No-Reflection Phenomena for Isotropic and Chiral Metamaterials

(等方性および旋光性メタマテリアルに対する無反射現象)

Yasuhiro Tamayama

January 2011

Abstract

We study Brewster's no-reflection phenomena for isotropic and chiral metamaterials. In naturally occurring media, the Brewster effect only exists for transverse-magnetic waves and not for transverse-electric waves. This asymmetry results from the assumption that the relative permeability is almost unity for higher frequencies, such as microwaves and light waves. The assumption is quite reasonable because for common materials, any kind of magnetic response is frozen in the high frequency regions. However, the assumption must be reconsidered for metamaterials, for which both the relative permittivity and permeability can be changed significantly from unity. In addition to permittivity and permeability, the chirality parameter and the non-reciprocity parameter can be controlled using metamaterials. Therefore, it is necessary to investigate the no-reflection conditions for generalized media. The objectives of our study are to experimentally observe Brewster's effect for transverse-electric waves in an isotropic metamaterial and to theoretically show the explicit relation among the medium parameters for achieving non-reflectivity in a chiral metamaterial.

First, we derive the wavenumber and the wave impedance in isotropic and chiral metamaterials. Properties of propagation, reflection, refraction, and transmission of electromagnetic waves are determined by these quantities that depend on medium parameters. Although the medium parameters in metamaterials can have arbitrary complex values, there are as yet no means by which to unambiguously calculate the wavenumber and wave impedance in such metamaterials. We show a few kinds of methods for determining the wavenumber and wave impedance in isotropic and chiral metamaterials with complex medium parameters.

Then, we experimentally demonstrate Brewster's effect for transverse-electric

waves with metamaterials. The Brewster effect can be observed for transverse-electric waves in media whose relative permeabilities do not equal unity. We design an array of split-ring resonators as a magnetic metamaterial using a finite-difference time-domain method. The reflection measurements are carried out in a 3-GHz region and the disappearance of reflected waves at a particular incident angle is confirmed.

Finally, we derive the explicit relation among permittivity, permeability, and chirality parameter of a chiral medium that satisfy the no-reflection condition for a planar interface between a vacuum and the chiral medium. We find that in general chiral media, the no-reflection condition is satisfied by elliptically polarized incident waves for at most one particular angle of incidence. When the wave impedance and the absolute value of the wavenumber in the chiral medium equal those in vacuum for one of the circularly polarized waves, the corresponding circularly polarized wave is transmitted to the medium without reflection for all angles of incidence. This is a qualitatively new mode of the no-reflection phenomenon. The no-reflection effect for chiral nihility media is found to be observed for linearly polarized waves at a particular incident angle, which resembles that for achiral media. We analyze the no-reflection effect for circularly polarized waves using a finite-difference time-domain method in detail. Also we propose a structure of an three-dimensional isotropic chiral metamaterial that is necessary to observe the no-reflection effect for circularly polarized waves.

Contents

1 Introduction **1**

1.1 Background 1

1.2 Progress in study of metamaterials 2

1.2.1 Negative refractive index media 2

1.2.2 Subwavelength imaging 5

1.2.3 Transformation optics 7

1.3 Objective and outline of this thesis 10

2 Fundamentals of propagation of electromagnetic waves **13**

2.1 Propagation in isotropic media 14

2.1.1 Conventional derivation 14

2.1.2 Choice of correct branch 16

2.1.3 Derivation from diagonalized Maxwell's equation 17

2.1.4 Formulae for calculating refractive index 19

2.1.5 Relation among permittivity, permeability, refractive index, and wave impedance on a complex plane 20

2.2 Propagation in chiral media 21

2.2.1 Wavenumber and wave impedance 21

2.2.2 Correspondence to wave propagation in isotropic media . . . 24

2.3 Summary 24

3 Observation of magnetic Brewster's effect in metamaterials **27**

3.1 Brewster's condition for isotropic media 28

3.1.1 Reflection and transmission for isotropic media 28

3.1.2 Derivation of Brewster's condition 30
3.1.3 Physical meaning of Brewster's condition 34
3.2 Magnetic metamaterials 37
3.2.1 Theoretical analysis of SRR 37
3.2.2 Numerical analysis of SRR 42
3.2.3 Measurement of admittance of single SRR 49
3.2.4 Measurement of electromagnetic properties of SRR array . . 56
3.3 Observation of magnetic Brewster's effect 65
3.3.1 Measurement system 66
3.3.2 Method 70
3.3.3 Results 71
3.3.4 Discussion 73
3.4 Summary 74

4 No-reflection conditions for chiral metamaterials 77
4.1 Reflection and transmission for chiral media 78
4.2 Derivation of no-reflection condition for chiral media 81
4.3 Analysis of no-reflection effect for chiral media 82
4.3.1 No-reflection effect for elliptically polarized waves 82
4.3.2 No-reflection effect for circularly polarized waves 85
4.3.3 No-reflection effect for linearly polarized waves 87
4.4 FDTD analysis of no-reflection effect for CP waves 90
4.5 Design of three-dimensional isotropic chiral metamaterial 93
4.6 Summary 94

5 Conclusion 97
5.1 Summary of this study 97
5.2 Future prospects 98

A Post and Tellegen representations 101

Acknowledgments 103

References 105

Chapter 1

Introduction

1.1 Background

Interest continues to grow in controlling the propagation of electromagnetic waves by utilizing periodically or randomly arranged artificial structures made of metal, dielectric, and other materials. When the size of the constituent structures and the separation between the neighboring structures are much smaller than the wavelength of the electromagnetic waves, the structure arrays behave as a continuous medium for the electromagnetic waves. That is, macroscopic medium parameters such as effective permittivity and permeability can be defined for the array. The artificial continuous medium is called a "metamaterial."

In the frequency region below the microwave frequency, the use of metallic structures as artificial media has been studied since the late 1940's [1]. At first, only control of the permittivity was studied and not that of the permeability. However, in 1999, Pendry *et al.* [2] proposed methods for fabricating artificial magnetic media, namely, magnetic metamaterials, which were built from nonmagnetic conductors. It was shown that not only can relative permeability be changed from unity but it also can have a negative value. Although the relative permeabilities of naturally occurring media are almost unity in such high frequency regions as microwave, terahertz, and optical regions, the restriction that the relative permeability is almost unity can be removed using the metamaterial. Moreover, the magnetic metamaterial enabled us to fabricate media with simultaneous negative permittivity and

permeability, or negative refractive index media that were predicted by Veselago [3] in 1967. In fact, Shelby *et al.* [4] made the first experimental verification of a negative refractive index metamaterial in the microwave region in 2001. This increased researcher interest in metamaterials.

It was not possible to independently control the wavenumber and the wave impedance in a medium until magnetic metamaterials were developed. The wavenumber is related to the propagation and refraction of electromagnetic waves, and the wave impedance is connected with the reflection. Phenomena about electromagnetic waves are described by these two quantities. In dielectric media, both of the wavenumber and wave impedance change with a change of the permittivity, and we cannot set these parameters independently. However, the wavenumber and wave impedance can be changed independently in metamaterials because we can control the permeability as well as the permittivity with metamaterials. By utilizing the flexibility of the wavenumber and wave impedance in metamaterials, such novel phenomena as a perfect lens (superlens) [5, 6], a hyperlens [7, 8], and an invisibility cloak [9–11] have been proposed and verified experimentally.

1.2 Progress in study of metamaterials

The studies of metamaterials are carried out in wide frequency range from the microwave region to the optical region because the idea of metamaterials is available irrespective of frequency.[1] Here, we describe some of the most famous studies of metamaterials.

1.2.1 Negative refractive index media

The refractive index n is given by $n = \sqrt{\varepsilon_{\mathrm{r}}\mu_{\mathrm{r}}}$, where ε_{r} is the relative permittivity and μ_{r} is the relative permeability. Veselago [3] suggested in 1967 that the refractive index becomes negative when both the relative permittivity and permeability are negative. However, there were no materials with simultaneous negative permittivity

[1] The idea of metamaterials is utilized not only for electromagnetic waves but also for acoustic waves [12].

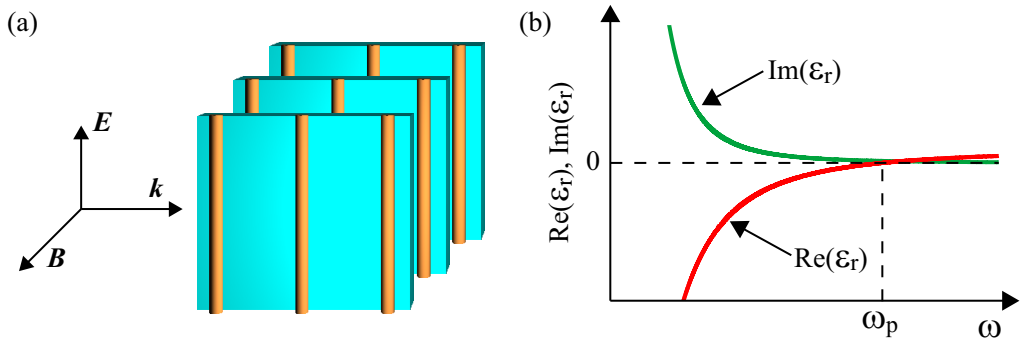

Figure 1.1: (a) Array of metallic wires and (b) its relative permittivity. Real part of the relative permittivity is negative below the effective plasma frequency ω_{p}.

and permeability, and experimental verifications of negative refractive index were not performed at that time.

Pendry *et al.* [13] proposed the method for fabricating artificial media with a desired negative permittivity in 1996. The artificial medium is composed of an array of metallic wires as shown in Fig. 1.1(a). It is well known that the relative permittivity of a metal is described by the Drude dispersion relation:

$$\varepsilon_{\mathrm{r}}(\omega) = 1 - \frac{\omega_{\mathrm{p}}^2}{\omega(\omega + \mathrm{i}\gamma)}, \tag{1.1}$$

where ω_{p} is a plasma frequency, γ ($\ll \omega_{\mathrm{p}}$) represents a damping, and the time-harmonic factor $\exp(-\mathrm{i}\omega t)$ is assumed.[2] A typical value of the plasma frequency in a metal is about the ultra-violet frequency. Equation (1.1) is plotted in Fig. 1.1(b). The real part of the relative permittivity is negative below the plasma frequency. The square of the plasma frequency is proportional to the density of free electrons in the metal and is inversely proportional to the effective mass of the electron. The density of the electrons in the array of metallic wires is less than that in the bulk metal. In addition, the effective mass of the electron in the array is larger than that in the bulk metal. Therefore, the effective plasma frequency in the array of metallic wires becomes smaller than the plasma frequency in the bulk metal. This implies that a desired negative permittivity can be obtained in the frequency region well

[2]We select $\exp(-\mathrm{i}\omega t)$ as the time-harmonic factor throughout this thesis.

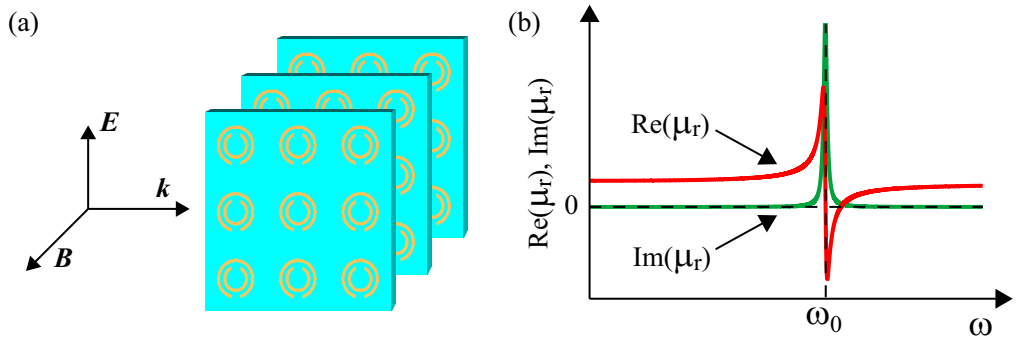

Figure 1.2: (a) Array of split-ring resonators and (b) its relative permeability. Real part of the relative permeability is negative in a narrow frequency range just above the resonance frequency ω_0.

below the plasma frequency in the bulk metal by controlling the effective plasma frequency and the effective mass of the electron, or the radius and density of the metallic wires.

Pendry *et al.* [2] also proposed the means by which to fabricate artificial magnetic media. The artificial structure is composed of an array of C-shaped double metallic ring structures as shown in Fig. 1.2(a). The structure is called a split-ring resonator (SRR). The SRR can be regarded as an inductor-capacitor (LC) series resonant circuit. When a time-varying magnetic field whose frequency is near the resonance frequency of the SRR goes through the ring, an electromotive force is induced and a large circular current flows in the SRR. This indicates that a large magnetic moment is induced. Therefore, the relative permeability is significantly changed from unity. Since the SRR behaves as an artificial resonant magnetic atom, the relative permeability of the SRR array is described by the Lorentz dispersion relation:

$$\mu_{\mathrm{r}}(\omega) = 1 - \frac{F\omega_0^2}{\omega^2 + \mathrm{i}\gamma\omega - \omega_0^2}, \tag{1.2}$$

where ω_0 is the resonance frequency, γ ($\ll \omega_0$) represents the damping, and F is a constant. Equation (1.2) is plotted in Fig. 1.2(b). One can see that the real part of the relative permeability is negative in the limited frequency range just above the resonance frequency.

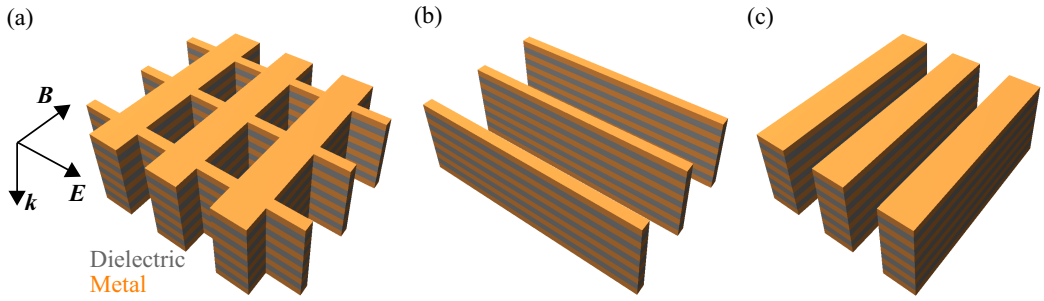

Figure 1.3: (a) Fishnet structure, which is a combination of structures (b) and (c). Structures (b) and (c) produce negative permittivity and permeability, respectively.

A negative refractive index metamaterial was first demonstrated by Shelby *et al.* [4] in the microwave region. The metamaterial consisted of an array of metallic wires and SRRs that was fabricated by printed circuit board technique. They measured the refraction angle when an electromagnetic wave was incident on the boundary between air and the metamaterial, and found that the refraction angle became negative, namely, the negative refractive index metamaterial was achieved.

The negative refraction phenomenon has already been observed even in the infrared region [14]. The metamaterial used in the experiment was made of cascaded fishnet structures as shown in Fig. 1.3(a). The structure was composed of alternating layers of metal (silver) and dielectric (magnesium fluoride) that were milled by focused ion beam. The fishnet structure is a combination of the structures shown in Fig. 1.3(b) and 1.3(c) [15]. The former structure produces a negative permittivity and the latter produces a negative permeability. The negative refractivity was confirmed through the measurement of the refraction angle.

1.2.2 Subwavelength imaging

It is commonly believed that the spot size of an electromagnetic wave focused by a lens does not become smaller than about the wavelength. This limitation is called the diffraction limit. The diffraction limit is explained simply as follows. We assume that electromagnetic fields are uniform in the y-direction and a line wave source exists at $(x, z) = (0, 0)$ as shown in Fig. 1.4(a). The electric field can be

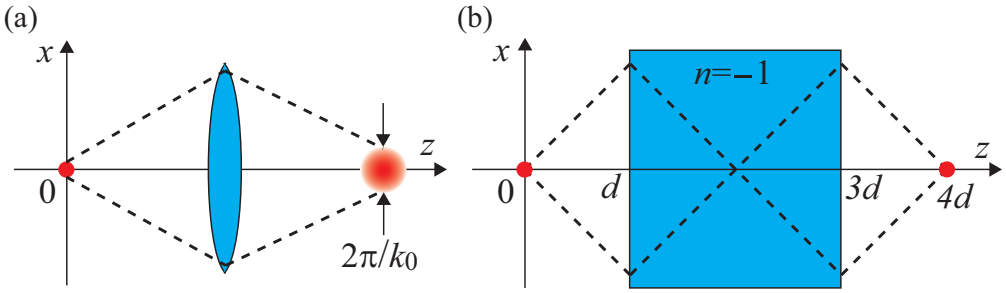

Figure 1.4: Focusings of electromagnetic waves by (a) a conventional lens and (b) a perfect lens. While the spot size is limited by the diffraction limit in the case of (a), the spot size can be infinitesimal in the case of (b).

expressed in the Fourier transformation form as

$$\boldsymbol{E}(x,z) = \int_{-\infty}^{\infty} \boldsymbol{E}(k_x)\mathrm{e}^{\mathrm{i}k_x x}\mathrm{e}^{\mathrm{i}k_z z}\,\mathrm{d}k_x, \tag{1.3}$$

where k_x and k_z are the wavenumbers in the x- and z-directions, respectively. Substituting $k_z = \sqrt{k_0^2 - k_x^2}$ (k_0: wavenumber in vacuum), we obtain

$$\begin{aligned}\boldsymbol{E}(x,z) = &\int_{-k_0}^{k_0} \boldsymbol{E}(k_x)\mathrm{e}^{\mathrm{i}k_x x}\mathrm{e}^{\mathrm{i}\sqrt{k_0^2-k_x^2}\,z}\,\mathrm{d}k_x \\ &+ \int_{-\infty}^{-k_0} \boldsymbol{E}(k_x)\mathrm{e}^{\mathrm{i}k_x x}\mathrm{e}^{-\sqrt{k_x^2-k_0^2}\,z}\,\mathrm{d}k_x + \int_{k_0}^{\infty} \boldsymbol{E}(k_x)\mathrm{e}^{\mathrm{i}k_x x}\mathrm{e}^{-\sqrt{k_x^2-k_0^2}\,z}\,\mathrm{d}k_x. \end{aligned} \tag{1.4}$$

The second and third terms exponentially decay with increasing z, namely, these terms represent evanescent wave components. Only the first term remains and the electromagnetic field components having $|k_x| > k_0$ vanish in the far field region. Therefore, the spot size cannot be smaller than about $2\pi/k_0 = \lambda$ even if the electromagnetic wave is focused by an infinitely large lens.

We consider the case where the lens is replaced with an infinite slab of a negative refractive index medium with $\varepsilon_\mathrm{r} = -1$, $\mu_\mathrm{r} = -1$, and thickness $2d$ as shown in Fig. 1.4(b). From the point of view of ray optics, an electromagnetic wave radiated from $(x,z) = (0,0)$ is found to converge to $(x,z) = (0,4d)$ as shown in Fig. 1.4(b). This indicates that the slab of the negative refractive index medium acts as a converging lens. From the viewpoint of wave optics, it follows that the electric field

at $z = 4d$ is given by

$$\begin{aligned}\boldsymbol{E}(x,4d) = &\int_{-k_0}^{k_0} \boldsymbol{E}(k_x)\mathrm{e}^{\mathrm{i}k_x x}\,\mathrm{e}^{\mathrm{i}\sqrt{k_0^2-k_x^2}\,d}\,\mathrm{e}^{-\mathrm{i}\sqrt{k_0^2-k_x^2}\,2d}\,\mathrm{e}^{\mathrm{i}\sqrt{k_0^2-k_x^2}\,d}\,\mathrm{d}k_x \\ &+ \int_{-\infty}^{-k_0} \boldsymbol{E}(k_x)\mathrm{e}^{\mathrm{i}k_x x}\,\mathrm{e}^{-\sqrt{k_x^2-k_0^2}\,d}\,\mathrm{e}^{+\sqrt{k_x^2-k_0^2}\,2d}\,\mathrm{e}^{-\sqrt{k_x^2-k_0^2}\,d}\,\mathrm{d}k_x \\ &+ \int_{k_0}^{\infty} \boldsymbol{E}(k_x)\mathrm{e}^{\mathrm{i}k_x x}\,\mathrm{e}^{-\sqrt{k_x^2-k_0^2}\,d}\,\mathrm{e}^{+\sqrt{k_x^2-k_0^2}\,2d}\,\mathrm{e}^{-\sqrt{k_x^2-k_0^2}\,d}\,\mathrm{d}k_x, \qquad (1.5)\\ = &\int_{-\infty}^{\infty} \boldsymbol{E}(k_x)\mathrm{e}^{\mathrm{i}k_x x}\,\mathrm{d}k_x = \boldsymbol{E}(x,0). \qquad (1.6)\end{aligned}$$

The electric field distribution at $z = 0$ is the same as that at $z = 4d$. That is, the electromagnetic wave can be focused to an infinitesimal point with the slab of the medium having $\varepsilon_\mathrm{r} = -1$ and $\mu_\mathrm{r} = -1$. The slab is called a "perfect lens [5]." The evanescent waves are enhanced in the perfect lens and contribute to the resolution of the image. Therefore, the spot size can be smaller than the diffraction limit. Note that the evanescent waves transport no energy, namely, amplifications of the electromagnetic wave do not occur in the perfect lens.

Subwavelength imaging by a negative refractive index metamaterial is carried out by Lagarkov *et al.* [6]. They observed superresolution of two wave sources separated by the distance of $\lambda/6$.

There exist reflection and transmission losses in an actual negative refractive index metamaterial, and therefore, subwavelength imaging by a perfect lens can be achieved only in the near field region. On the other hand, it is proposed [7] and experimentally verified [8] that subwavelength imaging can be achieved in the far field region by using a highly anisotropic medium, which is called a "hyperlens." Liu *et al.* [8] fabricated a hyperlens in the ultra-violet region ($\lambda = 365\,\mathrm{nm}$) and achieved a resolution of 130 nm.

1.2.3 Transformation optics

Transformation optics [9,16] is a technique for controlling propagation of electromagnetic waves using the form invariance of Maxwell's equations under coordinate transformations. One can control electromagnetic waves without unnecessary reflection by the technique.

Maxwell's equations for a monochromatic electromagnetic wave are given by

$$\boldsymbol{\nabla} \times \boldsymbol{E} = \mathrm{i}\omega[\mu]\boldsymbol{H}, \quad \boldsymbol{\nabla} \times \boldsymbol{H} = -\mathrm{i}\omega[\varepsilon]\boldsymbol{E}, \tag{1.7}$$

where ω is an angular frequency of the electromagnetic wave, $[\mu]$ is a permeability tensor, and $[\varepsilon]$ is a permittivity tensor. We consider the transformation described as

$$\boldsymbol{x}' = \boldsymbol{x}'(\boldsymbol{x}), \quad \boldsymbol{E}'(\boldsymbol{x}') = (A^T)^{-1}\boldsymbol{E}(\boldsymbol{x}), \quad \boldsymbol{H}'(\boldsymbol{x}') = (A^T)^{-1}\boldsymbol{H}(\boldsymbol{x}), \tag{1.8}$$

where A is the Jacobi matrix with elements

$$A_{ij} = \frac{\partial x_i'}{\partial x_j}, \tag{1.9}$$

and T stands for transposition. For the transformed fields, the following equations are satisfied [16]:

$$\boldsymbol{\nabla}' \times \boldsymbol{E}' = \mathrm{i}\omega[\mu']\boldsymbol{H}', \quad \boldsymbol{\nabla}' \times \boldsymbol{H}' = -\mathrm{i}\omega[\varepsilon']\boldsymbol{E}', \tag{1.10}$$

where

$$[\mu'(\boldsymbol{x}')] = \frac{A[\mu(\boldsymbol{x})]A^T}{\det A}, \quad [\varepsilon'(\boldsymbol{x}')] = \frac{A[\varepsilon(\boldsymbol{x})]A^T}{\det A}. \tag{1.11}$$

By comparing Eqs. (1.7) and (1.10), it is found that the influence of the transformation appears in the permittivity tensor and permeability tensor. This indicates that the electromagnetic wave is bent in the manner represented by the Jacobi matrix A without unnecessary reflection by setting the permittivity and permeability tensors as described in Eq. (1.11).

A great deal of attention has been focused on an invisibility cloak [9] as an application of transformation optics. Let us suppose that a plane electromagnetic wave propagates in vacuum from left to right as shown in Fig. 1.5(a). We consider the coordinate transformation that compresses space from the cylindrical region $0 < r < b$ into the annular region $a < r' < b$ as shown in Fig. 1.5(b), where r and r' are the radial coordinates in the original and transformed systems, respectively. This transformation is given by[3]

$$r' = \frac{b-a}{b}r + a, \quad \theta' = \theta, \quad z' = z, \quad (0 < r < b), \tag{1.12}$$

[3]The coordinate transformation $r' = [(b-a)/b^n]r^n + a$ $(n > 0)$ is also possible in this case [17].

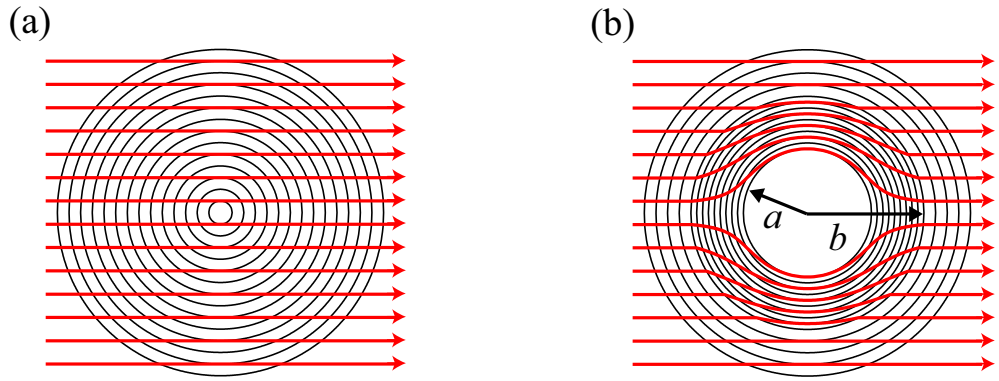

Figure 1.5: Propagations of electromagnetic waves in (a) vacuum and (b) transformed system. In the transformed system, an arbitrary object contained in the region $r' < a$ is invisible from external observers.

where θ and z (θ' and z') are the angular and vertical coordinates in the original (transformed) system, respectively. Equation (1.12) leads to the permittivity and permeability tensor components in the transformed system as follows:

$$\begin{aligned} &\frac{\varepsilon_{r'}}{\varepsilon_0} = \frac{\mu_{r'}}{\mu_0} = \frac{r'-a}{r'}, \quad \frac{\varepsilon_{\theta'}}{\varepsilon_0} = \frac{\mu_{\theta'}}{\mu_0} = \frac{r'}{r'-a}, \\ &\frac{\varepsilon_{z'}}{\varepsilon_0} = \frac{\mu_{z'}}{\mu_0} = \left(\frac{b}{b-a}\right)^2 \frac{r'-a}{r'}, \quad (a < r' < b), \end{aligned} \tag{1.13}$$

where ε_0 and μ_0 are the permittivity and permeability in vacuum, respectively. The electromagnetic wave does not penetrate into the cylindrical region $r' < a$ and the transmitted wave propagates as if it had passed through vacuum as shown in Fig. 1.5(b) when the medium parameters are set as described in Eq. (1.13). That is, an arbitrary object contained in the region $r' < a$ is concealed from external observers. The annular region $a < r' < b$ is called a "invisibility cloak." The invisibility cloak have been demonstrated experimentally in the microwave region [11].

As another cloaking device, a carpet cloak is studied [18]. The carpet cloak hides a bump in a metallic mirror. Experimental verifications of the carpet cloak are performed in the microwave [19] and infrared [20, 21] regions. It is theoretically shown that transformation optics can also be applied to a beam divider [22] and subwavelength imaging [23].

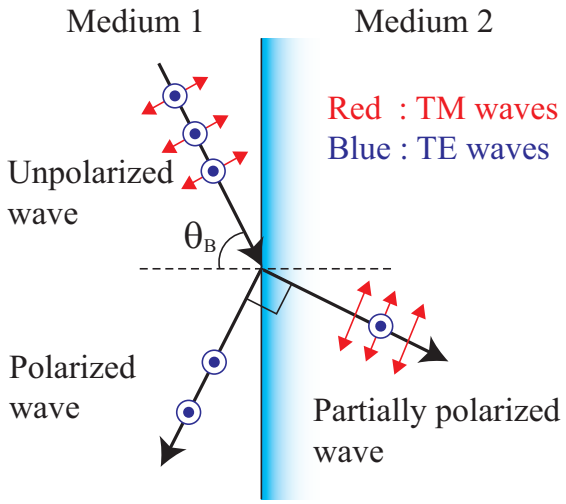

Figure 1.6: Brewster's effect. The reflectance for TM waves vanishes when the incident angle is equal to Brewster's angle θ_{B}.

1.3 Objective and outline of this thesis

Although most research of metamaterials has concentrated on negative refractivity, subwavelength imaging, and transformation optics (especially invisibility cloak), these phenomena are not all things that can be achieved using metamaterials. It is possible to find out new applications by exploring other phenomena in metamaterials. In this study, we focus on Brewster's no-reflection effect in metamaterials. Brewster's condition is one of the main features of the laws of reflection and refraction of electromagnetic waves at a boundary between two distinct media [24]. A schematic illustration of the Brewster effect is shown in Fig. 1.6. For a specific incident angle, known as the Brewster angle, the reflection wave vanishes. In naturally occurring media, this phenomenon only exists for transverse-magnetic (TM) waves (p waves) and not for transverse-electric (TE) waves (s waves). It is conveniently applied in optical instruments. One can generate completely polarized light from an unpolarized light source only with a glass plate. It can also be used to avoid the reflection losses at the surfaces of optical components. The Brewster window of the discharge tube in gaseous lasers is a typical example.

As we described above, the Brewster effect in naturally occurring media only

exists for TM waves and not for TE waves. This asymmetry results from the assumption that the relative permeability μ_r is almost unity for higher frequencies, such as microwaves and light waves. Each medium is characterized only by its relative permittivity ε_r. The assumption is quite reasonable because for common materials, any kind of magnetic response is frozen in high frequency regions. However, the assumption must be reconsidered for metamaterials, for which both ε_r and μ_r can be changed significantly from unity. It is not difficult to find that Brewster's effect arises for TE waves in a medium with $\varepsilon_r = 1$ and $\mu_r \neq 1$, which is a dual of normal dielectric materials, $\varepsilon_r \neq 1$ and $\mu_r = 1$. Actually, Brewster's effect for TE waves has been predicted [25–28]. Nevertheless, an experimental verification of the TE Brewster effect has not been carried out due to the absence of appropriate media.

In addition to permittivity and permeability, the chirality parameter and the non-reciprocity parameter can be controlled using metamaterials. It is also possible to control the anisotropy in electromagnetic responses. Therefore, the no-reflection condition for generalized media should be explored in order to develop novel devices for reflection control of electromagnetic waves. Brewster's condition has been theoretically studied for anisotropic media [29–32], chiral media (bi-isotropic media) [33, 34], and bi-anisotropic media [35]. However, thus far, the explicit relation among the medium parameters for achieving non-reflectivity in chiral and bi-anisotropic media have not been determined.

The objectives of our study are to experimentally observe Brewster's effect for TE waves in a magnetic metamaterial and to theoretically show the explicit relation among the medium parameters for achieving non-reflectivity in a chiral metamaterial.

An outline of this thesis is as follows. In Chap. 2, we derive the wavenumber and the wave impedance in isotropic and chiral metamaterials. The wavenumber and wave impedance, which are related to propagation, reflection, refraction, and transmission of electromagnetic waves, depend on the medium parameters. Although the medium parameters in metamaterials can have arbitrary complex values, the method currently used for calculating the wavenumber and wave impedance can be applied only when the medium is passive, or the imaginary parts of the medium

parameters are not negative. We show that the wavenumber and wave impedance in both passive and active metamaterials can be calculated by considering the direction of the energy flow of an electromagnetic wave. In Chap. 3, we describe an experimental demonstration of Brewster's effect for TE waves in a magnetic metamaterial. It is shown that Brewster's condition is satisfied for TE waves and not for TM waves in magnetic media. An array of SRRs is used for the experiment of the TE Brewster effect as a magnetic metamaterial. We analyze the permittivity and permeability of the SRR array by theoretical, numerical, and experimental methods and then make an experiment of observing Brewster's effect for TE waves in the SRR array. In Chap. 4, we analyze the no-reflection effect for chiral media. The no-reflection condition is derived from the vanishing eigenvalue condition of the reflection Jones matrix. We show that the analysis can be largely simplified by decomposing the reflection matrix into the unit and Pauli matrices. The no-reflection effect is found to be observed for elliptically polarized incident waves at a particular angle of incidence for general chiral media. This is merely a natural extension of the conventional Brewster's effect. When the wave impedance and the absolute value of the wavenumber for one of the circularly polarized waves in the chiral medium equal those in vacuum, the no-reflection effect arises for the corresponding circularly polarized wave irrespective of the incident angle. This phenomenon is a qualitatively new mode of the no-reflection effect. We find that the no-reflection effect for chiral nihility media is observed for linearly polarized waves at a particular incident angle, which resembles that for achiral media. We focus on the no-reflection effect for circularly polarized waves and analyze it by a finite-difference time-domain (FDTD) method [36] in detail. Besides, we propose a structure of an isotropic chiral metamaterial that could be used to achieve the no-reflection effects for elliptically and circularly polarized waves. In Chap. 5, summary of this study and future prospects are described.

Chapter 2

Fundamentals of propagation of electromagnetic waves

Properties of propagation, reflection, refraction, and transmission of electromagnetic waves are determined by the wavenumber and the wave impedance that depend on medium parameters. In the conventional optics, it is usually assumed that only the permittivity can be changed from the vacuum value. Based on this assumption, the wavenumber and wave impedance are calculated and analyses of various kinds of wave propagation are performed. However, the other medium parameters, also, can be changed from their vacuum values using metamaterials [37]. In addition, it is possible to control losses and gains of electromagnetic responses in metamaterials [38–41]. That is, one could control all of the medium parameters as complex values. When the medium parameters become complex values, there are some cases where the conventional method for calculating the wavenumber and wave impedance cannot be used. Thus, it is necessary to develop a derivation of the wavenumber and wave impedance that is able to be applied to such metamaterials.

We derive the wavenumber and wave impedance in isotropic media with complex values of the permittivity and permeability. A few kinds of methods are shown for calculating the wavenumber and wave impedance. These parameters are determined also for chiral media that have complex values of the permittivity, permeability, and chirality parameter. In the calculations, we do not take the causality into account. That is, we assume that the locations of the poles of the electromagnetic

susceptibilities may be anywhere on a complex frequency plane.

2.1 Propagation in isotropic media

We analyze the wavenumber and wave impedance in isotropic media. First, the wavenumber and wave impedance are derived by the conventional method and a problem of the method is described. Then, a few methods are presented for calculating the wavenumber and wave impedance in isotropic metamaterials having complex medium parameters without any trouble.

2.1.1 Conventional derivation

In order to derive the wavenumber k and wave impedance Z in isotropic media, we start from Maxwell's equations:

$$\mathrm{rot}\,\boldsymbol{E} = -\frac{\partial \boldsymbol{B}}{\partial t}, \tag{2.1}$$

$$\mathrm{rot}\,\boldsymbol{H} = \frac{\partial \boldsymbol{D}}{\partial t}. \tag{2.2}$$

For a monochromatic plane electromagnetic wave with time (t) and space ($\boldsymbol{r}$) dependence $\exp\left[-\mathrm{i}(\omega t - \boldsymbol{k}\cdot\boldsymbol{r})\right]$, Eqs. (2.1) and (2.2) are reduced to

$$\boldsymbol{k}\times\boldsymbol{E} = \omega\boldsymbol{B}, \tag{2.3}$$

$$\boldsymbol{k}\times\boldsymbol{H} = -\omega\boldsymbol{D}, \tag{2.4}$$

respectively. Substituting constitutive equations:

$$\boldsymbol{D} = \varepsilon\boldsymbol{E}, \tag{2.5}$$

$$\boldsymbol{H} = \mu^{-1}\boldsymbol{B}, \tag{2.6}$$

into Eqs. (2.3) and (2.4) and assuming that the prorogation direction of the electromagnetic wave is the z-direction, namely $\boldsymbol{k} = k\boldsymbol{e}_z$ ($\boldsymbol{e}_z$ is the unit vector in the z-direction), we obtain

$$k\begin{bmatrix} 1 & & & O \\ & 1 & & \\ & & 1 & \\ O & & & 1 \end{bmatrix}\begin{bmatrix} E_x \\ E_y \\ H_x \\ H_y \end{bmatrix} = \omega\begin{bmatrix} O & & & \mu \\ & & -\mu & \\ & -\varepsilon & & \\ \varepsilon & & & O \end{bmatrix}\begin{bmatrix} E_x \\ E_y \\ H_x \\ H_y \end{bmatrix}. \tag{2.7}$$

This indicates that the electromagnetic fields can be decomposed into two polarization components, which are (E_x, H_y) and (E_y, H_x) polarization components. From Eq. (2.7), we have

$$k^2 = \omega^2 \varepsilon \mu, \tag{2.8}$$

$$Z^2 = \left(\frac{E_x}{H_y}\right)^2 = \left(-\frac{E_y}{H_x}\right)^2 = \frac{\mu}{\varepsilon}. \tag{2.9}$$

These equations yield the refractive index n and the normalized wave impedance Z_r as follows:

$$n = \frac{k}{k_0} = \sqrt{\varepsilon_\mathrm{r}\mu_\mathrm{r}}, \tag{2.10}$$

$$Z_\mathrm{r} = \frac{Z}{Z_0} = \sqrt{\frac{\mu_\mathrm{r}}{\varepsilon_\mathrm{r}}}, \tag{2.11}$$

where k_0 and Z_0 are the wavenumber and the wave impedance in a vacuum, respectively. The square root function is a double-valued function. Thus, it is necessary to choose the appropriate branches in order to calculate n and Z_r. When both ε_r and μ_r are real values, the following procedure is used to select the correct branches.

The branch of $\sqrt{\mu_\mathrm{r}/\varepsilon_\mathrm{r}}$ should be selected so that $Z_\mathrm{r} > 0$ is satisfied. If $Z_\mathrm{r} < 0$, the absolute value of the reflectivity at the boundary between a vacuum and the medium becomes larger than unity [see Eqs. (3.11) and (3.13)]. This phenomenon cannot occur in passive media.

The correct branch of $\sqrt{\varepsilon_\mathrm{r}\mu_\mathrm{r}}$ can be determined by considering the relation among $\boldsymbol{E}$, $\boldsymbol{H}$, $\boldsymbol{k}$, and the Poynting vector: $\boldsymbol{S} = \boldsymbol{E} \times \boldsymbol{H}$. In the case of $\varepsilon_\mathrm{r}\mu_\mathrm{r} < 0$, n becomes a purely imaginary number and electromagnetic waves do not propagate in the medium. Thus, we have only to consider the two cases: both of the relative permittivity and permeability are positive and negative. When $\varepsilon_\mathrm{r} > 0$ and $\mu_\mathrm{r} > 0$, one can find from Eqs. (2.3)-(2.6) that the vectors $\boldsymbol{E}$, $\boldsymbol{H}$, and $\boldsymbol{k}$ are right-handed set and $\boldsymbol{k}$ is parallel to $\boldsymbol{S}$ as shown in Fig. 2.1(a). Therefore, the branch of $\sqrt{\varepsilon_\mathrm{r}\mu_\mathrm{r}}$ should be chosen so that $n > 0$. When $\varepsilon_\mathrm{r} < 0$ and $\mu_\mathrm{r} < 0$, the vectors $\boldsymbol{E}$, $\boldsymbol{H}$, and $\boldsymbol{k}$ are left-handed set and $\boldsymbol{k}$ is anti-parallel to $\boldsymbol{S}$ as shown in Fig. 2.1(b). Hence, the branch of $\sqrt{\varepsilon_\mathrm{r}\mu_\mathrm{r}}$ should be determined so that $n < 0$. From the relation among $\boldsymbol{E}$, $\boldsymbol{H}$, and $\boldsymbol{k}$, a medium with positive (negative) refractive index is often called a right-handed (left-handed) medium [3].

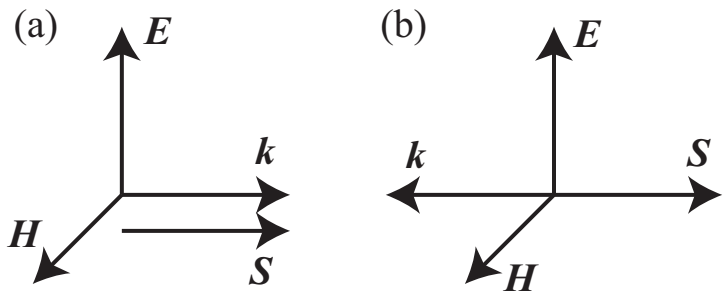

Figure 2.1: Relations among $\boldsymbol{E}$, $\boldsymbol{H}$, $\boldsymbol{k}$, and $\boldsymbol{S}$ for isotropic media having (a) $n > 0$ and (b) $n < 0$.

When the medium does not have gain, or $\mathrm{Im}\,(\varepsilon_\mathrm{r}) \geq 0$ and $\mathrm{Im}\,(\mu_\mathrm{r}) \geq 0$ are satisfied, we can also determine the correct branch. The branch of $\sqrt{\mu_\mathrm{r}/\varepsilon_\mathrm{r}}$ and $\sqrt{\varepsilon_\mathrm{r}\mu_\mathrm{r}}$ should be selected so that $\mathrm{Re}\,(Z_\mathrm{r}) > 0$ and $\mathrm{Im}\,(n) \geq 0$ are satisfied. The reasons are as follows. If $\mathrm{Re}\,(Z_\mathrm{r}) < 0$, the absolute value of the reflectivity at the boundary between a vacuum and the medium becomes larger than unity [see Eqs. (3.11) and (3.13)]. If $\mathrm{Im}\,(n) < 0$, the amplitude of the electromagnetic wave is amplified as the electromagnetic wave propagates in the medium. These phenomena cannot occur in passive media.

When either or both of $\mathrm{Im}\,(\varepsilon_\mathrm{r})$ and $\mathrm{Im}\,(\mu_\mathrm{r})$ are negative, there is as yet no means by which to determine the correct branch. Thus, the wavenumber and wave impedance cannot be calculated unambiguously.

2.1.2 Choice of correct branch

The correct branch can be chosen from the facts that the wave impedance is related to the direction of the energy flow and that the refractive index is connected with the relation between the directions of the energy flow and the wavenumber.

We derive the relation between the wave impedance and the energy flow. The time-averaged Poynting vector, which governs the energy flow of electromagnetic

waves, is written as

$$\langle \boldsymbol{S} \rangle = \frac{1}{2} \mathrm{Re}\,(EH^*)\boldsymbol{e}_z \tag{2.12}$$

$$= \frac{|E|^2}{2} \mathrm{Re}\left(\frac{1}{Z}\right)\boldsymbol{e}_z = \frac{|H|^2}{2} \mathrm{Re}\,(Z)\boldsymbol{e}_z, \tag{2.13}$$

where E and H are, respectively, the complex amplitudes of the vectors $\boldsymbol{E}$ and $\boldsymbol{H}$, and the asterisk represents complex conjugation. Equation (2.13) shows that the direction of the energy flow is related to the real part of the wave impedance.

From Eq. (2.7), we obtain the following equations:

$$k = \omega\varepsilon Z = \frac{\omega\mu}{Z}, \tag{2.14}$$

which represent the relation between the wavenumber and the energy flow. In order to calculate the wavenumber corresponding to the positive (negative) energy flow, we should choose the branch of Z so that $\mathrm{Re}\,(Z) > 0$ [$\mathrm{Re}\,(Z) < 0$] is satisfied and substitute Z into Eq. (2.14). When the wave impedance is purely imaginary value, the energy flow vanishes in the medium, namely, electromagnetic waves cannot penetrate the medium. Thus, it is nonsense to determine the wavenumber in the case of $\mathrm{Re}\,(Z) = 0$.

The refractive index is the ratio of the wavenumber of the electromagnetic wave propagating in the medium to that in a vacuum in the case where the directions of their energy flows are the same as each other:

$$n = \frac{\omega\varepsilon Z}{\omega\varepsilon_0 Z_0} = \varepsilon_\mathrm{r} Z_\mathrm{r}, \tag{2.15}$$

$$= \frac{\omega\mu Z^{-1}}{\omega\mu_0 Z_0^{-1}} = \frac{\mu_\mathrm{r}}{Z_\mathrm{r}}. \tag{2.16}$$

Here the condition $\mathrm{Re}\,(Z_\mathrm{r}) > 0$ is satisfied because Z_0 is a real value and the directions of the energy flows of these two waves are the same, or $\mathrm{Re}\,(Z)\,\mathrm{Re}\,(Z_0) > 0$. This indicates that the refractive index can be calculated from Eqs. (2.15) and (2.16) without ambiguity.

2.1.3 Derivation from diagonalized Maxwell's equation

The wavenumber and wave impedance can be derived also from diagonalized Maxwell's equation. One can understand the relation among the electromagnetic

fields, wavenumber, and wave impedance for each eigenmode more clearly by diagonalizing Maxwell's equation.

In order to diagonalize Eq. (2.7), we use the following transformation matrix:

$$U = \frac{1}{\sqrt{2}} \begin{bmatrix} 1 & 1 & 0 & 0 \\ 0 & 0 & 1 & 1 \\ 0 & 0 & -Z^{-1} & Z^{-1} \\ Z^{-1} & -Z^{-1} & 0 & 0 \end{bmatrix}, \quad U^{-1} = \frac{1}{\sqrt{2}} \begin{bmatrix} 1 & 0 & 0 & Z \\ 1 & 0 & 0 & -Z \\ 0 & 1 & -Z & 0 \\ 0 & 1 & Z & 0 \end{bmatrix}. \tag{2.17}$$

The coefficient matrix M at the right-hand side of Eq. (2.7) is transformed into

$$U^{-1}MU = \frac{\omega}{2} \begin{bmatrix} \varepsilon Z + \mu Z^{-1} & \varepsilon Z - \mu Z^{-1} & 0 & 0 \\ -\varepsilon Z + \mu Z^{-1} & -\varepsilon Z - \mu Z^{-1} & 0 & 0 \\ 0 & 0 & \varepsilon Z + \mu Z^{-1} & \varepsilon Z - \mu Z^{-1} \\ 0 & 0 & -\varepsilon Z + \mu Z^{-1} & -\varepsilon Z - \mu Z^{-1} \end{bmatrix}, \tag{2.18}$$

$$= \omega\varepsilon Z \begin{bmatrix} 1 & 0 & 0 & 0 \\ 0 & -1 & 0 & 0 \\ 0 & 0 & 1 & 0 \\ 0 & 0 & 0 & -1 \end{bmatrix} = \omega\mu Z^{-1} \begin{bmatrix} 1 & 0 & 0 & 0 \\ 0 & -1 & 0 & 0 \\ 0 & 0 & 1 & 0 \\ 0 & 0 & 0 & -1 \end{bmatrix}, \tag{2.19}$$

where the relation $\varepsilon Z = \mu Z^{-1}$ ($Z^2 = \mu/\varepsilon$) is used. From the above equations and Eq. (2.7), we obtain the diagonalized Maxwell equation:

$$k \begin{bmatrix} E_x + ZH_y \\ E_x - ZH_y \\ E_y - ZH_x \\ E_y + ZH_x \end{bmatrix} = \omega\varepsilon Z \begin{bmatrix} 1 & 0 & 0 & 0 \\ 0 & -1 & 0 & 0 \\ 0 & 0 & 1 & 0 \\ 0 & 0 & 0 & -1 \end{bmatrix} \begin{bmatrix} E_x + ZH_y \\ E_x - ZH_y \\ E_y - ZH_x \\ E_y + ZH_x \end{bmatrix}, \tag{2.20}$$

$$= \omega\mu Z^{-1} \begin{bmatrix} 1 & 0 & 0 & 0 \\ 0 & -1 & 0 & 0 \\ 0 & 0 & 1 & 0 \\ 0 & 0 & 0 & -1 \end{bmatrix} \begin{bmatrix} E_x + ZH_y \\ E_x - ZH_y \\ E_y - ZH_x \\ E_y + ZH_x \end{bmatrix}. \tag{2.21}$$

The first and second (third and fourth) rows of Eqs. (2.20) and (2.21) correspond to the x-polarized (y-polarized) electromagnetic waves. Assuming that the real

part of the wave impedance is positive, the directions of the energy flows of the electromagnetic waves represented by the first and third (second and fourth) rows are the positive (negative) z-direction. The wavenumbers for the eigenmodes whose energy flows are directed to the positive (negative) z-direction are given by $k = \omega\varepsilon Z = \omega\mu Z^{-1}$ ($k = -\omega\varepsilon Z = -\omega\mu Z^{-1}$). This result is consistent with Sec. 2.1.2. Even if we assume $\mathrm{Re}\,(Z) < 0$, we can obtain the same result by regarding $-Z$ as the wave impedance.

The above discussion demonstrates that there is no loss of generality in supposing $\mathrm{Re}\,(Z) > 0$. Therefore, we choose the branch of Z so that $\mathrm{Re}\,(Z) > 0$ is satisfied from now on.

2.1.4 Formulae for calculating refractive index

The refractive index can be calculated from Eqs. (2.15) and (2.16), while these equations seem to be different from the familiar expression, Eq. (2.10). That is, the normalized wave impedance appears in Eqs. (2.15) and (2.16); however, it does not appear in Eq. (2.10). We consider the formulae for calculating the correct refractive index from Eq. (2.10) by setting calculation rules.

The calculation rules are as follows:

1. The absolute value and argument of square root of a complex number $\alpha = |\alpha| \exp(\mathrm{i}\theta_\alpha)$ are $\sqrt{|\alpha|}$ (> 0) and $\theta_\alpha/2$, respectively.

2. The arguments θ_ε and θ_μ of the relative permittivity and permeability are set so that $|\theta_\mu - \theta_\varepsilon| < \pi$ is satisfied.

Rule 1 is introduced for making a square root function a single-valued function. Rule 2 corresponds to $\mathrm{Re}\,(Z_\mathrm{r}) > 0$.

We show that the correct refractive index can be calculated by using these rules. The normalized wave impedance is written as

$$Z_\mathrm{r} = \sqrt{\frac{\mu_\mathrm{r}}{\varepsilon_\mathrm{r}}}, \tag{2.22}$$

$$= \sqrt{\frac{|\mu_\mathrm{r}|}{|\varepsilon_\mathrm{r}|}} \exp\left(\mathrm{i}\frac{\theta_\mu - \theta_\varepsilon}{2}\right), \tag{2.23}$$

which naturally satisfies $\mathrm{Re}\,(Z_\mathrm{r}) > 0$. Substituting Eq. (2.23) into Eqs. (2.15) and (2.16), we obtain

$$n = \varepsilon_\mathrm{r} Z_\mathrm{r} = \frac{\mu_\mathrm{r}}{Z_\mathrm{r}}, \tag{2.24}$$

$$= \sqrt{|\varepsilon_\mathrm{r}||\mu_\mathrm{r}|}\exp\left(\mathrm{i}\frac{\theta_\mu + \theta_\varepsilon}{2}\right). \tag{2.25}$$

On the other hand, Eq. (2.10) yields

$$n = \sqrt{\varepsilon_\mathrm{r}\mu_\mathrm{r}}, \tag{2.26}$$

$$= \sqrt{|\varepsilon_\mathrm{r}||\mu_\mathrm{r}|}\exp\left(\mathrm{i}\frac{\theta_\mu + \theta_\varepsilon}{2}\right). \tag{2.27}$$

Equation (2.27) agrees with Eq. (2.25). This implies that we can obtain the correct refractive index from $n = \sqrt{\varepsilon_\mathrm{r}\mu_\mathrm{r}}$ by setting the above calculation rules.

2.1.5 Relation among permittivity, permeability, refractive index, and wave impedance on a complex plane

We consider the relation among the permittivity, permeability, refractive index, and wave impedance on a complex plane and describe how to determine the correct branch of the refractive index from the relation.

From Eqs. (2.23) and (2.27), the arguments θ_n and θ_Z of the refractive index and normalized wave impedance are, respectively, found to be

$$\theta_n = \frac{\theta_\mu + \theta_\varepsilon}{2}, \tag{2.28}$$

$$\theta_Z = \frac{\theta_\mu - \theta_\varepsilon}{2}, \tag{2.29}$$

which are reduced to

$$\theta_\mu - \theta_n = \theta_n - \theta_\varepsilon = \theta_Z. \tag{2.30}$$

The absolute values of $\theta_\mu - \theta_n$ and $\theta_n - \theta_\varepsilon$ are acute angles because the absolute value of θ_Z is acute angle. Based on this fact, the argument of the refractive index can be determined. Figure 2.2 shows the relation among ε_r, μ_r, n, and Z_r on a complex plane.

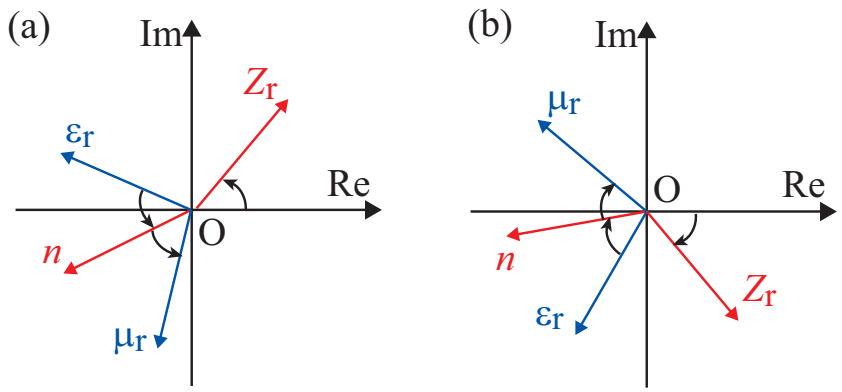

Figure 2.2: Relations among relative permittivity ε_r, relative permeability μ_r, refractive index n, and normalized wave impedance Z_r on a complex plane when the imaginary part of normalized wave impedance is (a) positive ($\theta_Z > 0$) and (b) negative ($\theta_Z < 0$). The angles represented by the three arrows in each figure are equal to each other.

2.2 Propagation in chiral media

We derive the wavenumber and wave impedance in chiral media having complex medium parameters. By using a similar procedure to Sec. 2.1.3, we show the relation among the electromagnetic fields, wavenumber, and wave impedance for each eigenmode without ambiguity. We consider the correspondence of the wave propagation in chiral media to that in isotropic media.

2.2.1 Wavenumber and wave impedance

The constitutive equations for chiral media have several types of expressions. The Post and Tellegen representations are mainly used as the constitutive equations. The Post representation is written as

$$\boldsymbol{D} = \varepsilon_{\mathrm{P}}\boldsymbol{E} - \mathrm{i}\xi_{\mathrm{P}}\boldsymbol{B}, \tag{2.31}$$

$$\boldsymbol{H} = \mu_{\mathrm{P}}^{-1}\boldsymbol{B} - \mathrm{i}\xi_{\mathrm{P}}\boldsymbol{E}, \tag{2.32}$$

and the Tellegen representation is written as

$$\boldsymbol{D} = \varepsilon_{\mathrm{T}}\boldsymbol{E} - \mathrm{i}\kappa_{\mathrm{T}}\boldsymbol{H}, \tag{2.33}$$

$$\boldsymbol{B} = \mu_{\mathrm{T}}\boldsymbol{H} + \mathrm{i}\kappa_{\mathrm{T}}\boldsymbol{E}, \tag{2.34}$$

where $\varepsilon_{\mathrm{P,T}}$ is the permittivity, $\mu_{\mathrm{P,T}}$ is the permeability, and ξ_{p} and κ_{T} are the chirality parameters. The subscript P (T) stands for the Post (Tellegen) representation. These representations are equivalent and interchangeable with the following transformation (see Appendix A):

$$\varepsilon_{\mathrm{T}} = \varepsilon_{\mathrm{P}} + \mu_{\mathrm{P}}\xi_{\mathrm{P}}^2, \quad \mu_{\mathrm{T}} = \mu_{\mathrm{P}}, \quad \kappa_{\mathrm{T}} = \mu_{\mathrm{P}}\xi_{\mathrm{P}}. \tag{2.35}$$

In this thesis, we consistently use the Post representation and omit the subscript P for simplicity.

Substituting Eqs. (2.31) and (2.32) into Eqs. (2.3) and (2.4) and assuming $\boldsymbol{k} = k\boldsymbol{e}_z$, we obtain

$$k\begin{bmatrix} 1 & & & O \\ & 1 & & \\ & & 1 & \\ O & & & 1 \end{bmatrix}\begin{bmatrix} E_x \\ E_y \\ H_x \\ H_y \end{bmatrix} = \omega\begin{bmatrix} 0 & \mathrm{i}\mu\xi & 0 & \mu \\ -\mathrm{i}\mu\xi & 0 & -\mu & 0 \\ 0 & -(\varepsilon+\mu\xi^2) & 0 & \mathrm{i}\mu\xi \\ \varepsilon+\mu\xi^2 & 0 & -\mathrm{i}\mu\xi & 0 \end{bmatrix}\begin{bmatrix} E_x \\ E_y \\ H_x \\ H_y \end{bmatrix}. \tag{2.36}$$

This equation has a nontrivial solution when the following condition is satisfied:

$$\begin{vmatrix} k & -\mathrm{i}\omega\mu\xi & 0 & \omega\mu \\ \mathrm{i}\omega\mu\xi & k & \omega\mu & 0 \\ 0 & \omega(\varepsilon+\mu\xi^2) & k & -\mathrm{i}\omega\mu\xi \\ -\omega(\varepsilon+\mu\xi^2) & 0 & \mathrm{i}\omega\mu\xi & k \end{vmatrix} = 0. \tag{2.37}$$

From this equation, we have the wavenumber:

$$k = \pm\omega(\sqrt{\varepsilon\mu+\mu^2\xi^2}+\mu\xi), \quad \pm\omega(\sqrt{\varepsilon\mu+\mu^2\xi^2}-\mu\xi). \tag{2.38}$$

After substitution of the derived wavenumber into Eq. (2.36), the relation among the wavenumber and the electromagnetic fields is obtained and summarized in Tab. 2.1. Here we define the wave impedance Z_{c} of the chiral medium as

$$Z_{\mathrm{c}} = \sqrt{\frac{\mu}{\varepsilon+\mu\xi^2}}. \tag{2.39}$$

Table 2.1: Relation among wavenumber and electromagnetic fields in chiral media. Ratio of each electromagnetic field component to E_x is written for each eigenmode. Here $k_\pm = \omega(\sqrt{\varepsilon\mu + \mu^2\xi^2} \pm \mu\xi) = \omega[(\varepsilon + \mu\xi^2)Z_\mathrm{c} \pm \mu\xi]$ and $Z_\mathrm{c} = \sqrt{\mu/(\varepsilon + \mu\xi^2)}$ $[\mathrm{Re}\,(Z_\mathrm{c}) > 0]$.

k	k_+	$-k_+$	k_-	$-k_-$
E_x	1	1	1	1
E_y	$-\mathrm{i}$	i	i	$-\mathrm{i}$
H_x	$\mathrm{i}Z_\mathrm{c}^{-1}$	$\mathrm{i}Z_\mathrm{c}^{-1}$	$-\mathrm{i}Z_\mathrm{c}^{-1}$	$-\mathrm{i}Z_\mathrm{c}^{-1}$
H_y	Z_c^{-1}	$-Z_\mathrm{c}^{-1}$	Z_c^{-1}	$-Z_\mathrm{c}^{-1}$

The eigenpolarizations in chiral media are found to be circularly polarized (CP) waves because $E_y/E_x = \pm\mathrm{i}$ is satisfied.

Equations (2.38) and (2.39) contain double-valued square root functions. In order to choose a correct branch, we diagonalize Eq. (2.36). By using the transformation matrix:

$$U = \frac{1}{2}\begin{bmatrix} 1 & 1 & 1 & 1 \\ -\mathrm{i} & \mathrm{i} & \mathrm{i} & -\mathrm{i} \\ \mathrm{i}Z_\mathrm{c}^{-1} & \mathrm{i}Z_\mathrm{c}^{-1} & -\mathrm{i}Z_\mathrm{c}^{-1} & -\mathrm{i}Z_\mathrm{c}^{-1} \\ Z_\mathrm{c}^{-1} & -Z_\mathrm{c}^{-1} & Z_\mathrm{c}^{-1} & -Z_\mathrm{c}^{-1} \end{bmatrix}, \quad U^{-1} = \frac{1}{2}\begin{bmatrix} 1 & \mathrm{i} & -\mathrm{i}Z_\mathrm{c} & Z_\mathrm{c} \\ 1 & -\mathrm{i} & -\mathrm{i}Z_\mathrm{c} & -Z_\mathrm{c} \\ 1 & -\mathrm{i} & \mathrm{i}Z_\mathrm{c} & Z_\mathrm{c} \\ 1 & \mathrm{i} & \mathrm{i}Z_\mathrm{c} & -Z_\mathrm{c} \end{bmatrix}, \tag{2.40}$$

Eq. (2.36) is diagonalized as follows:

$$\begin{aligned} k\begin{bmatrix} E_x + \mathrm{i}E_y - \mathrm{i}Z_\mathrm{c}H_x + Z_\mathrm{c}H_y \\ E_x - \mathrm{i}E_y - \mathrm{i}Z_\mathrm{c}H_x - Z_\mathrm{c}H_y \\ E_x - \mathrm{i}E_y + \mathrm{i}Z_\mathrm{c}H_x + Z_\mathrm{c}H_y \\ E_x + \mathrm{i}E_y + \mathrm{i}Z_\mathrm{c}H_x - Z_\mathrm{c}H_y \end{bmatrix} \\ = \begin{bmatrix} k_+ & & & O \\ & -k_+ & & \\ & & k_- & \\ O & & & -k_- \end{bmatrix}\begin{bmatrix} E_x + \mathrm{i}E_y - \mathrm{i}Z_\mathrm{c}H_x + Z_\mathrm{c}H_y \\ E_x - \mathrm{i}E_y - \mathrm{i}Z_\mathrm{c}H_x - Z_\mathrm{c}H_y \\ E_x - \mathrm{i}E_y + \mathrm{i}Z_\mathrm{c}H_x + Z_\mathrm{c}H_y \\ E_x + \mathrm{i}E_y + \mathrm{i}Z_\mathrm{c}H_x - Z_\mathrm{c}H_y \end{bmatrix}, \end{aligned} \tag{2.41}$$

where we use the relation $(\varepsilon + \mu\xi^2)Z_\mathrm{c} = \mu Z_\mathrm{c}^{-1}$ $[Z_\mathrm{c}^2 = \mu/(\varepsilon + \mu\xi^2)]$ and set

$$k_\pm = \omega[(\varepsilon + \mu\xi^2)Z_\mathrm{c} \pm \mu\xi]. \tag{2.42}$$

As we described in Sec. 2.1, there is no loss of generality in supposing that the real part of Z_c is positive. The directions of the energy flows of the eigenmodes represented by the first and third (second and fourth) rows of Eq. (2.41) are found to be the positive (negative) z-direction. Thus, k_+ and k_- ($-k_+$ and $-k_-$) are the wavenumbers for the eigenmodes whose energy flows are directed to the positive (negative) z-direction. The wavenumbers k_+ and k_- can be calculated from Eq. (2.42) without ambiguity. We define the eigenmodes represented by the first and second (third and fourth) rows as left circularly polarized (LCP) [right circularly polarized (RCP)] waves.

2.2.2 Correspondence to wave propagation in isotropic media

We rewrite Eq. (2.36), which is Maxwell's equation for chiral media represented by linear polarization bases, in circular polarization bases.

We set $E_\pm = E_x \pm \mathrm{i}E_y$ and $H_\pm = H_y \mp \mathrm{i}H_x$. Here $Z_\mathrm{c} = E_\pm/H_\pm$ is satisfied and upper and lower signs respectively correspond to LCP and RCP waves. By using $E_\pm$ and $H_\pm$ instead of E_x, E_y, H_x, and H_y, Eq. (2.36) is reduced to

$$\left.\begin{aligned} kE_\pm &= \omega(\mu \pm \mu\xi Z_\mathrm{c})H_\pm, \\ kH_\pm &= \omega(\varepsilon + \mu\xi^2 \pm \mu\xi Z_\mathrm{c}^{-1})E_\pm. \end{aligned}\right\} \tag{2.43}$$

Comparing Eq. (2.43) with Eq. (2.7), the wavenumber and wave impedance for LCP and RCP waves are found to be equal to those in an isotropic medium having a permittivity $\varepsilon_\pm = \varepsilon + \mu\xi^2 \pm \mu\xi Z_\mathrm{c}^{-1}$ and a permeability $\mu_\pm = \mu \pm \mu\xi Z_\mathrm{c}$.

2.3 Summary

We analyzed the propagation of electromagnetic waves in isotropic and chiral media. A few kinds of methods were shown for calculating the wavenumber

and wave impedance in metamaterials with complex medium parameters. The wavenumber and wave impedance were determined unambiguously by considering the relations between the direction of the energy flow and the real part of the wave impedance and between the wavenumber and the wave impedance. We clarified the relation among the electromagnetic fields, wavenumber, and wave impedance for each eigenmode from the diagonalized Maxwell equation.

The results can be utilized for controlling the propagation of electromagnetic waves in isotropic and chiral metamaterials having losses and gains. The calculation methods can be expanded into generalized media having anisotropy and nonreciprocity, namely, bi-anisotropic media.

Chapter 3

Observation of magnetic Brewster's effect in metamaterials

It is generally believed that Brewster's condition exists only for TM waves and not for TE waves. This asymmetry results from the assumption that $\varepsilon_{\mathrm{r}} \neq 1$ and $\mu_{\mathrm{r}} = 1$ are satisfied for high-frequency electromagnetic fields in naturally occurring media. By considering the dual to Brewster's effect in naturally occurring media, it is found that Brewster's condition is satisfied for TE waves and not for TM waves in media with $\varepsilon_{\mathrm{r}} = 1$ and $\mu_{\mathrm{r}} \neq 1$. Actually, Brewster's condition in isotropic media with both electric and magnetic responses has been studied in the past literature [25–28]. Although Brewster's effect for TE waves has been predicted theoretically in these studies, the experimental verification has not been performed due to the absence of appropriate media. In this study, we demonstrate Brewster's effect for TE waves in magnetic metamaterials [42].

First, we derive Brewster's condition for a boundary between a vacuum and an isotropic medium. We show whether Brewster's condition exists for TM waves or TE waves for given medium parameters, ε_{r} and μ_{r}. Then, we analyze a magnetic metamaterial, namely, an array of SRRs. Theoretical, numerical, and experimental analyses of the metamaterial are carried out in order to examine whether the medium parameters of the metamaterial satisfy Brewster's condition for TE waves. Finally, we demonstrate the TE Brewster effect in the SRR array metamaterial.

3.1 Brewster's condition for isotropic media

We calculate a reflectivity of electromagnetic waves at a plane boundary between a vacuum and an isotropic medium and derive Brewster's no-reflection condition. We show the relation between the medium parameters and the incident polarization for which the Brewster condition is satisfied. The physical meaning of the Brewster condition is clarified by calculating radiations from an electric dipole moment and a magnetic moment in the medium.

3.1.1 Reflection and transmission for isotropic media

First, we derive the reflection and transmission coefficients at a boundary between a vacuum and an isotropic medium for TE waves. Let us assume that a monochromatic plane electromagnetic wave is incident from the vacuum on the isotropic medium as shown in Fig. 3.1(a). The electromagnetic fields of the incident (i), reflected (r), and transmitted (t) waves are written as

$$\boldsymbol{E}_{\mathrm{i}} = E_{\mathrm{i}}\boldsymbol{e}_z \exp\left[\mathrm{i}k_0(x\cos\theta_{\mathrm{i}} - y\sin\theta_{\mathrm{i}})\right], \tag{3.1}$$

$$\boldsymbol{H}_{\mathrm{i}} = H_{\mathrm{i}}(-\cos\theta_{\mathrm{i}}\boldsymbol{e}_y - \sin\theta_{\mathrm{i}}\boldsymbol{e}_x) \exp\left[\mathrm{i}k_0(x\cos\theta_{\mathrm{i}} - y\sin\theta_{\mathrm{i}})\right], \tag{3.2}$$

$$\boldsymbol{E}_{\mathrm{r}} = E_{\mathrm{r}}\boldsymbol{e}_z \exp\left[\mathrm{i}k_0(-x\cos\theta_{\mathrm{r}} - y\sin\theta_{\mathrm{r}})\right], \tag{3.3}$$

$$\boldsymbol{H}_{\mathrm{r}} = H_{\mathrm{r}}(\cos\theta_{\mathrm{r}}\boldsymbol{e}_y - \sin\theta_{\mathrm{r}}\boldsymbol{e}_x) \exp\left[\mathrm{i}k_0(-x\cos\theta_{\mathrm{r}} - y\sin\theta_{\mathrm{r}})\right], \tag{3.4}$$

$$\boldsymbol{E}_{\mathrm{t}} = E_{\mathrm{t}}\boldsymbol{e}_z \exp\left[\mathrm{i}k(x\cos\theta_{\mathrm{t}} - y\sin\theta_{\mathrm{t}})\right], \tag{3.5}$$

$$\boldsymbol{H}_{\mathrm{t}} = H_{\mathrm{t}}(-\cos\theta_{\mathrm{t}}\boldsymbol{e}_y - \sin\theta_{\mathrm{t}}\boldsymbol{e}_x) \exp\left[\mathrm{i}k(x\cos\theta_{\mathrm{t}} - y\sin\theta_{\mathrm{t}})\right], \tag{3.6}$$

where $\boldsymbol{e}_x$, $\boldsymbol{e}_y$, and $\boldsymbol{e}_z$ are the unit vectors in the directions of the positive x-, y-, and z-axes, respectively. The common time-harmonic factor $\exp(-\mathrm{i}\omega t)$ is omitted for simplicity. The continuity of the tangential components of the electromagnetic fields across the boundary is reduced to

$$E_{\mathrm{i}}\exp(-\mathrm{i}k_0 y\sin\theta_{\mathrm{i}}) + E_{\mathrm{r}}\exp(-\mathrm{i}k_0 y\sin\theta_{\mathrm{r}}) = E_{\mathrm{t}}\exp(-\mathrm{i}ky\sin\theta_{\mathrm{t}}), \tag{3.7}$$

$$-H_{\mathrm{i}}\cos\theta_{\mathrm{i}}\exp(-\mathrm{i}k_0 y\sin\theta_{\mathrm{i}}) + H_{\mathrm{r}}\cos\theta_{\mathrm{r}}\exp(-\mathrm{i}k_0 y\sin\theta_{\mathrm{r}}) = -H_{\mathrm{t}}\cos\theta_{\mathrm{t}}\exp(-\mathrm{i}ky\sin\theta_{\mathrm{t}}). \tag{3.8}$$

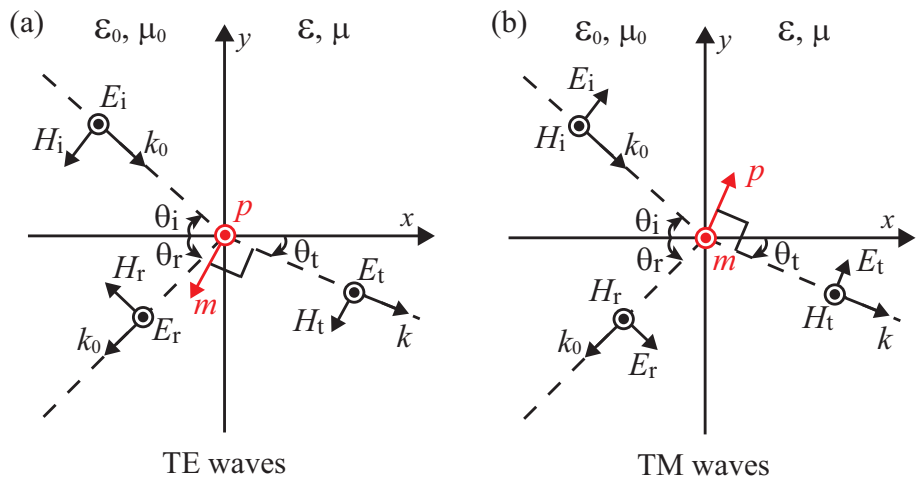

Figure 3.1: Relations among electric field, magnetic field, and wavenumber for (a) TE waves and (b) TM waves.

In order to satisfy Eqs. (3.7) and (3.8) for arbitrary y, the conditions

$$k_0 \sin\theta_\mathrm{i} = k_0 \sin\theta_\mathrm{r}, \tag{3.9}$$

$$k_0 \sin\theta_\mathrm{i} = k \sin\theta_\mathrm{t}, \tag{3.10}$$

must be satisfied. Equations (3.9) and (3.10) are known as the law of reflection ($\theta_\mathrm{i} = \theta_\mathrm{r}$) and Snell's law ($\sin\theta_\mathrm{i} = n\sin\theta_\mathrm{t}$), respectively. Substituting Eqs. (3.9) and (3.10) into Eqs. (3.7) and (3.8), we obtain the reflection coefficient r_TE and the transmission coefficient t_TE:

$$r_\mathrm{TE} = \frac{E_\mathrm{r}}{E_\mathrm{i}} = \frac{Z_\mathrm{r}\cos\theta_\mathrm{i} - \cos\theta_\mathrm{t}}{Z_\mathrm{r}\cos\theta_\mathrm{i} + \cos\theta_\mathrm{t}}, \tag{3.11}$$

$$t_\mathrm{TE} = \frac{E_\mathrm{t}}{E_\mathrm{i}} = \frac{2Z_\mathrm{r}\cos\theta_\mathrm{i}}{Z_\mathrm{r}\cos\theta_\mathrm{i} + \cos\theta_\mathrm{t}}, \tag{3.12}$$

where we use $Z_0 = E_\mathrm{i}/H_\mathrm{i} = E_\mathrm{r}/H_\mathrm{r}$, and $Z_\mathrm{r}Z_0 = E_\mathrm{t}/H_\mathrm{t}$.

Next, we show the reflection coefficient r_TM and the transmission coefficient t_TM for TM waves [see Fig. 3.1(b)]. With a similar procedure to the above discussion,

we have

$$r_{\mathrm{TM}} = \frac{H_{\mathrm{r}}}{H_{\mathrm{i}}} = \frac{Z_{\mathrm{r}}^{-1}\cos\theta_{\mathrm{i}} - \cos\theta_{\mathrm{t}}}{Z_{\mathrm{r}}^{-1}\cos\theta_{\mathrm{i}} + \cos\theta_{\mathrm{t}}}, \tag{3.13}$$

$$t_{\mathrm{TM}} = \frac{H_{\mathrm{t}}}{H_{\mathrm{i}}} = \frac{2Z_{\mathrm{r}}^{-1}\cos\theta_{\mathrm{i}}}{Z_{\mathrm{r}}^{-1}\cos\theta_{\mathrm{i}} + \cos\theta_{\mathrm{t}}}. \tag{3.14}$$

3.1.2 Derivation of Brewster's condition

Brewster's condition can be derived from the zero reflection condition. We consider whether Brewster's condition is satisfied for TE waves or TM waves and calculate Brewster's angle θ_{B} for purely dielectric, purely magnetic, and general isotropic media.

In case of purely dielectric media

To begin with, we derive Brewster's condition for purely dielectric media whose relative permeability is unity. All of naturally occurring media in high frequency region fall into this case.

After substitution of $\mu_{\mathrm{r}} = 1$ into Eqs. (3.11) and (3.13), we obtain

$$r_{\mathrm{TE}} = -\frac{\sin(\theta_{\mathrm{i}} - \theta_{\mathrm{t}})}{\sin(\theta_{\mathrm{i}} + \theta_{\mathrm{t}})}, \tag{3.15}$$

$$r_{\mathrm{TM}} = \frac{\tan(\theta_{\mathrm{i}} - \theta_{\mathrm{t}})}{\tan(\theta_{\mathrm{i}} + \theta_{\mathrm{t}})}, \tag{3.16}$$

which are known as (a part of) the Fresnel equations. Brewster's condition for TE and TM waves are derived from $r_{\mathrm{TE}} = 0$ and $r_{\mathrm{TM}} = 0$, respectively. Since θ_{i} does not equal θ_{t} for oblique incidence, the numerators in Eqs. (3.15) and (3.16) cannot vanish. However, r_{TM} vanishes when $\tan(\theta_{\mathrm{i}} + \theta_{\mathrm{t}})$ diverges to infinity, or $\theta_{\mathrm{i}} + \theta_{\mathrm{t}}$ equals $\pi/2$. Thus, Brewster's condition exists only for TM waves and not for TE waves in purely dielectric media. From the condition $\theta_{\mathrm{i}} + \theta_{\mathrm{r}} = \pi/2$, one can find that Brewster's angle satisfies $\tan\theta_{\mathrm{B}} = \sqrt{\varepsilon_{\mathrm{r}}}$.

In case of purely magnetic media

Magnetic media can be fabricated in high frequency region with metamaterials; therefore, it is necessary to eliminate the restriction of $\mu_{\mathrm{r}} = 1$. We derive Brewster's

condition for purely magnetic media.

By substituting $\varepsilon_{\rm r} = 1$ into Eqs. (3.11) and (3.13), we have

$$r_{\rm TE} = \frac{\tan(\theta_{\rm i} - \theta_{\rm t})}{\tan(\theta_{\rm i} + \theta_{\rm t})}, \tag{3.17}$$

$$r_{\rm TM} = -\frac{\sin(\theta_{\rm i} - \theta_{\rm t})}{\sin(\theta_{\rm i} + \theta_{\rm t})}. \tag{3.18}$$

From these equations, one sees that Brewster's condition exists only for TE waves and not for TM waves. Brewster's angle is given by $\tan\theta_{\rm B} = \sqrt{\mu_{\rm r}}$. The result is natural because purely magnetic media are dual to purely dielectric media and TE waves are dual to TM waves.

In case of general isotropic media

We now derive Brewster's condition for general isotropic media that respond to both the electric and magnetic fields of electromagnetic waves. We describe the relation among the relative permittivity, relative permeability, and incident polarization that satisfies Brewster's condition and calculate Brewster's angle for the given medium parameters.

Brewster's condition is derived from Eqs. (3.11) and (3.13). Using Snell's law, Eqs. (3.11) and (3.13) are reduced to

$$r_{\rm TE} = \frac{Z_{\rm r}\cos\theta_{\rm i} - \sqrt{1 - n^{-2}\sin^2\theta_{\rm i}}}{Z_{\rm r}\cos\theta_{\rm i} + \sqrt{1 - n^{-2}\sin^2\theta_{\rm i}}}, \tag{3.19}$$

$$r_{\rm TM} = \frac{Z_{\rm r}^{-1}\cos\theta_{\rm i} - \sqrt{1 - n^{-2}\sin^2\theta_{\rm i}}}{Z_{\rm r}^{-1}\cos\theta_{\rm i} + \sqrt{1 - n^{-2}\sin^2\theta_{\rm i}}}. \tag{3.20}$$

If either $\varepsilon_{\rm r}$ or $\mu_{\rm r}$ is negative, both $Z_{\rm r}$ and n become purely imaginary numbers. From Eqs. (3.19) and (3.20), $|r_{\rm TE}|$ and $|r_{\rm TM}|$ are found to equal unity independent of the incident angle. Thus, total reflection occurs for any incident angle and there is no Brewster condition. This indicates that we have only to treat the cases that both $\varepsilon_{\rm r}$ and $\mu_{\rm r}$ are positive and negative. When $1 - n^{-2}\sin^2\theta_{\rm i}$ is negative, $|r_{\rm TE}|$ and $|r_{\rm TM}|$ become unity, namely, the incident wave is totally reflected. It is not necessary to take the case of $1 - n^{-2}\sin^2\theta_{\rm i} < 0$ into account in the analysis of the no-reflection condition.

We examine whether r_{TE} or r_{TM} can vanish based on the reflectivities at normal incidence and the differentiations of the reflectivities with respect to the incident angle. From Eqs. (3.19) and (3.20), it follows that the reflectivities at normal incidence satisfy

$$r_{\mathrm{TE}}(\theta_{\mathrm{i}}=0)>0, \quad r_{\mathrm{TM}}(\theta_{\mathrm{i}}=0)<0 \qquad \text{when} \quad Z_{\mathrm{r}}>1, \tag{3.21}$$

$$r_{\mathrm{TE}}(\theta_{\mathrm{i}}=0)<0, \quad r_{\mathrm{TM}}(\theta_{\mathrm{i}}=0)>0 \qquad \text{when} \quad Z_{\mathrm{r}}<1. \tag{3.22}$$

Differentiating both sides of Eqs. (3.19) and (3.20) with respect to θ_{i}, we obtain

$$\frac{\mathrm{d}r_{\mathrm{TE}}}{\mathrm{d}\theta_{\mathrm{i}}}=\frac{2Z_{\mathrm{r}}(n^{-2}-1)\sin\theta_{\mathrm{i}}}{\left(Z_{\mathrm{r}}\cos\theta_{\mathrm{i}}+\sqrt{1-n^{-2}\sin^2\theta_{\mathrm{i}}}\right)^2\sqrt{1-n^{-2}\sin^2\theta_{\mathrm{i}}}}, \tag{3.23}$$

$$\frac{\mathrm{d}r_{\mathrm{TM}}}{\mathrm{d}\theta_{\mathrm{i}}}=\frac{2Z_{\mathrm{r}}^{-1}(n^{-2}-1)\sin\theta_{\mathrm{i}}}{\left(Z_{\mathrm{r}}^{-1}\cos\theta_{\mathrm{i}}+\sqrt{1-n^{-2}\sin^2\theta_{\mathrm{i}}}\right)^2\sqrt{1-n^{-2}\sin^2\theta_{\mathrm{i}}}}. \tag{3.24}$$

The functions $\sin\theta_{\mathrm{i}}$, $\cos\theta_{\mathrm{i}}$, and $\sqrt{1-n^{-2}\sin^2\theta_{\mathrm{i}}}$ give positive values for any incident angle, and therefore, one sees that

$$\frac{\mathrm{d}r_{\mathrm{TE}}}{\mathrm{d}\theta_{\mathrm{i}}}<0, \quad \frac{\mathrm{d}r_{\mathrm{TM}}}{\mathrm{d}\theta_{\mathrm{i}}}<0 \qquad \text{when} \quad |n|>1, \tag{3.25}$$

$$\frac{\mathrm{d}r_{\mathrm{TE}}}{\mathrm{d}\theta_{\mathrm{i}}}>0, \quad \frac{\mathrm{d}r_{\mathrm{TM}}}{\mathrm{d}\theta_{\mathrm{i}}}>0 \qquad \text{when} \quad |n|<1. \tag{3.26}$$

This implies that the amplitude reflectivities r_{TE} and r_{TM} are monotonically increasing or decreasing functions with respect to θ_{i}. From Eqs. (3.21), (3.22), (3.25), and (3.26), we can understand that Brewster's effect arises for TE waves when $|n|>1$ and $Z_{\mathrm{r}}>1$ and when $|n|<1$ and $Z_{\mathrm{r}}<1$. On the other hand, it occurs for TM waves in the case of $|n|>1$ and $Z_{\mathrm{r}}<1$ and in the case of $|n|<1$ and $Z_{\mathrm{r}}>1$. Converting the parameters (n, Z_{r}) into the medium parameters $(\varepsilon_{\mathrm{r}}, \mu_{\mathrm{r}})$, Brewster's condition is found to be satisfied for TE waves (TM waves) in the shaded (unshaded) region of the $(\varepsilon_{\mathrm{r}}, \mu_{\mathrm{r}})$-plane in Fig. 3.2.

When $Z_{\mathrm{r}}=1$ and $|n|\neq 1$, both r_{TE} and r_{TM} vanish only for normal incidence. That is, arbitrary polarized waves are not reflected only for normal incidence in the case of $\varepsilon_{\mathrm{r}}=\mu_{\mathrm{r}}\neq 1$. If $Z_{\mathrm{r}}\neq 1$ and $|n|=1$, conditions $r_{\mathrm{TE}}(\theta_{\mathrm{i}}=0)\neq 0$, $\mathrm{d}r_{\mathrm{TE}}/\mathrm{d}\theta_{\mathrm{i}}=0$, $r_{\mathrm{TM}}(\theta_{\mathrm{i}}=0)\neq 0$, and $\mathrm{d}r_{\mathrm{TM}}/\mathrm{d}\theta_{\mathrm{i}}=0$ are satisfied, namely, the reflectivities never

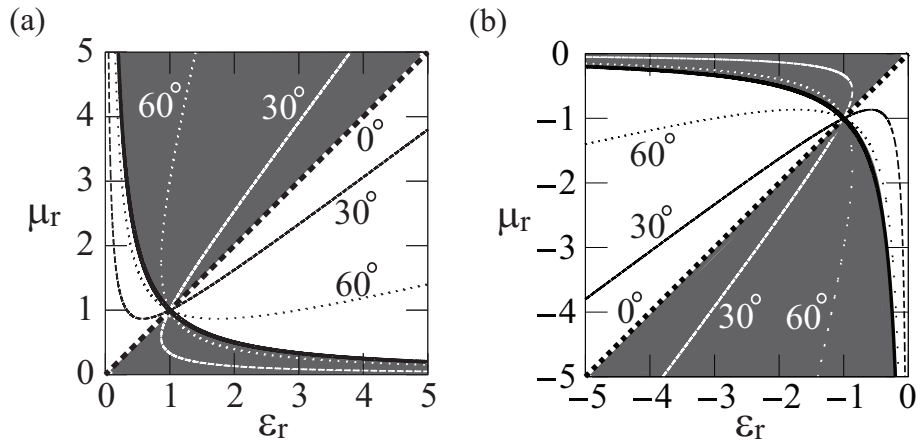

Figure 3.2: Brewster's condition for media with relative permittivity ε_r and relative permeability μ_r. Brewster's condition exists in the (a) first and (b) third quadrants of the $(\varepsilon_\mathrm{r}, \mu_\mathrm{r})$-plane. Brewster's conditions for TE and TM waves exist in the shaded and unshaded areas, respectively. All the lines except the bold solid line represent the contour lines of the Brewster angles. The bold solid line and the bold dashed line correspond to $\varepsilon_\mathrm{r}\mu_\mathrm{r} = \pm 1$ and $\varepsilon_\mathrm{r} = \mu_\mathrm{r}$, namely, $n = \pm 1$ and $Z_\mathrm{r} = 1$, respectively.

vanish. Therefore, Brewster's condition does not exist for media with $\varepsilon_\mathrm{r} = \mu_\mathrm{r}^{-1} \neq 1$. When $Z_\mathrm{r} = 1$ and $|n| = 1$, the reflectivities for TE and TM waves vanish for all angles of incidence. Thus, arbitrary polarized waves are not reflected for any incident angle in the cases of $(\varepsilon_\mathrm{r}, \mu_\mathrm{r}) = (1, 1)$ and $(\varepsilon_\mathrm{r}, \mu_\mathrm{r}) = (-1, -1)$.

Brewster's angle is derived from Eqs. (3.19) and (3.20). By solving the no-reflection conditions, $r_\mathrm{TE} = 0$ and $r_\mathrm{TM} = 0$, we obtain the following equation:

$$0 \leq \sin^2\theta_\mathrm{B} = \frac{\alpha^2 - n^2}{\alpha^2 - 1} \leq 1, \tag{3.27}$$

where $\alpha = \mu_\mathrm{r}$ for TE waves and $\alpha = \varepsilon_\mathrm{r}$ for TM waves. With this equation, the Brewster angle can be determined for a given pair, $(\varepsilon_\mathrm{r}, \mu_\mathrm{r})$. In Fig. 3.2, the Brewster angles are plotted parametrically on the $(\varepsilon_\mathrm{r}, \mu_\mathrm{r})$-plane.

It is apparent that Brewster's effect arises only for TM waves in normal media ($\mu_\mathrm{r} = 1$). However, for a medium with $\mu_\mathrm{r} \neq \pm 1$, the Brewster condition for TE waves can be observed. For a given $|\mu_\mathrm{r}| \gtrless 1$, when $1/|\mu_\mathrm{r}| \lesseqgtr |\varepsilon_\mathrm{r}| \lesseqgtr |\mu_\mathrm{r}|$ is satisfied, there exists a Brewster angle for TE waves. In other words, the medium must

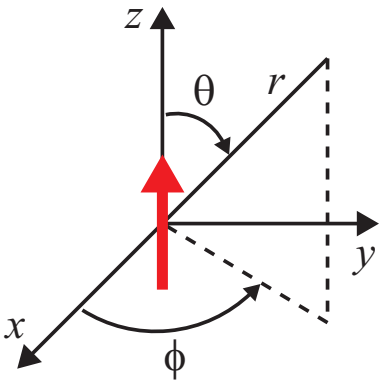

Figure 3.3: Geometry of coordinate system for an electric dipole moment (magnetic moment). Red arrow represents the electric dipole moment (magnetic moment).

be more magnetic, rather than electric, in order to realize the Brewster condition for TE waves. From this fact, Brewster's effect for TE waves is called "magnetic Brewster's effect [27]."

3.1.3 Physical meaning of Brewster's condition

We discuss the physical meaning of Brewster's condition by analyzing the electromagnetic fields radiated by the induced electric dipole moment and magnetic moment in the medium.

In case of purely dielectric or purely magnetic media

First, we consider the physical meaning of Brewster's condition for purely dielectric media. Let us define a spherical coordinate system (r, θ, ϕ) and assume that an electric dipole moment p is located at the origin of the coordinate system as shown in Fig. 3.3. In the far field region, the electric field $\boldsymbol{E}_p = (E_{pr}, E_{p\theta}, E_{p\phi})$ of the electromagnetic wave produced by the electric dipole moment is given by $E_{pr} = 0$, $E_{p\phi} = 0$, and

$$E_{p\theta} = -\frac{\pi c_0 Z_0 p \mathrm{e}^{\mathrm{i}k_0 r}}{\lambda^2 r} \sin\theta, \tag{3.28}$$

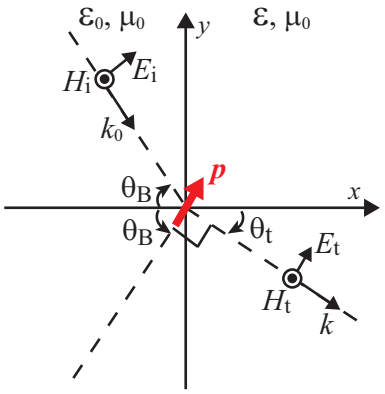

Figure 3.4: Physical meaning of Brewster's condition in purely dielectric media for TM waves.

where the electromagnetic field is assumed to be radiated to a vacuum [43]. From Eq. (3.28), one sees that the electric dipole moment cannot emit radiation in the direction of the vibration, $\theta = 0, \pi$. On the other hand, it is found from Eq. (3.16) that the no-reflection condition for TM waves in purely dielectric media is written as $\theta_\mathrm{i} + \theta_\mathrm{t} = \pi/2$. The vibration direction of the induced electric dipole moment in an isotropic dielectric medium is parallel to the electric field and perpendicular to the wavenumber vector of the transmitted wave. Therefore, one can conclude that the no-reflection effect for TM waves arises when the wavenumber vector of the reflected wave coincides with the vibration direction of the electric dipole moment induced by the transmitted wave as shown in Fig. 3.4.

Next, we examine the physical meaning for purely magnetic media. We assume that a magnetic moment m is located at the origin of the spherical coordinate system as shown in Fig. 3.3. The electric field $\boldsymbol{E}_m = (E_{mr}, E_{m\theta}, E_{m\phi})$ of the electromagnetic wave radiated by the magnetic moment is written as $E_{mr} = 0$, $E_{m\theta} = 0$, and

$$E_{m\phi} = \frac{\pi Z_0 m \mathrm{e}^{\mathrm{i}k_0 r}}{\lambda^2 r} \sin\theta, \tag{3.29}$$

in the far field region [43]. This equation shows that the magnetic moment cannot radiate electromagnetic fields in the direction of the vibration as in the case of the electric dipole moment. Brewster's condition for TE waves is derived from Eq. (3.17) and is written as $\theta_\mathrm{i} + \theta_\mathrm{t} = \pi/2$, which is the same equation as the TM

Brewster condition for purely dielectric media. Hence, one can understand that the TE Brewster condition for purely magnetic media is satisfied when the wavenumber vector of the reflected wave is parallel to the vibration direction of the magnetic moment induced by the transmitted wave.

In case of general isotropic media

We look into the physical meaning of Brewster's condition for general isotropic media [26]. It is necessary to take into account both the radiations from the induced electric dipole moment and magnetic moment.

We suppose that the electric dipole moment p and the magnetic moment m in the medium occupy the volume V. These values are expressed by the electric field and magnetic field of the transmitted wave as the following equations:

$$p = PV = (\varepsilon_{\mathrm{r}} - 1)\varepsilon_0 E_{\mathrm{t}} V, \tag{3.30}$$

$$m = MV = (\mu_{\mathrm{r}} - 1) H_{\mathrm{t}} V, \tag{3.31}$$

where P and M are the polarization and the magnetization in the medium, respectively.

Let us define the electric field of the electromagnetic wave that is radiated by the induced electric dipole moment (magnetic moment) in the direction parallel to the reflected waves as E_p (E_m). We calculate the condition that satisfies $E_p + E_m = 0$ by using Eqs. (3.28)-(3.31).

When the incident wave is TE wave, $E_p + E_m = 0$ is written as

$$-\frac{\pi c_0 Z_0 (\varepsilon_{\mathrm{r}} - 1)\varepsilon_0 E_{\mathrm{t}} V \mathrm{e}^{\mathrm{i}k_0 r}}{\lambda^2 r} \sin\left(\frac{\pi}{2}\right) + \frac{\pi Z_0 (\mu_{\mathrm{r}} - 1) H_{\mathrm{t}} V \mathrm{e}^{\mathrm{i}k_0 r}}{\lambda^2 r} \sin\left[\frac{\pi}{2} - (\theta_{\mathrm{i}} + \theta_{\mathrm{t}})\right] = 0. \tag{3.32}$$

From the relation $E_{\mathrm{t}}/H_{\mathrm{t}} = Z_{\mathrm{r}} Z_0 = \sqrt{(\mu_{\mathrm{r}}\mu_0)/(\varepsilon_{\mathrm{r}}\varepsilon_0)}$, Eq. (3.32) is reduced to

$$\cos(\theta_{\mathrm{i}} + \theta_{\mathrm{t}}) = \frac{\varepsilon_{\mathrm{r}} - 1}{\mu_{\mathrm{r}} - 1}\sqrt{\frac{\mu_{\mathrm{r}}}{\varepsilon_{\mathrm{r}}}}. \tag{3.33}$$

After substitution of Snell's law into Eq. (3.33), we obtain

$$\sin^2\theta_{\mathrm{i}} = \frac{\mu_{\mathrm{r}}^2 - n^2}{\mu_{\mathrm{r}}^2 - 1}, \tag{3.34}$$

which is the same as Eq. (3.27). This implies that Brewster's effect for general isotropic media arises as a result of the destructive interference between the electromagnetic waves produced by the induced electric dipole moment and magnetic moment in the medium.

In the case of TM incidence, $E_p + E_m = 0$ is written as

$$-\frac{\pi c_0 Z_0(\varepsilon_\mathrm{r}-1)\varepsilon_0 E_\mathrm{t} V \mathrm{e}^{\mathrm{i}k_0 r}}{\lambda^2 r}\sin\left[\frac{\pi}{2}+(\theta_\mathrm{i}+\theta_\mathrm{t})\right]+\frac{\pi Z_0(\mu_\mathrm{r}-1)H_\mathrm{t} V \mathrm{e}^{\mathrm{i}k_0 r}}{\lambda^2 r}\sin\left(\frac{\pi}{2}\right)=0. \tag{3.35}$$

Repeating a similar procedure to the above discussion, we have

$$\sin^2\theta_\mathrm{i} = \frac{\varepsilon_\mathrm{r}^2 - n^2}{\varepsilon_\mathrm{r}^2 - 1}. \tag{3.36}$$

This equation is also the same as Eq. (3.27).

3.2 Magnetic metamaterials

We showed in the previous section that there exists Brewster's condition for TE waves in magnetic media. We now analyze properties of an array of SRRs [2] that are one of the most common meta-atoms used to fabricate magnetic metamaterials, and examine whether TE Brewster's effect can be observed for the SRR array metamaterial. The characteristics of the SRR array metamaterial are evaluated by theoretical, numerical, and experimental analyses.

3.2.1 Theoretical analysis of SRR

We consider an array of metallic rings as shown in Fig. 3.5(a). When a time-varying magnetic field $B = \mu_0 H$ that goes through the rings is applied, an electromotive force is induced and a circular current I flows in each ring. Thus, magnetic moments m are induced. If the size of the ring and the separation between neighboring rings are much smaller than the wavelength of the electromagnetic wave, the array of the rings behaves as an artificial magnetic medium.

We calculate the effective relative permeability μ_r of the array of the rings. From the equilibrium between the electromotive force induced by the applied magnetic

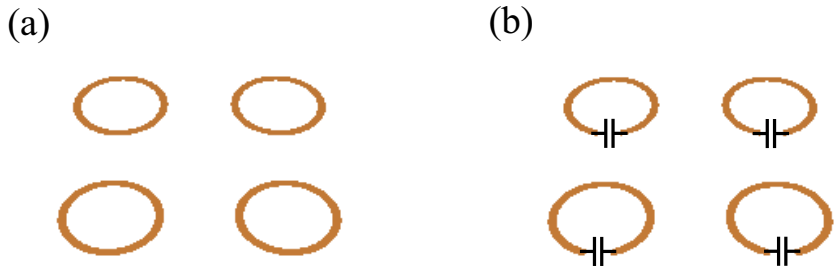

Figure 3.5: Arrays of (a) metallic rings and (b) metallic rings loaded with capacitors.

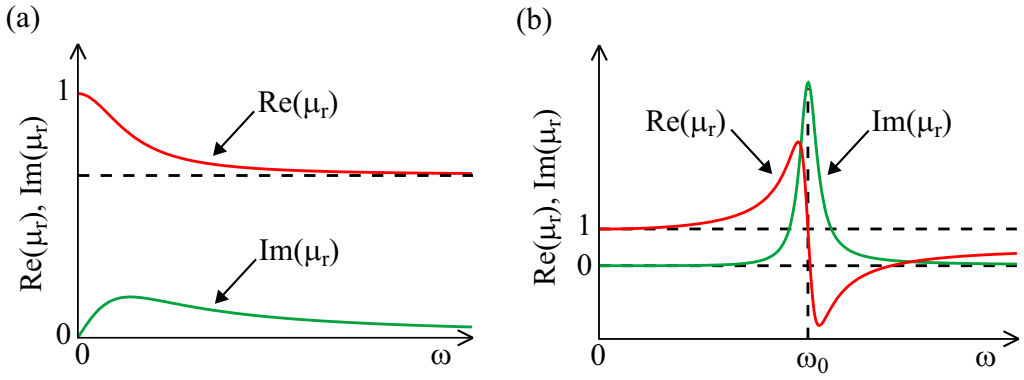

Figure 3.6: Relative permeabilities of (a) array of metallic rings and (b) array of metallic rings loaded with capacitors.

field and the voltage drop in the ring, we have

$$\mathrm{i}\omega\mu_0 HS - Z(\omega)I = 0, \tag{3.37}$$

where $Z(\omega)$ is the impedance in the ring, which is described by an input impedance of a loop antenna [43], and S is the area surrounded by the ring. When the size of the ring is much smaller than the wavelength, $Z(\omega)$ is reduced to

$$Z(\omega) = R(\omega) - \mathrm{i}\omega L, \tag{3.38}$$

where $R(\omega)$ [$\propto (r\omega)^4$, r is the radius of the ring] is the input resistance, or the radiation resistance, and L is the input inductance of the loop antenna. Both the parameters R and L are positive values. The magnetization M in the array is given

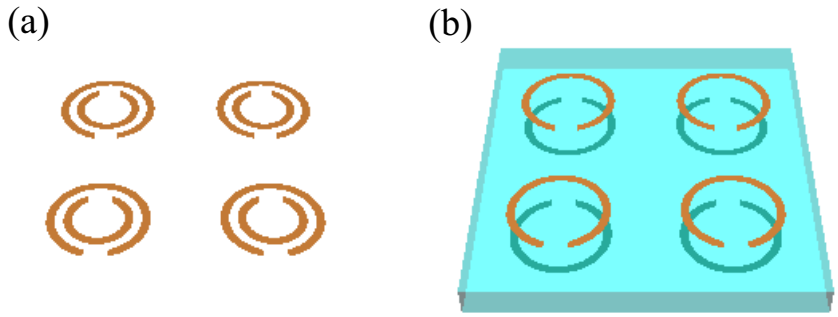

Figure 3.7: Arrays of (a) ECSRRs and (b) BCSRRs.

by

$$M = Nm = NIS, \tag{3.39}$$

where N is the number density of the ring. Substituting Eqs. (3.37) and (3.39) into the relation $\mu_{\rm r} = 1 + (M/H)$, the following equation is derived:

$$\mu_{\rm r} = 1 + \frac{{\rm i}\omega\mu_0 NS^2}{Z(\omega)} = 1 + \frac{{\rm i}\omega\mu_0 NS^2}{R(\omega) - {\rm i}\omega L}. \tag{3.40}$$

This equation is similar to the Debye dispersion relation. The real part of $\mu_{\rm r}$ ranges between 1 and $1 - (\mu_0 NS/L)$ as shown in Fig. 3.6(a).

In order to significantly change the relative permeability from unity, we should utilize an array of rings loaded with capacitors C as shown in Fig. 3.5(b). The impedance in the ring is written as

$$Z(\omega) = R(\omega) - {\rm i}\omega L - \frac{1}{{\rm i}\omega C}, \tag{3.41}$$

After substitution of Eq. (3.41) into Eq. (3.40), we obtain

$$\mu_{\rm r} = 1 + \frac{{\rm i}\omega\mu_0 NS^2}{R(\omega) - {\rm i}\omega L - 1/({\rm i}\omega C)}. \tag{3.42}$$

This equation resembles the Lorentz dispersion equation. The real part of the relative permeability significantly varies from unity and even becomes negative value around the resonance frequency $\omega_0 = 1/\sqrt{LC}$ as shown in Fig. 3.6(b).

A capacitor-loaded ring can be fabricated by making a cut in the ring. When the resonance frequency needs to be reduced for a fixed radius of the ring, we should

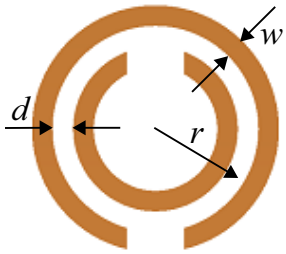

Figure 3.8: Geometry of SRR. Thickness of SRR is t.

increase the capacitance in the ring. There are several kinds of ring structures where large capacitance can be obtained, for example, edge-coupled SRR [2] (ECSRR) and broadside-coupled SRR [44] (BCSRR) shown in Fig. 3.7. The capacitance in the BCSRR can be larger than that in the ECSRR. When we fabricate these SRR structures for a fixed resonance frequency, the radius of the BCSRR can become smaller than that of the ECSRR. That is, the radiation resistance of the BCSRR can be smaller than that of the ECSRR. Thus, lower-loss magnetic metamaterials are able to be realized by utilizing the BCSRRs rather than the ECSRRs. On the other hand, it is more difficult to fabricate the BCSRR than the ECSRR. We adopt an array of the ECSRR as a magnetic metamaterial because of its easy-to-fabricate structure. Hereafter, we simply refer to ECSRR as SRR.

It is convenient to have an analytical approximation for the resonance frequency of the SRR. We calculate the inductance and capacitance in the SRR and derive the resonance frequency.

Let us define the geometry of the SRR as shown in Fig. 3.8. First, we calculate the inductance of the SRR. A high-frequency current flows over a surface of a conductor; therefore, the inductance of the SRR is nearly equal to the external inductance of the two rings. The external inductance of the rings is given by the Neumann formula [45] and is written as

$$L = \mu_0 r \left(\ln \frac{16r}{w} - 2 \right), \tag{3.43}$$

where $r \gg w, d$ is assumed. Second, we calculate the capacitance between the two rings. When $r \gg w, d$ is satisfied, the capacitance is approximated by that between

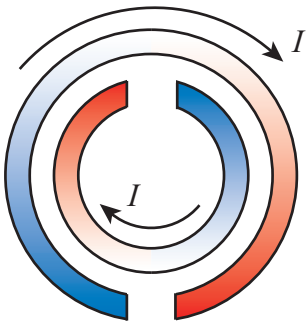

Figure 3.9: Charge distribution in SRR when circular current flows. Red (blue) color represents positive (negative) charge.

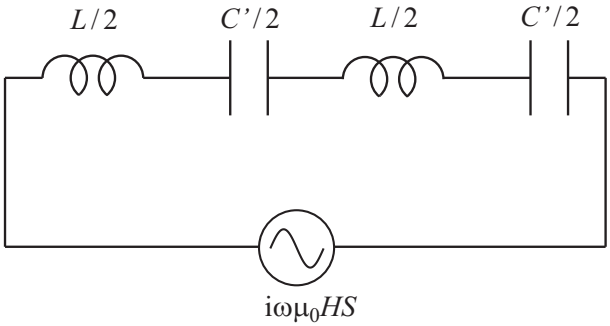

Figure 3.10: Lumped circuit model of SRR. Radiation resistance and ohmic loss are omitted for simplicity.

two linear conductors. The formulas for calculating the wiring capacitances are introduced by Sakurai *et al.* [46]. From this formula, the capacitance between the two rings is found to be

$$C = \varepsilon_0 \left[\frac{2.3\pi r t}{d} + 1.40(2\pi r + t) \left(\frac{2w}{d} \right)^{0.222} + 1.03d \left(\frac{2w}{d} \right)^{0.728} \right]. \tag{3.44}$$

Supposing that the SRR is fabricated on a substrate whose relative permittivity is ε_r and that the thickness t of the ring is much smaller than w and d, the capacitance becomes

$$C' = \frac{1 + \varepsilon_\mathrm{r}}{2} C. \tag{3.45}$$

Finally, we determine the resonance frequency of the SRR. When the circular cur-

rent flows around the ring of the SRR, the charge is distributed as if the capacitance between the two rings is divided in half as shown in Fig. 3.9. Therefore, it is found that the lumped circuit model of the SRR is expressed as Fig. 3.10 and that the resonance frequency is given by

$$f_0 = \frac{1}{2\pi\sqrt{L(C'/4)}} = \frac{1}{\pi\sqrt{LC}}\sqrt{\frac{2}{1+\varepsilon_{\mathrm{r}}}}. \tag{3.46}$$

3.2.2 Numerical analysis of SRR

The theoretical analysis of the SRR showed that the relative permeability can be significantly changed from unity by utilizing the SRR array metamaterial. Brewster's effect for TE waves arises for media where magnetic responses are larger than electric responses. Therefore, it is necessary to examine the relative permittivity of the SRR array as well as the relative permeability. We calculate the relative permittivity and permeability of the SRR array using an FDTD method.

Simulated system

We analyzed an array of rectangular SRRs, as shown in Fig. 3.11(a), for the purpose of simplicity in calculation. The SRR was supposed to be made of copper whose conductivity was $5.8 \times 10^7\,\mathrm{S/m}$. Figure 3.11(b) shows the unit cell of the SRR array. Periodic boundary conditions were adopted in the x- and y-directions to achieve two dimensional array of the SRRs. The SRR array was a monolayer in the z-direction. A monochromatic plane electromagnetic wave (amplitude of the electric field was $1.0\,\mathrm{V/m}$) was introduced into the SRR array. The space and time step sizes were $0.4\,\mathrm{mm}$ and $0.65\,\mathrm{ps}$, respectively.

Method for calculating medium parameters

The relative permittivity and permeability of the SRR array can be calculated by analyzing the electromagnetic fields around the SRR [47].

First, we describe a way to determine the relative permittivity. Here, we calculate only the x-component of the electric response because the direction of the incident electric field is the x-direction. The relative permittivity can be figured

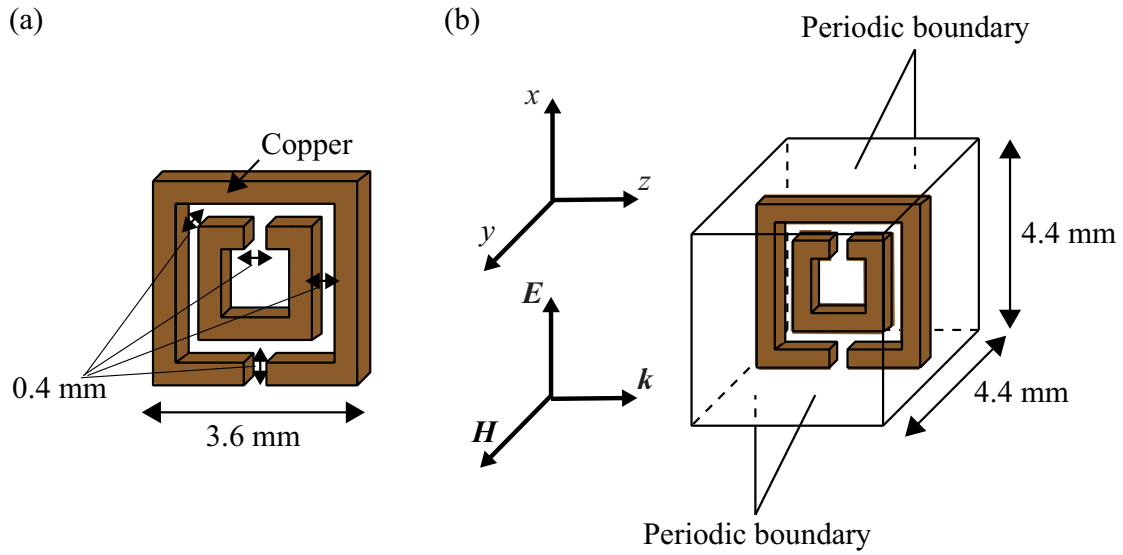

Figure 3.11: (a) Geometry of the rectangular SRR. (b) Unit cell of the SRR array used in the FDTD simulation.

from the charge distribution in the SRR. The charge in a volume surrounded by a closed surface S is given by Gauss's law:

$$q = \int_S \boldsymbol{D} \cdot \mathrm{d}\boldsymbol{S}, \tag{3.47}$$

where $\mathrm{d}\boldsymbol{S}$ is an area element directed outside the volume. The x-component of the electric dipole moment in the single SRR is written as

$$p_x = \int_V \mathrm{d}q(\boldsymbol{r})\, x, \tag{3.48}$$

where V represents a volume that includes the single SRR, $\boldsymbol{r} = (x, y, z)$ is the position vector whose origin is the center of the SRR. Supposing that the number density of the SRR is N, the relative permittivity is given by

$$\varepsilon_\mathrm{r} = 1 + \frac{\tilde{P}_x}{\varepsilon_0 \tilde{E}_x} = 1 + \frac{N\tilde{p}_x}{\varepsilon_0 \tilde{E}_x}. \tag{3.49}$$

Here P_x is the x-component of the polarization, E_x is the average electric field in the x-direction, and the tilde represents the complex amplitude. The relative permittivity of the SRR array can be determined by calculating the electric flux density around the SRR with the FDTD simulation and using Eqs. (3.47)-(3.49).

Then we show how to calculate the relative permeability. We analyze only the y-component of the magnetic response because the direction of the incident magnetic field is the y-direction. The relative permeability is derived from the current distribution in the SRR. The current that flows through an area bounded by a closed line C is given by Ampère's law:

$$I = \int_C \boldsymbol{H} \cdot \mathrm{d}\boldsymbol{l}, \tag{3.50}$$

where $\mathrm{d}\boldsymbol{l}$ is a line element of C. The y-component of the magnetic moment in the single SRR is written as

$$m_y = \left(\frac{1}{2} \int_{C'} \boldsymbol{r} \times I \, \mathrm{d}\boldsymbol{s} \right)_y, \tag{3.51}$$

where C' represents the ring of the SRR and $\mathrm{d}\boldsymbol{s}$ is a line element of C'. We have the relative permeability from the following equation:

$$\mu_\mathrm{r} = 1 + \frac{\tilde{M}_y}{\tilde{H}_y} = 1 + \frac{N\tilde{m}_y}{\tilde{H}_y}. \tag{3.52}$$

Here M_y is the y-component of the magnetization, and H_y is the average magnetic field in the y-direction. The relative permeability of the SRR array can be found by calculating the magnetic field around the SRR with the FDTD analysis and using Eqs. (3.50)-(3.52).

Results

Figure 3.12 shows the numerically calculated ε_r and μ_r of the SRR array as a function of frequency f. The relative permittivity can be regarded as unity for any frequency, and $\mathrm{Re}(\mu_\mathrm{r})$ and $\mathrm{Im}(\mu_\mathrm{r})$ can be approximated by the Lorentz dispersion and absorption functions. The resonance frequency of the SRR array is found to be 10.0 GHz. The SRR array behaves as a almost purely magnetic medium with finite losses near the resonance frequency.

Figure 3.13 shows the current distribution in the SRR as a function of time. The currents I_{x1}, I_{x2}, I_{z1}, and I_{z2} are defined in Fig. 3.13(a). We show the currents at 5.0 GHz, 10.0 GHz, and 15.0 GHz in Figs. 3.13(b)-(d), respectively. At 10.0 GHz,

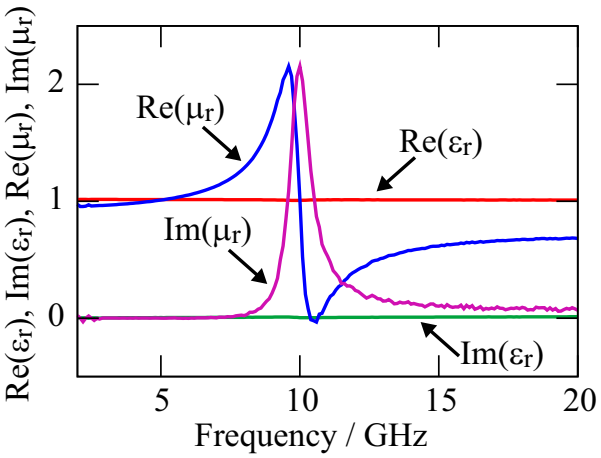

Figure 3.12: Complex relative permittivity ε_r and complex relative permeability μ_r versus frequency for the SRR array.

which is the resonance frequency, the currents flow in phase and the amplitudes of the currents are larger than the other cases. At 5.0 GHz and 15.0 GHz, not only are the amplitudes of the currents small, but the currents also flow out of phase. The current distributions, also, reveal that the SRR array metamaterial shows a significant magnetic response at 10.0 GHz.

We show snapshots of the charge distributions in the SRR in Fig. 3.14. Figure 3.14(b) that shows the charge distribution at 10.0 GHz is similar to Fig. 3.9. This indicates that the circular current flows in the SRR at 10.0 GHz. The charge distribution at 5.0 GHz, which is different from Fig. 3.9, shows that an electric dipole moment in the x-direction is induced in the SRR; the SRR responds only to the electric field and not to the magnetic field. One can see from the charge distribution that the circular current flows also at 15.0 GHz, while the charge density is smaller than that in the case of 10.0 GHz. This implies that the circular current at 15.0 GHz is smaller than that in the case of 10.0 GHz. The calculation results of the charge distributions are consistent with those of the medium parameters and current distributions.

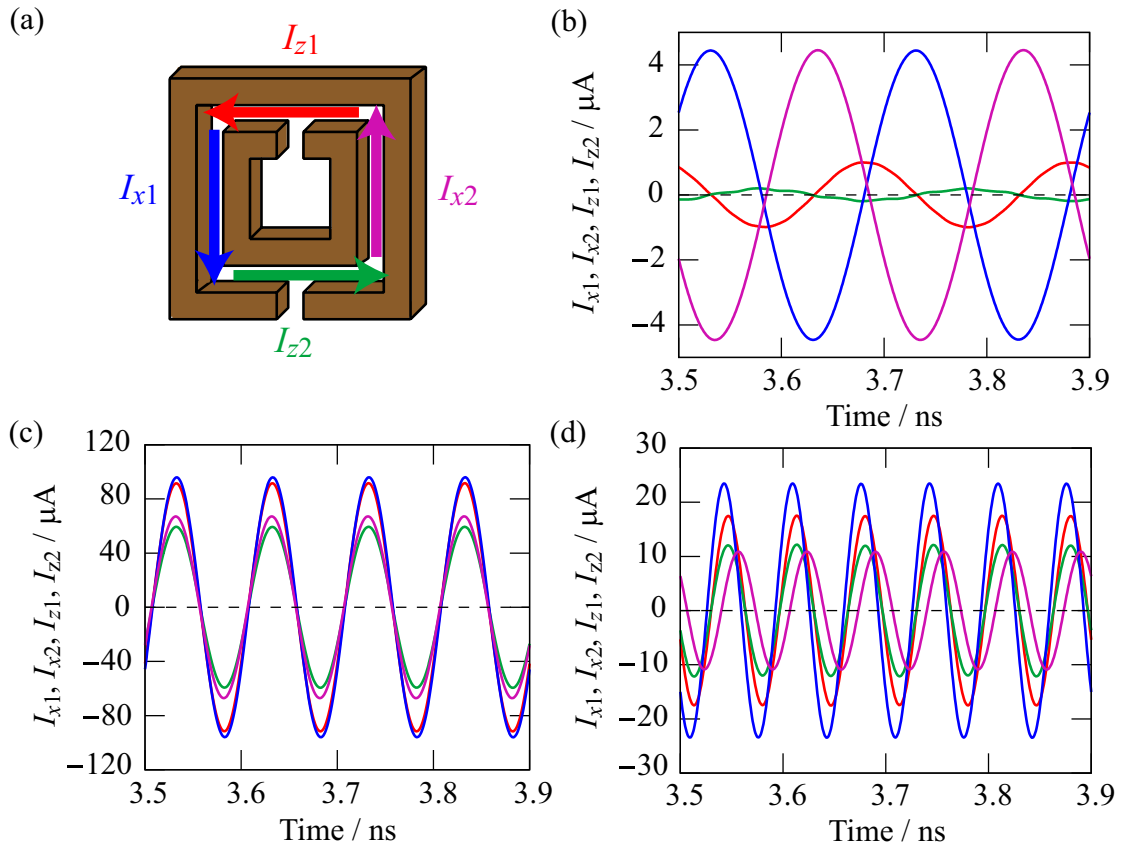

Figure 3.13: Current distributions in the SRR. (a) Definition of each current. (b)-(d) The currents versus time at 5.0 GHz, 10.0 GHz, and 15.0 GHz, respectively.

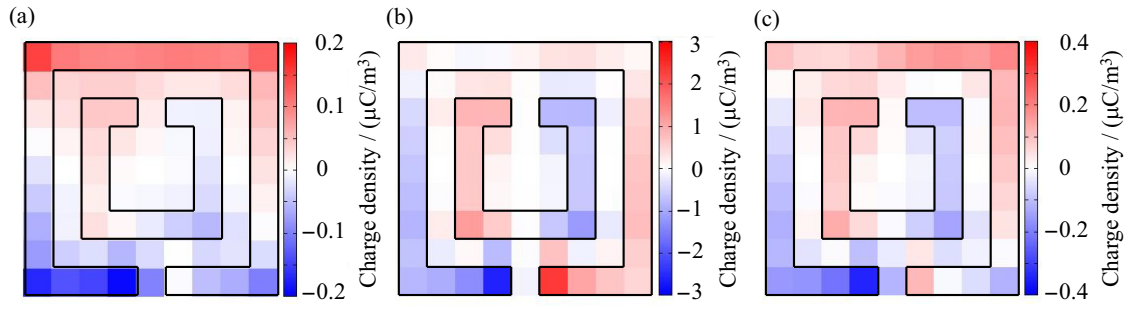

Figure 3.14: Charge distributions in the SRR at (a) 5.0 GHz, (b) 10.0 GHz, and (c) 15.0 GHz.

Discussion

Resonance frequency The resonance frequency determined by the FDTD analysis is 10.0 GHz. On the other hand, the resonance frequency calculated from Eq. (3.46) is 11.7 GHz. The former value is 14.5 % smaller than the latter value. We find that the LC circuit model is helpful in the estimation of the resonance frequency.

Pseudo Brewster's angle The SRR array was found to be a magnetic medium with $\mu_\mathrm{r} \neq 1$ and $\varepsilon_\mathrm{r} \simeq 1$ near the resonance frequency. It seems that Brewster's effect for TE waves can be observed for the SRR array near the resonance frequency. However, although the SRR metamaterial has finite losses, we have not considered Brewster's effect for lossy media yet. Medium losses were not taken into account in Sec. 3.1. We discuss Brewster's effect for lossy magnetic media with $\varepsilon_\mathrm{r} = 1$ and consider ease of observing Brewster's effect.

We suppose that ε_r equals unity and calculate reflectivities for various μ_r from Eq. (3.19). Figure 3.15(a) shows reflectivities for TE waves when μ_r is equal to $1.5 + \mathrm{i}0.01$, $1.5 + \mathrm{i}0.1$, and $1.5 + \mathrm{i}1.0$. The difference among these three cases is the imaginary part of μ_r, and the real parts of μ_r are the same values. The reflectivities do not vanish for any incident angle; however, they reach minimum values at a particular incident angle.[1] The incident angle for the minimum reflectivity is called the pseudo-Brewster angle [48, 49]. Figure 3.15(a) clarifies that the larger the imaginary part, the larger the reflectivity at the pseudo-Brewster angle.

Figure 3.15(b) shows reflectivities for TE waves when μ_r equals $1.5 + \mathrm{i}0.01$ and $0.5 + \mathrm{i}0.01$. The difference between these two cases is the real part of μ_r. The imaginary parts of μ_r are the same values. One can see that the minimum reflectivity in the former case is smaller than that in the latter case. Brewster's effect is related to the ratio of the imaginary part of μ_r to the real part.

Based on the above discussion, we find that a significant depression in the power reflectivity can be detected around the pseudo-Brewster angle if the dispersive prop-

[1] This does not imply that the reflectivity for lossy media never vanish. Note that we made a assumption: $\varepsilon_\mathrm{r} = 1$. The no-reflection phenomena can be observed even for lossy media if the medium parameters satisfy Eq. (3.27).

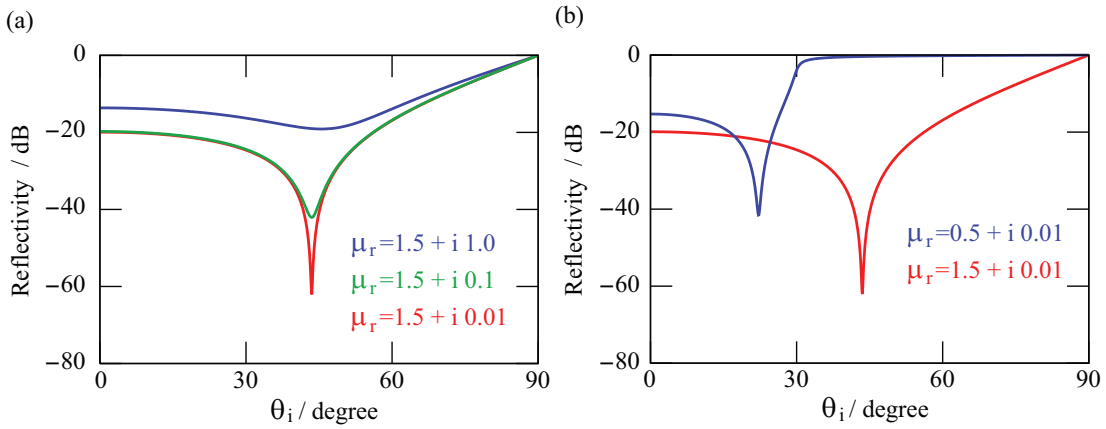

Figure 3.15: Power reflectivities for TE waves as a function of incident angle $\theta_{\rm i}$. Reflectivities are calculated for (a) $(\varepsilon_{\rm r}, \mu_{\rm r}) = (1, 1.5 + {\rm i}0.01)$, $(1, 1.5 + {\rm i}0.1)$, $(1, 1.5 + {\rm i}1.0)$ and (b) $(\varepsilon_{\rm r}, \mu_{\rm r}) = (1, 0.5 + {\rm i}0.01)$, $(1, 1.5 + {\rm i}0.01)$.

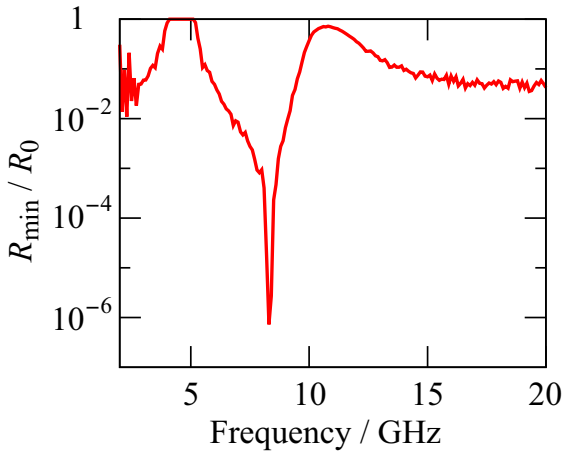

Figure 3.16: Ratio of the minimum power reflectivity $R_{\rm min}$ to the power reflectivity R_0 for normal incidence versus frequency for the SRR array metamaterial.

erty of the SRR metamaterial dominates the dissipation. In order to estimate the magnitude of the depression, we introduce the ratio of the minimum power reflectivity $R_{\rm min}$ to the power reflectivity for normal incidence, R_0. The smaller the ratio $R_{\rm min}/R_0$, the more easily Brewster's effect can be observed in the experiments.

Figure 3.16 gives the frequency dependence of $R_{\rm min}/R_0$ that is calculated from

the results of the FDTD simulation shown in Fig. 3.12. The ratio $R_{\min}/R_0$ reduces in a narrow region just below the resonance frequency. The frequency width where $R_{\min}/R_0 < 10^{-4}$ is satisfied is about 340 MHz, which corresponds to the fractional bandwidth of 4.1 %. Brewster's effect for TE waves could easily be detected in that narrow frequency region.

3.2.3 Measurement of admittance of single SRR

The FDTD simulation revealed that the SRR metamaterial behaves as a magnetic medium with $\varepsilon_{\mathrm{r}} \simeq 1$ around the resonance frequency of the SRR and that the TE Brewster effect could easily be observed in the narrow frequency region just below the resonance frequency. Before the experiment of observing the TE Brewster effect, it is necessary to develop a method for designing the SRR that has a desired resonance frequency. That is, we need to experimentally examine the accuracy of the LC circuit model given by Eq. (3.46). In this section, we determine the resonance frequency by measuring the admittance of the single SRR and compare the measured resonance frequency with the frequency calculated from Eq. (3.46).

Theory of admittance measurement

We describe how to measure the admittance of the single SRR at the microwave frequencies.

Let us suppose that a load with impedance Z, which represents the single SRR, is connected to the end of a transmission line (characteristic impedance: Z_0) as shown in Fig. 3.17. The voltage and current in the transmission line are written as

$$V(z) = V_{\mathrm{i}}\mathrm{e}^{-\mathrm{i}(\omega t - kz)} + V_{\mathrm{r}}\mathrm{e}^{-\mathrm{i}(\omega t + kz)}, \tag{3.53}$$

$$I(z) = \frac{V_{\mathrm{i}}}{Z_0}\mathrm{e}^{-\mathrm{i}(\omega t - kz)} - \frac{V_{\mathrm{r}}}{Z_0}\mathrm{e}^{-\mathrm{i}(\omega t + kz)}. \tag{3.54}$$

Since the load impedance is Z, we have

$$Z = \frac{V(l)}{I(l)} = \frac{V_{\mathrm{i}}\mathrm{e}^{\mathrm{i}kl} + V_{\mathrm{r}}\mathrm{e}^{-\mathrm{i}kl}}{V_{\mathrm{i}}\mathrm{e}^{\mathrm{i}kl} - V_{\mathrm{r}}\mathrm{e}^{-\mathrm{i}kl}} Z_0. \tag{3.55}$$

The input impedance at $z = 0$ is given by

$$Z_{\mathrm{in}} = \frac{V(0)}{I(0)} = \frac{V_{\mathrm{i}} + V_{\mathrm{r}}}{V_{\mathrm{i}} - V_{\mathrm{r}}} Z_0. \tag{3.56}$$

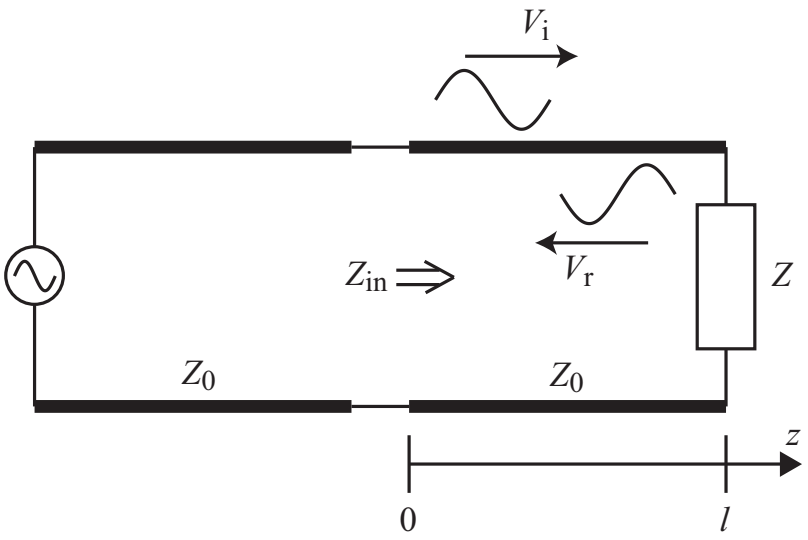

Figure 3.17: Transmission line ended with load Z.

From Eqs. (3.55) and (3.56), we obtain

$$Z = \frac{Z_\mathrm{in}\cos(2\pi f t_\mathrm{d}) + \mathrm{i}Z_0\sin(2\pi f t_\mathrm{d})}{Z_0\cos(2\pi f t_\mathrm{d}) + \mathrm{i}Z_\mathrm{in}\sin(2\pi f t_\mathrm{d})}Z_0, \tag{3.57}$$

where $t_\mathrm{d} = (kl)/(2\pi f)$ is an electrical delay of the transmission line with length l. From this equation, one sees that the load admittance $Y = 1/Z$ can be determined by measuring the input impedance Z_in and the electrical delay t_d.

The input impedance Z_in can be found by a measurement of the reflection coefficient. The voltage reflection coefficient at $z = 0$ is given by [50]

$$\Gamma = \frac{Z_\mathrm{in} - Z_0}{Z_\mathrm{in} + Z_0}. \tag{3.58}$$

This equation is reduced to

$$Z_\mathrm{in} = \frac{1+\Gamma}{1-\Gamma}. \tag{3.59}$$

The electrical delay t_d can be determined by measuring the input impedance of the transmission line ended with short. The input impedance of this transmission line is given by

$$Z_\mathrm{s} = -\mathrm{i}Z_0\tan(2\pi f t_\mathrm{d}) = -\mathrm{i}Z_0\tan\theta_\mathrm{d}, \tag{3.60}$$

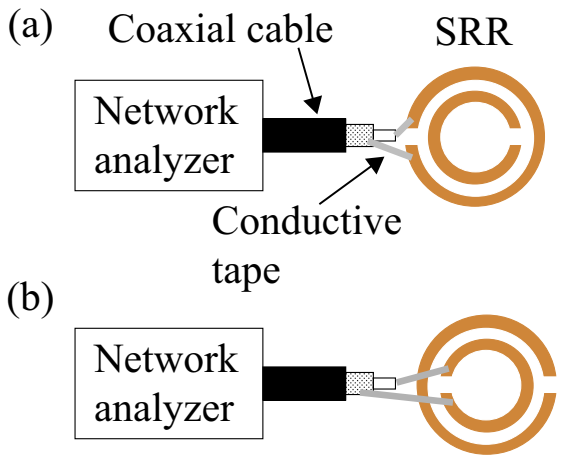

Figure 3.18: Schematic diagram of the experimental setup for measuring the admittance of the single SRR. Coaxial cable is connected (a) to the outer ring and (b) to the inner ring.

where

$$\theta_{\mathrm{d}} = 2\pi f t_{\mathrm{d}}. \tag{3.61}$$

Thus, one can calculate θ_{d} from a measurement of Z_{s}. Since θ_{d} is directly proportional to the frequency f, the electrical delay is determined from a slope of the θ_{d}-f characteristic.

Measurement system

We used an admittance measurement system as shown in Fig. 3.18 to examine the resonance frequency of the single SRR. The following is the detail of the experimental setup.

Coaxial cable A coaxial cable (RG223/U, $Z_0 = 50\,\Omega$) was used as the transmission line. We set the length of the transmission line at 2.0 cm. The one end of the coaxial cable was connected to the transmitting port of the network analyzer and the other end was connected to the SRR. The inner conductor of the coaxial cable was soldered to the one end of the outer (inner) ring of the SRR and the outer

Table 3.1: Structural parameters of the SRRs used in Sec. 3.2.3.

	r/mm	w/mm	d/mm	t/μm
SRR 1	18.1	5.05	4.87	35
SRR 2	11.8	2.50	1.63	35
SRR 3	6.75	1.50	0.98	35
SRR 4	4.98	0.986	0.891	35

conductor was soldered to the other end by using a conductive tape as shown in Fig. 3.18.

SRR The SRRs were fabricated by using printed circuit board technology. The thicknesses of the copper layer and the FR-4 substrate (relative permittivity: 4.5) of the printed circuit board were 35 μm and 1.6 mm, respectively. We prepared four types of SRRs. The structural parameters of the SRRs are shown in Tab. 3.1.

Network analyzer A network analyzer (Advantest, R3765BG) was used as the microwave generator and detector. It can generate signals ranging from 300 kHz to 3.8 GHz and enables us to measure both the complex reflectivity and the complex transmissivity.

Method

Calibration One-port full calibration was performed at the transmitting port of the network analyzer in order to eliminate errors in the measurement [51]. BNC-type short, open, and 50 Ω load standards were used for the calibration.

Measurement of electrical delay of transmission line We fabricated the transmission line ended with short by soldering the inner conductor of the coaxial cable to the outer conductor. We connected this transmission line to the transmitting port of the network analyzer and measured the voltage reflection coefficient at the transmitting port. The measured reflection coefficient was converted into

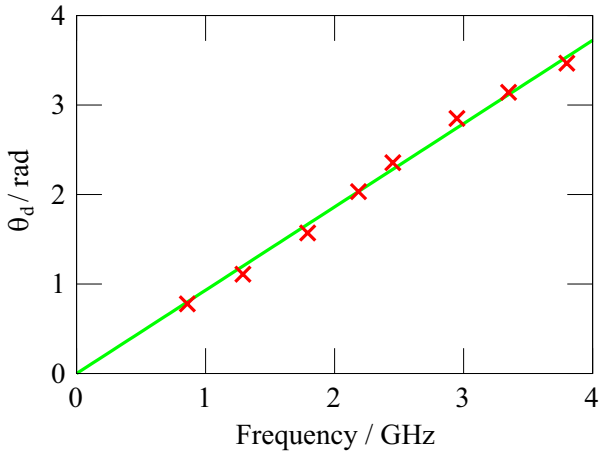

Figure 3.19: Frequency dependence of θ_d (red crosses). The green line is the fitted line. The slope of the line corresponds to the electrical delay.

θ_d using Eqs. (3.59) and (3.60). The electrical delay of the transmission line was determined from Eq. (3.61), or the frequency dependence of θ_d.

Measurement of admittance of single SRR We connected the transmission line ended with the single SRR to the transmitting port of the network analyzer and carried out a measurement of the reflection coefficient. The input impedance of the transmission line was calculated from Eq. (3.59). The admittance of the single SRR was determined from Eq. (3.57) using the obtained electrical delay and input impedance.

Results

Electrical delay of transmission line The dependence of θ_d on the frequency f is shown in Fig. 3.19 as red crosses. It is seen that θ_d varies linearly with f. Fitting Eq. (3.61) to the measured θ_d-f characteristic, the electrical delay t_d is found to be 148.1 ps.

Admittance of single SRR Figures 3.20(a)-(c) respectively show the admittances of SRRs 1-3 when the coaxial cables are connected to the outer rings of the

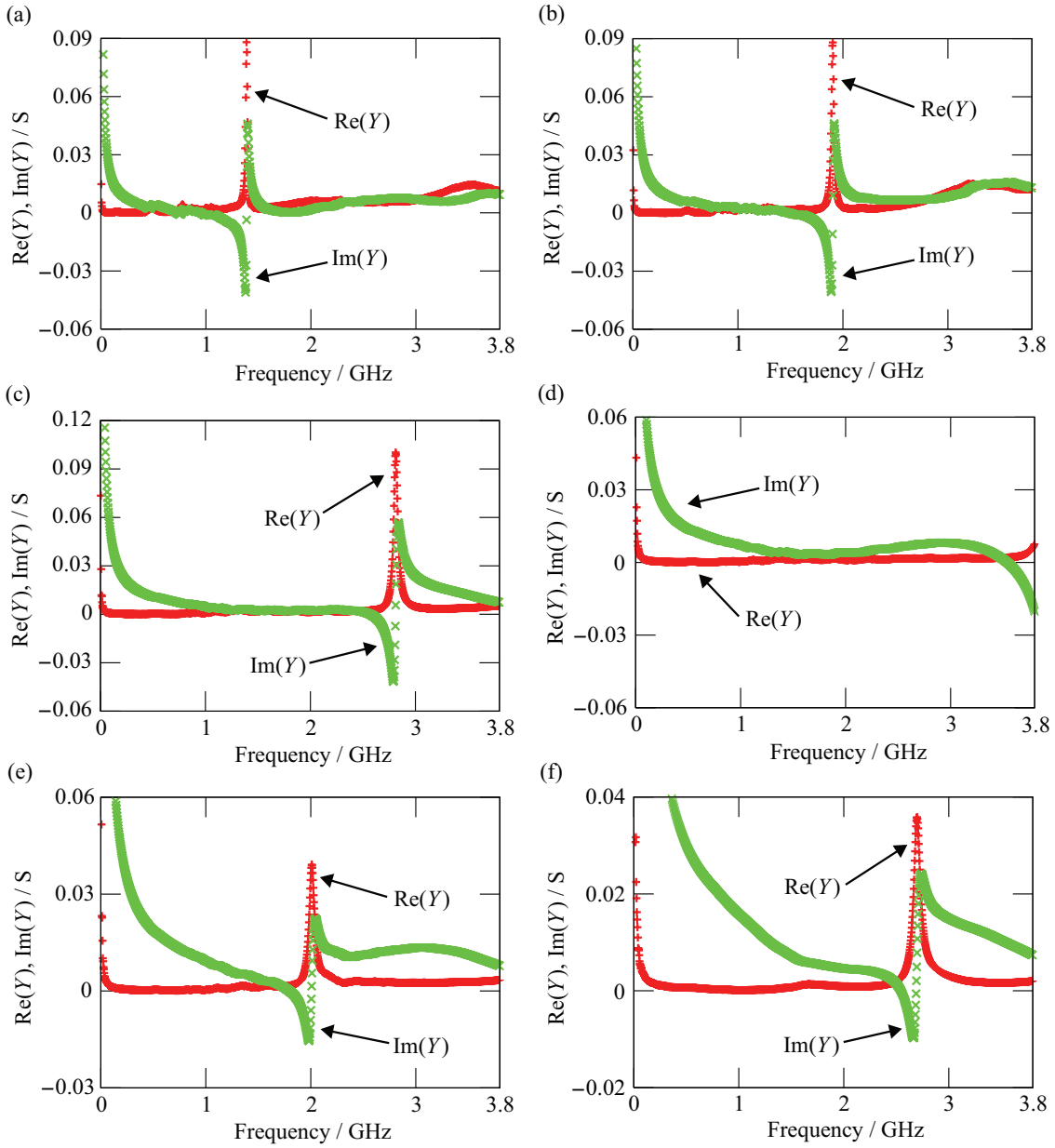

Figure 3.20: (a)-(d) Measured admittances of SRRs 1-4 when the coaxial cables are connected to the outer rings of the SRRs and (e)-(f) those of SRRs 3-4 when the coaxial cables are connected to the inner rings of the SRRs.

SRRs. The real part of the admittance becomes maximal value and the imaginary part vanishes at a certain non-zero frequency in each case. That is, the LC series resonances of the SRRs are observed. The measured resonance frequencies [resonance frequencies calculated from Eq. (3.46)] of SRRs 1-3 are 1.38 GHz (0.674 GHz), 1.90 GHz (0.933 GHz), and 2.78 GHz (1.64 GHz), respectively. The ratios of the measured resonance frequencies to the calculated resonance frequencies are 2.05, 2.04, and 1.70, respectively. The differences between the measured and calculated frequencies are quite large.

Figure 3.20(d) gives the admittance of SRR 4 in the case where the coaxial cable is connected to the outer ring. The LC series resonance phenomenon do not appear in the operating frequency region. The resonance frequency seems to be larger than 3.8 GHz.

Figures 3.20(e) and 3.20(f) respectively show the admittances of SRRs 3 and 4 when the coaxial cables are connected to the inner rings of the SRRs. The measured (calculated) resonance frequencies are 2.00 GHz (1.64 GHz) and 2.70 GHz (2.24 GHz). The measured value is 22.0 % (20.5 %) larger than the calculated value in the case of SRR 3 (SRR 4). The measured and calculated values are not so different from each other.

Discussion

The admittances of the single SRR when the coaxial cables are connected to the outer ring and to the inner ring are different from each other. The resonance frequency of the later case is closer to the frequency calculated from the LC circuit model, which is in good agreement with the FDTD analysis. The difference between the measured resonance frequencies in the two cases is caused by the way to apply the voltage to the SRR. The method for applying the voltage in this experiment may not accurately realize the interaction between an electromagnetic wave and an SRR array. However, it is experimentally confirmed at least that the LC circuit model is useful for estimating the order of the resonance frequency.

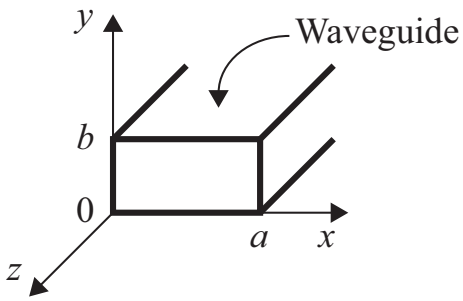

Figure 3.21: Geometry of coordinate system used for analyzing electromagnetic fields in rectangular waveguide. Dimension of the cross section of the waveguide is $a \times b$.

3.2.4 Measurement of electromagnetic properties of SRR array

We experimentally investigate characteristics of an SRR array in this section. The SRR array are designed based on the *LC* circuit model, Eq. (3.46). Not only the resonance frequency of the SRR array but also its relative permittivity and permeability are evaluated by measuring the transmission spectrum of the SRR array placed in a rectangular waveguide.

Theory for determining relative permittivity and permeability from scattering parameters

The relative permittivity and permeability of the SRR array can be determined from the transmission spectrum. First, the wavenumber and wave impedance in a rectangular waveguide are analyzed, then the relations among the scattering parameters (S parameters), wavenumber, and wave impedance are calculated. Finally, the method for estimating the relative permittivity and permeability is described.

Wavenumber and wave impedance in rectangular waveguide We derive the wavenumber k in the longitudinal direction and the wave impedance Z for a fundamental mode, the TE_{10} mode, in a rectangular waveguide.

Let us define a orthogonal coordinate system for a rectangular waveguide as shown in Fig. 3.21. We start with the Maxwell equations:

$$\mathrm{rot}\,\boldsymbol{E} = -\frac{\partial \boldsymbol{B}}{\partial t}, \quad \mathrm{rot}\,\boldsymbol{H} = \frac{\partial \boldsymbol{D}}{\partial t}, \quad \mathrm{div}\,\boldsymbol{D} = 0, \quad \mathrm{div}\,\boldsymbol{B} = 0. \tag{3.62}$$

The constitutive equations of an anisotropic medium are given by

$$\boldsymbol{D} = [\varepsilon]\boldsymbol{E}, \quad \boldsymbol{B} = [\mu]\boldsymbol{H}, \tag{3.63}$$

where $[\varepsilon]$ and $[\mu]$ are the permittivity tensor and permeability tensor, respectively.

Supposing that $[\varepsilon]$ and $[\mu]$ are written as diagonal matrices:

$$[\varepsilon] = \begin{bmatrix} \varepsilon_x & 0 & 0 \\ 0 & \varepsilon_y & 0 \\ 0 & 0 & \varepsilon_z \end{bmatrix} = \varepsilon_0 \begin{bmatrix} \varepsilon_{\mathrm{r}x} & 0 & 0 \\ 0 & \varepsilon_{\mathrm{r}y} & 0 \\ 0 & 0 & \varepsilon_{\mathrm{r}z} \end{bmatrix}, \tag{3.64}$$

$$[\mu] = \begin{bmatrix} \mu_x & 0 & 0 \\ 0 & \mu_y & 0 \\ 0 & 0 & \mu_z \end{bmatrix} = \mu_0 \begin{bmatrix} \mu_{\mathrm{r}x} & 0 & 0 \\ 0 & \mu_{\mathrm{r}y} & 0 \\ 0 & 0 & \mu_{\mathrm{r}z} \end{bmatrix}, \tag{3.65}$$

Eq. (3.62) is reduced to

$$\left.\begin{aligned} &\frac{\partial E_z}{\partial y} - \mathrm{i}kE_y = \mathrm{i}\omega\mu_x H_x, \ \mathrm{i}kE_x - \frac{\partial E_z}{\partial x} = \mathrm{i}\omega\mu_y H_y, \ \frac{\partial E_y}{\partial x} - \frac{\partial E_x}{\partial y} = \mathrm{i}\omega\mu_z H_z, \\ &\frac{\partial H_z}{\partial y} - \mathrm{i}kH_y = -\mathrm{i}\omega\varepsilon_x E_x, \ \mathrm{i}kH_x - \frac{\partial H_z}{\partial x} = -\mathrm{i}\omega\varepsilon_y E_y, \ \frac{\partial H_y}{\partial x} - \frac{\partial H_x}{\partial y} = -\mathrm{i}\omega\varepsilon_z E_z, \\ &\varepsilon_x\frac{\partial E_x}{\partial x} + \varepsilon_y\frac{\partial E_y}{\partial y} + \mathrm{i}\varepsilon_z kE_z = 0, \ \mu_x\frac{\partial H_x}{\partial x} + \mu_y\frac{\partial H_y}{\partial y} + \mathrm{i}\mu_z kH_z = 0, \end{aligned}\right\} \tag{3.66}$$

where a monochromatic plane wave $\exp[-\mathrm{i}(\omega t - kz)]$ is assumed.

When the electromagnetic field is TE mode, namely $E_z = 0$, the following equation is obtained from Eq. (3.66) by eliminating E_x, E_y, H_x, and H_y:

$$\mu_x\frac{\mathrm{i}k}{\omega^2\varepsilon_y\mu_x - k^2}\frac{\partial^2 H_z}{\partial x^2} + \mu_y\frac{\mathrm{i}k}{\omega^2\varepsilon_x\mu_y - k^2}\frac{\partial^2 H_z}{\partial y^2} + \mathrm{i}\mu_z kH_z = 0. \tag{3.67}$$

One of the solutions of Eq. (3.67) is represented by

$$H_z = H_0\cos(\beta_x x)\cos(\beta_y y), \tag{3.68}$$

where H_0 is a constant. The other components of the electromagnetic fields can be calculated from Eqs. (3.66) and (3.68) and written as

$$H_x = -H_0 \frac{\mathrm{i}k}{\omega^2 \varepsilon_y \mu_x - k^2} \beta_x \sin(\beta_x x) \cos(\beta_y y), \tag{3.69}$$

$$H_y = -H_0 \frac{\mathrm{i}k}{\omega^2 \varepsilon_x \mu_y - k^2} \beta_y \cos(\beta_x x) \sin(\beta_y y), \tag{3.70}$$

$$E_x = -H_0 \frac{\mathrm{i}\omega\mu_y}{\omega^2 \varepsilon_x \mu_y - k^2} \beta_y \cos(\beta_x x) \sin(\beta_y y), \tag{3.71}$$

$$E_y = H_0 \frac{\mathrm{i}\omega\mu_x}{\omega^2 \varepsilon_y \mu_x - k^2} \beta_x \sin(\beta_x x) \cos(\beta_y y). \tag{3.72}$$

Substituting Eq. (3.68) into Eq. (3.67), we have

$$\beta_x^2 \frac{\mu_x}{\omega^2 \varepsilon_y \mu_x - k^2} + \beta_y^2 \frac{\mu_y}{\omega^2 \varepsilon_x \mu_y - k^2} = \mu_z. \tag{3.73}$$

Considering the boundary conditions:

$$E_x(y = 0, b) = 0, \tag{3.74}$$

$$E_y(x = 0, a) = 0, \tag{3.75}$$

the following equations are derived from Eqs. (3.71) and (3.72):

$$\beta_x = \frac{m\pi}{a}, \tag{3.76}$$

$$\beta_y = \frac{n\pi}{b}, \tag{3.77}$$

where m and n are non-negative integers. After substitution of Eqs. (3.76) and (3.77) into Eq. (3.73), the wavenumber is obtained. The wave impedance is determined from the ratio of the electric field to the magnetic field. The wavenumber $k_{\mathrm{TE}_{10}}$ and the wave impedance $Z_{\mathrm{TE}_{10}}$ for the TE_{10} mode ($m = 1, n = 0$) are given by

$$k_{\mathrm{TE}_{10}} = \frac{2\pi f}{c_0} \sqrt{\varepsilon_{\mathrm{r}y} \mu_{\mathrm{r}x} - \frac{\mu_{\mathrm{r}x}}{\mu_{\mathrm{r}z}} \left(\frac{c_0}{2af} \right)^2}, \tag{3.78}$$

$$Z_{\mathrm{TE}_{10}} = -\frac{E_y}{H_x} = \frac{2\pi f \mu_0 \mu_{\mathrm{r}x}}{k_{\mathrm{TE}_{10}}}, \tag{3.79}$$

respectively.

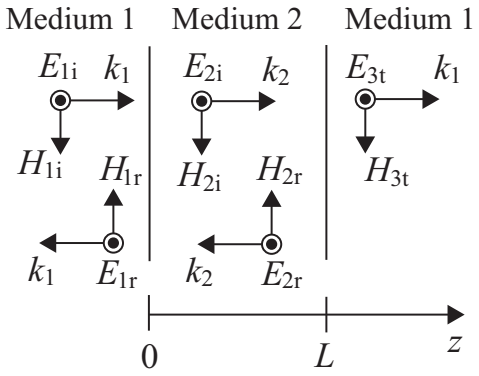

Figure 3.22: Three-layer structure.

S parameters Assume that an infinite slab of medium 2 (wavenumber k_2, wave impedance Z_2) is placed in medium 1 (wavenumber k_1, wave impedance Z_1) and that a monochromatic plane electromagnetic wave comes from the left as shown in Fig. 3.22. The incident, reflected, and transmitted electromagnetic waves are denoted by i, r, and t, respectively, in the figure.

We calculate S parameters of the system. The definitions of the S parameters, namely the reflection coefficient S_{11} and the transmission coefficient S_{21}, are as follows:

$$S_{11} = \frac{E_{1\mathrm{r}}}{E_{1\mathrm{i}}}, \tag{3.80}$$

$$S_{21} = \frac{E_{3\mathrm{t}}}{E_{1\mathrm{i}}}. \tag{3.81}$$

The electric fields in region 1, 2, and 3 are written as

$$E_1 = E_{1\mathrm{i}}\mathrm{e}^{\mathrm{i}k_1 z}\mathrm{e}^{-\mathrm{i}\omega t} + E_{1\mathrm{r}}\mathrm{e}^{-\mathrm{i}k_1 z}\mathrm{e}^{-\mathrm{i}\omega t}, \tag{3.82}$$

$$E_2 = E_{2\mathrm{i}}\mathrm{e}^{\mathrm{i}k_2 z}\mathrm{e}^{-\mathrm{i}\omega t} + E_{2\mathrm{r}}\mathrm{e}^{-\mathrm{i}k_2 z}\mathrm{e}^{-\mathrm{i}\omega t}, \tag{3.83}$$

$$E_3 = E_{3\mathrm{t}}\mathrm{e}^{\mathrm{i}k_1 z}\mathrm{e}^{-\mathrm{i}\omega t}, \tag{3.84}$$

respectively. The boundary conditions at $z = 0$ and $z = L$ are reduced to

$$E_{1\mathrm{i}} + E_{1\mathrm{r}} = E_{2\mathrm{i}} + E_{2\mathrm{r}}, \tag{3.85}$$

$$\frac{1}{Z_1}(E_{1\mathrm{i}} - E_{1\mathrm{r}}) = \frac{1}{Z_2}(E_{2\mathrm{i}} - E_{2\mathrm{r}}), \tag{3.86}$$

and

$$E_{2\mathrm{i}}\mathrm{e}^{\mathrm{i}k_2L} + E_{2\mathrm{r}}\mathrm{e}^{-\mathrm{i}k_2L} = E_{3\mathrm{t}}\mathrm{e}^{\mathrm{i}k_1L}, \tag{3.87}$$

$$\frac{1}{Z_2}(E_{2\mathrm{i}}\mathrm{e}^{\mathrm{i}k_2L} - E_{2\mathrm{r}}\mathrm{e}^{-\mathrm{i}k_2L}) = \frac{1}{Z_1}E_{3\mathrm{t}}\mathrm{e}^{\mathrm{i}k_1L}, \tag{3.88}$$

respectively. Here relations $Z_1 = E_{1\mathrm{i}}/H_{1\mathrm{i}} = E_{1\mathrm{r}}/H_{1\mathrm{r}} = E_{3\mathrm{t}}/H_{3\mathrm{t}}$ and $Z_2 = E_{2\mathrm{i}}/H_{2\mathrm{i}} = E_{2\mathrm{r}}/H_{2\mathrm{r}}$ are used. From Eqs. (3.85)-(3.88), the S parameters are calculated to be

$$S_{11} = \frac{-(Z_1^2 - Z_2^2)(\mathrm{e}^{\mathrm{i}k_2L} - \mathrm{e}^{-\mathrm{i}k_2L})}{(Z_1 - Z_2)^2\mathrm{e}^{\mathrm{i}k_2L} - (Z_1 + Z_2)^2\mathrm{e}^{-\mathrm{i}k_2L}}, \tag{3.89}$$

$$S_{21} = \frac{-4Z_1Z_2}{[(Z_1 - Z_2)^2\mathrm{e}^{\mathrm{i}k_2L} - (Z_1 + Z_2)^2\mathrm{e}^{-\mathrm{i}k_2L}]\mathrm{e}^{\mathrm{i}k_1L}}. \tag{3.90}$$

Determination of ε_r and μ_r The medium parameters of medium 1 (relative permittivity $\varepsilon_{\mathrm{r}1}$, relative permeability $\mu_{\mathrm{r}1}$) are assumed to be known values and that of medium 2 (relative permittivity $\varepsilon_{\mathrm{r}2}$, relative permeability $\mu_{\mathrm{r}2}$) are unknown values to be measured.

The values of $\varepsilon_{\mathrm{r}2}$ and $\mu_{\mathrm{r}2}$ can be determined from Eqs. (3.78), (3.79), (3.89), and (3.90) by measuring both the complex parameters S_{11} and S_{21} [52, 53]. This method enables us to examine medium parameters of unknown materials, however, the procedure of the measurement is a little bit complicated. It is necessary to measure the phases as well as the magnitudes of the reflected and transmitted waves.

When the expressions of the functions $\varepsilon_{\mathrm{r}2}(f)$ and $\mu_{\mathrm{r}2}(f)$ are known, $\varepsilon_{\mathrm{r}2}$ and $\mu_{\mathrm{r}2}$ can be estimated from a measurement of the frequency dependence of either $|S_{11}|$ or $|S_{21}|$. Based on the result of the FDTD simulation shown in Sec. 3.2.2, it is reasonable to make an assumption that $\varepsilon_{\mathrm{r}2}(f)$ and $\mu_{\mathrm{r}2}(f)$ are represented by the Lorentz functions,

$$\varepsilon_{\mathrm{r}2}(f) = 1 - \frac{F_\mathrm{e}}{f^2 - f_{0\mathrm{e}}^2 + \mathrm{i}\gamma_\mathrm{e}f}, \tag{3.91}$$

$$\mu_{\mathrm{r}2}(f) = 1 - \frac{F_\mathrm{m}}{f^2 - f_{0\mathrm{m}}^2 + \mathrm{i}\gamma_\mathrm{m}f}, \tag{3.92}$$

where $f_{0\mathrm{e}}$ ($f_{0\mathrm{m}}$) is the resonance frequency of the electric (magnetic) response, γ_e (γ_m) represents the loss in the electric (magnetic) response, and F_e and F_m are

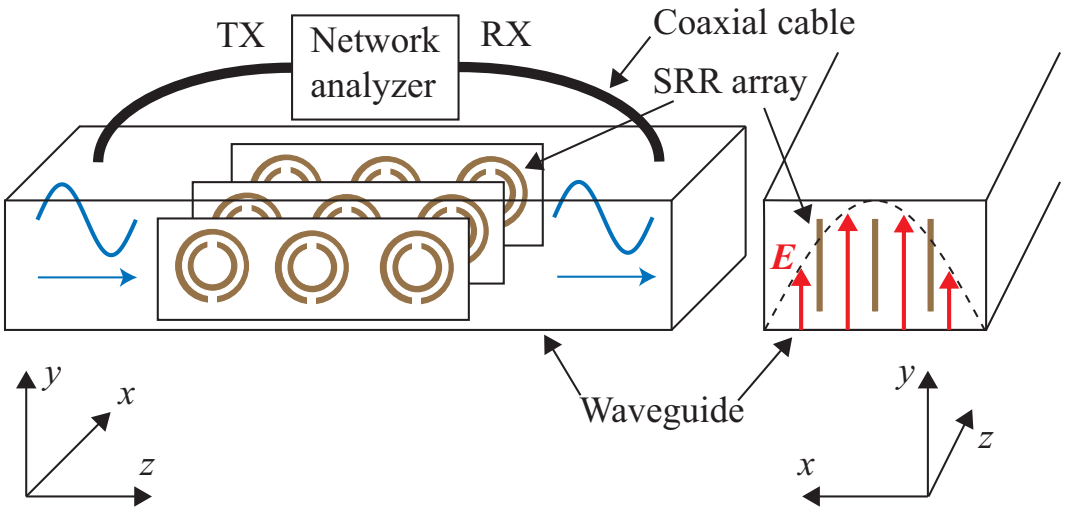

Figure 3.23: Schematic diagram of the transmission measurement system.

constants. Although the relative permittivity of the SRR array is found to be almost unity from the result of the FDTD simulation, we dare to assume that $\varepsilon_{\mathrm{r}2}(f)$ is represented by the Lorentz function. By substituting Eqs. (3.91) and (3.92) into Eq. (3.89) [Eq. (3.90)] and fitting $|S_{11}(f)|$ [$|S_{21}(f)|$] to the measured reflection (transmission) spectrum, $\varepsilon_{\mathrm{r}2}(f)$ and $\mu_{\mathrm{r}2}(f)$ can be evaluated. In this study, we determine $\varepsilon_{\mathrm{r}2}(f)$ and $\mu_{\mathrm{r}2}(f)$ from the transmission spectrum.

Measurement system

The schematic diagram of the measurement system is shown in Fig. 3.23. An SRR array was placed in a rectangular waveguide. The SRRs were arranged so that the SRR array responded only to the x-component of the magnetic field. Transmitting and receiving ports of a network analyzer were connected to the waveguide by coaxial cables (RG213/U). The detail of each component is described below.

Waveguide The dimension of the cross section of the rectangular waveguide was $(a, b) = (72.1\,\mathrm{mm}, 34.0\,\mathrm{mm})$ (see Fig. 3.21). The frequency range in which only the TE_{10} mode can propagate is from 2.08 GHz to 4.16 GHz. Coaxial-waveguide transformers were connected to the both ends of the waveguide.

Table 3.2: Geometrical parameters of the SRR arrays used in Sec. 3.2.4.

	r/mm	w/mm	d/mm	t/μm	L/cm	N
SRR array 1	4.85	0.8	0.9	35	17.0	$3 \times 2 \times 10$
SRR array 2	4.1	0.3	0.45	35	17.0	$3 \times 2 \times 13$
SRR array 3	4.0	0.61	0.48	35	5.25	$5 \times 2 \times 4$
SRR array 4	4.0	0.61	0.48	35	10.5	$5 \times 2 \times 8$

SRR array Four kinds of SRR arrays were fabricated by using printed circuit boards. The geometrical parameters of the fabricated SRR arrays are shown in Tab. 3.2. Here L is the length of the SRR array in the z-direction and N represents the numbers of SRRs in the x-, y-, and z-directions.

Network analyzer The same network analyzer as that used in Sec. 3.2.3 was used as the microwave generator and detector.

Method

First, through calibration (normalization) was carried out in order to eliminate errors in the measurement system [51]. A transmission characteristic of the empty waveguide was measured and the measured response was regarded as a reference value. Next, the SRR array was placed in the waveguide and the transmission response was measured. The transmissivity of the SRR array was determined by dividing the transmission response of the SRR array by that of the empty waveguide.

Experimental results

The transmission spectra of SRR arrays 1 and 2 are shown in Fig. 3.24 as green crosses. There exists a dip in the transmission spectrum in each case. This indicates that the resonances of the SRR array metamaterials are observed.

Figure 3.25 shows the transmission spectra of SRR arrays 3 and 4. The frequency where the dip in the transmission spectrum is observed in the case of SRR array 3 is

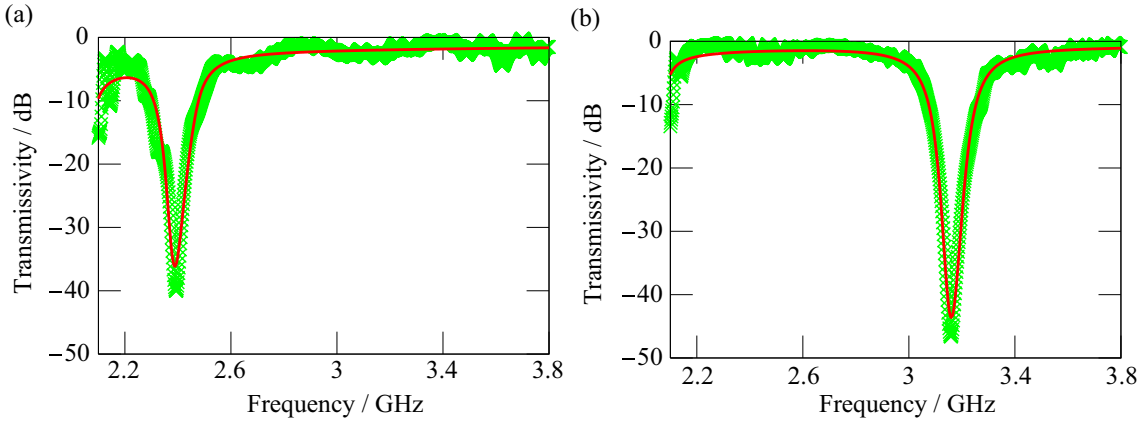

Figure 3.24: Transmission spectra of (a) SRR array 1 and (b) SRR array 2 (green crosses). Red lines are the fitted curves.

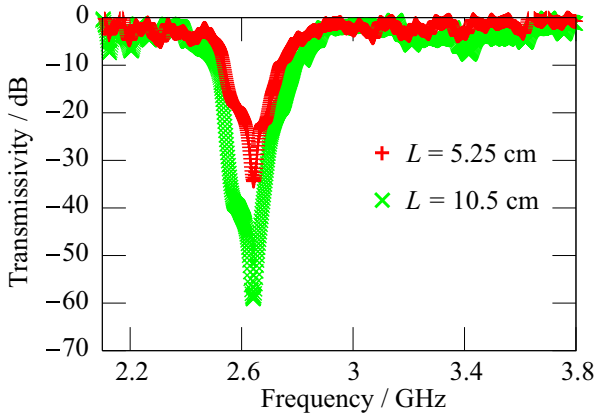

Figure 3.25: Transmission spectra of SRR array 3 ($L = 5.25\,\mathrm{cm}$) and SRR array 4 ($L = 10.5\,\mathrm{cm}$).

the same as that in the case of SRR array 4. This implies that the frequency where the dip is observed does not depend on the length of the SRR array metamaterial.

Discussion

We estimated the relative permittivity and permeability of the SRR array from the measured transmission spectrum. The values of k_1 and Z_1 were calculated by

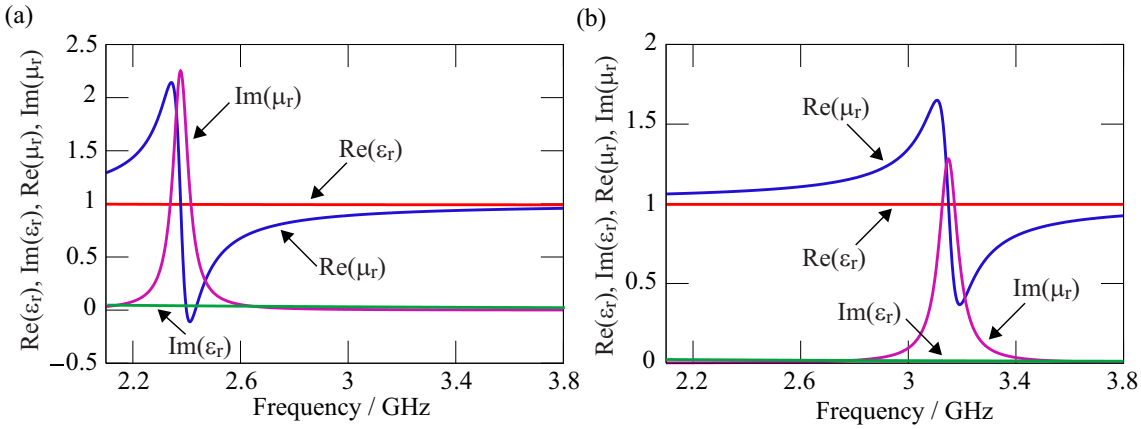

Figure 3.26: (a) Relative permittivity ε_{r} and relative permeability μ_{r} of SRR array 1 and (b) those of SRR array 2 versus frequency.

substituting $\varepsilon_{\mathrm{r}y} = 1$ and $\mu_{\mathrm{r}x} = \mu_{\mathrm{r}z} = 1$ into Eqs. (3.78) and (3.79). Both $\varepsilon_{\mathrm{r}y}(f)$ and $\mu_{\mathrm{r}x}(f)$ of the SRR array were assumed to be given by the Lorentz functions, Eqs. (3.91) and (3.92). Since the SRR array responded only to the x-component of the magnetic field, $\mu_{\mathrm{r}z}$ was set to unity. Substituting Eqs. (3.91), (3.92) and $\mu_{\mathrm{r}z} = 1$ into Eqs. (3.78) and (3.79), k_2 and Z_2 were obtained. The parameters $f_{0\mathrm{e}}$, $f_{0\mathrm{m}}$, γ_{e}, γ_{m}, F_{e}, and F_{m} were fixed by fitting the theoretical transmissivity $|S_{21}(f)|$ calculated from Eq. (3.90) to the measured transmission spectrum. The fitted transmission spectra of SRR arrays 1 and 2 are shown as the red curves in Fig. 3.24. The theoretical and measured transmissivities are in good agreement.

The relative permittivity and permeability of SRR array 1 obtained by the fitting are shown in Fig. 3.26(a). These values are written as

$$\varepsilon_{\mathrm{r}y}(f) \simeq 1, \tag{3.93}$$

$$\mu_{\mathrm{r}x}(f) = 1 - \frac{0.368\,(\mathrm{GHz})^2}{f^2 - (2.38\,\mathrm{GHz})^2 + \mathrm{i}(0.0687\,\mathrm{GHz})f}. \tag{3.94}$$

The relative permittivity of SRR array 1 is almost unity and the relative permeability is changed significantly from unity near the resonance frequency. The measured resonance frequency, 2.38 GHz, is 4.8 % larger than the calculated resonance frequency from Eq. (3.46), 2.27 GHz.

Figure 3.26(b) shows the obtained relative permittivity and permeability of SRR array 2. These medium parameters are described by

$$\varepsilon_{ry}(f) \simeq 1, \tag{3.95}$$

$$\mu_{rx}(f) = 1 - \frac{0.340\,(\mathrm{GHz})^2}{f^2 - (3.15\,\mathrm{GHz})^2 + \mathrm{i}(0.0843\,\mathrm{GHz})f}. \tag{3.96}$$

The relative permittivity is almost unity also in this case. The resonance frequency, 3.15 GHz, is 31.3 % larger than the calculated value, 2.27 GHz.

The estimated relative permittivity and relative permeability of each SRR array are consistent with the FDTD simulation in Sec. 3.2.2. This indicates that the FDTD simulation is reliable and that it is experimentally confirmed that Brewster's condition can be satisfied for TE waves in the SRR array metamaterial.

From the above results, the resonance frequency is found to be almost the same as the frequency where the transmittance becomes minimum value. Based on this fact, the resonance frequencies of SRR arrays 3 and 4 are determined to be 2.65 GHz, which is 2.3 % larger than the value calculated from Eq. (3.46), 2.59 GHz.

The measured and calculated resonance frequencies are in good agreement except for the case of SRR array 2. Only in the case of SRR array 2, the geometrical parameters of the SRR almost reach the lower limit of the condition where the error of the analytical approximation of the capacitance, Eq. (3.44), is small, namely $0.4 < 2w/d < 10$ [46]. In the other cases, the differences between the measured and calculated values are less than 5 %. Thus, the LC lumped circuit model is useful for the design of SRR array metamaterials as long as the approximation conditions are well satisfied.

3.3 Observation of magnetic Brewster's effect

The analysis in Sec. 3.2 demonstrated that Brewster's effect for TE waves could be easily observed just below the resonance frequency of the SRR array metamaterial. We now examine the reflectivity of the SRR array for various incident angles in order to make an experimental verification of TE Brewster's effect.

If the (pseudo-)Brewster angle[2] does not exist, the power reflectivity increases with the incident angle. However, if there exists the Brewster angle, the power reflectivity first decreases, and then increases with increasing the incident angle. The power reflectivity comes to minimum when the incident angle is equal to the Brewster angle. Thus, the Brewster angle can be found by measuring the incident angle dependence of the power reflectivity.

3.3.1 Measurement system

We built experimental setups shown in Figs. 3.27 and 3.28. The former setup was used to measure the transmittance for normal incidence of the SRR array. From the transmission spectrum, the resonance frequency of the SRR array can be determined. The latter one was used to measure the reflectance of the SRR array for various incident angles, or to examine whether TE Brewster's effect arises.

In these setups, two parallel aluminum plates formed a two-dimensional waveguide [54]. Transmitting and receiving horn antennas and the SRR array were placed in the waveguide. The horn antennas were connected to a network analyzer with coaxial cables. The detail of each component is given in the following.

Waveguide

The two-dimensional waveguide consisted of two parallel aluminum plates separated by 38.0 mm. The size of the aluminum plates was 1.0 m × 1.5 m and the thickness was 2.0 mm.

In this waveguide, the electric field is perpendicular to the plates, and the electromagnetic fields become uniform in the z-direction below 3.95 GHz, which is determined by the separation of the two aluminum plates. Thus, only TE waves can be propagated. Note that the direction of the electric field does not change for the change of the incident angle θ and fixed to the direction of the minimum electric response of the SRR array [55, 56].

[2] In this section, we refer to the pseudo-Brewster angle as the Brewster angle for simplicity.

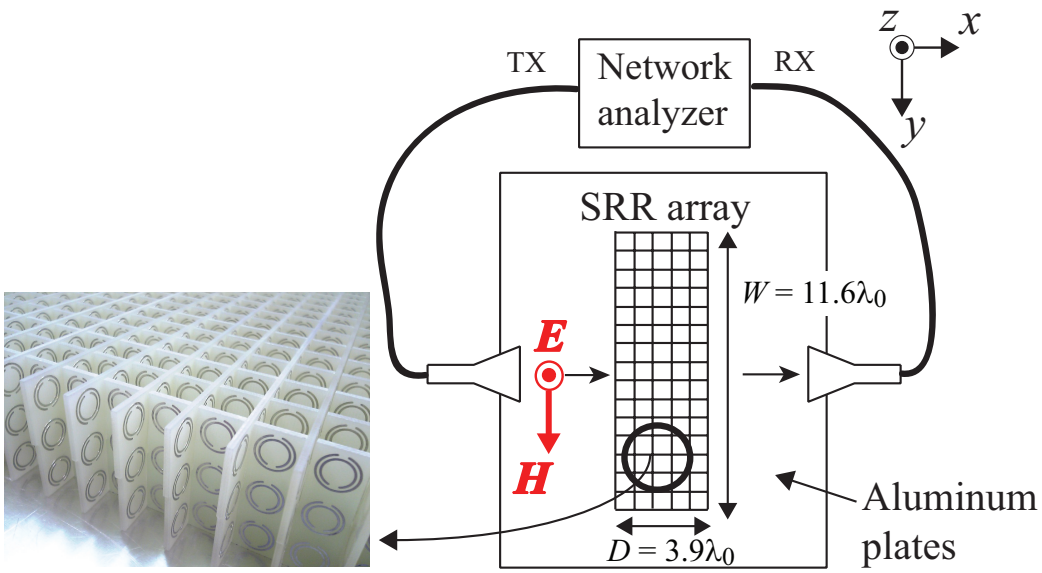

Figure 3.27: Schematic diagram of the transmission measurement system.

Horn antenna

A horn antenna was used in order to generate a slowly diverging beam. We put another horn antenna to receive the transmitted wave in the transmission measurement. In the reflection measurement, the receiving horn antenna was used to detect the plane wave reflected at the boundary between air and the SRR array. Only the plane waves propagating normal to the antenna apertures can be coupled to the horn antennas.

The horn antennas were made of brass plates whose thicknesses were 2.0 mm. The aperture size of the horn antennas was 15.0 cm × 3.4 cm. The boundary between the far field region (Fraunhofer region) and the near field region (Fresnel region) for the electromagnetic wave whose frequency is less than 3.8 GHz (the maximum operating frequency of the network analyzer) is at most 28.5 cm away from the aperture [57]. Therefore, we set the distance from the antennas to the interface between air and the SRR array to 38.4 cm.

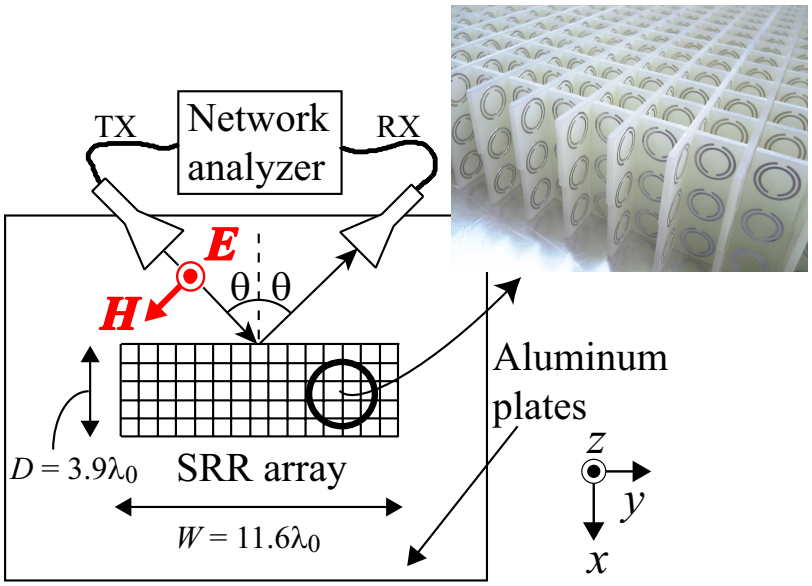

Figure 3.28: Schematic diagram of the reflection measurement system.

SRR

Similar to Sec. 3.2, SRRs were fabricated using printed circuit boards. The geometrical parameters of the SRR were $r = 4.0\,\mathrm{mm}$, $w = 0.61\,\mathrm{mm}$, $d = 0.48\,\mathrm{mm}$, and $t = 35\,\mu\mathrm{m}$, which were the same parameters as those of SRR arrays 3 and 4 in Sec. 3.2. The calculated resonance frequency from Eq. (3.46) is 2.59 GHz; this corresponds to the wavelength in a vacuum, $\lambda_0 = 11.6\,\mathrm{cm}$.

SRR array

The unit cell size of the SRR array must be much smaller than λ_0; therefore, the SRRs were arranged every $1.4\,\mathrm{cm}(= 0.12\lambda_0)$ in the x- and y-directions and $1.3\,\mathrm{cm}(= 0.11\lambda_0)$ in the z-direction. The direction of $\boldsymbol{H}$ varied in the xy-plane because the reflectance was measured for various incident angles. Hence, the SRRs were arranged orthogonally to make the response of the SRR array isotropic.

The dimension of the SRR array was $(W, D, H) = (135.0\,\mathrm{cm}, 45.0\,\mathrm{cm}, 3.8\,\mathrm{cm}) = (11.6\lambda_0, 3.9\lambda_0, 0.33\lambda_0)$ (see Figs. 3.27 and 3.28). The height H was determined by the separation of the two aluminum plates that form the two-dimensional waveguide.

The depth D was made sufficiently large so that the influence of the back side reflection can be avoided. The method to determine the width W is described in the following.

The width W should be set large enough in order to ensure an extended boundary. It is necessary to consider the first Fresnel zone in order to determine W quantitatively [58]. Let us suppose that T is a transmitting point and R is a receiving point in Fig. 3.29(a). When the sum of the distance TP and the distance PR equals the sum of the distance TR and a half of the wavelength λ, the set of the points P becomes spheroid with two focal points located at T and R. The first Fresnel zone is the inner region of the spheroid. In transmission measurements, the dimension of the cross section of the medium under test should be larger than that of the first Fresnel zone.

We consider the first Fresnel zone for reflection measurements. Figure 3.29(b) shows the first Fresnel zone, whose focal points are located at T$'$ and R, for the reflection measurement. The point T$'$ is the mirror image of T with respect to the reflection plane. The reflection surface of the medium should be larger than the cross section of the first Fresnel zone cut in the reflection plane. The first Fresnel zone shown in Fig. 3.29 is the inner region of the spheroid that is given by

$$r_1 + r_2 = \frac{\lambda}{2} + 2r. \tag{3.97}$$

The length of the major axis of the spheroid is written as

$$l_{\mathrm{major}} = \frac{\lambda}{2} + 2r. \tag{3.98}$$

The cross section of the first Fresnel zone cut in the reflection plane becomes largest when the incident angle is 90°. In this case, the length of the yellow line in Fig. 3.29 equals l_{major}. Thus, we should set W larger than l_{major}. (If the beam width of the electromagnetic wave is smaller than l_{major}, the condition $W > l_{\mathrm{major}}$ does not have to be satisfied.) When $r = 38.4\,\mathrm{cm}$ and $\lambda = 15\,\mathrm{cm}$, which corresponds to the wavelength of 2.0 GHz (lower limit of the operating frequency in our measurement system), l_{major} equals 84.3 cm. Therefore, W should be larger than 84.3 cm.

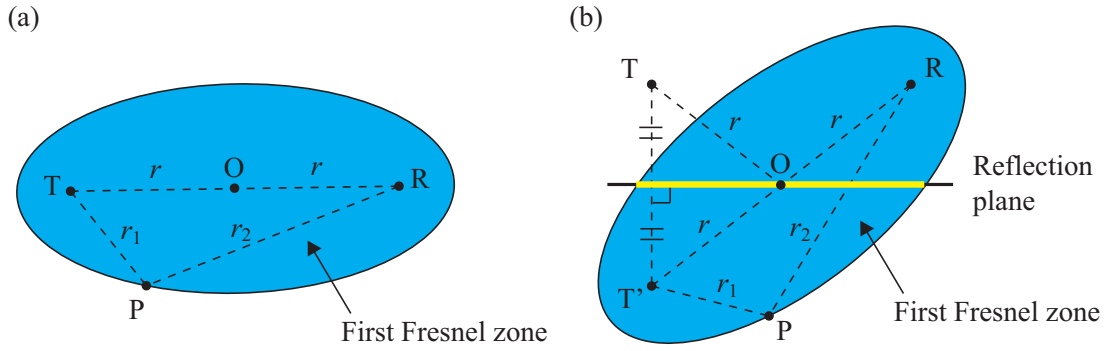

Figure 3.29: First Fresnel zones for (a) transmission and (b) reflection measurements. T is a transmitting point and R is a receiving point. P satisfies $r_1 + r_2 = (\lambda/2) + 2r$. The yellow line represents the cross section of the first Fresnel zone cut in the reflection plane.

Network analyzer

The same network analyzer as that used in Sec. 3.2 was used as the microwave generator and detector. The network analyzer supplied the signal to the transmitting horn antenna and detected the signal from the receiving horn antenna.

3.3.2 Method

Measurement of transmissivity for normal incidence

The two horn antennas were set opposite to each other. First, a transmission response of the empty space was measured and the measured response was regarded as complete transmission. Next, the SRR array was placed between the two antennas and a transmission response of the SRR array was measured. The transmissivity of the SRR array was calculated by dividing the transmission response of the SRR array by that of the empty space.

Measurement of reflectivity for various incident angles

The direction of the receiving horn antenna was always set such that a plane wave reflected with a reflection angle equal to the incident angle was detected. First,

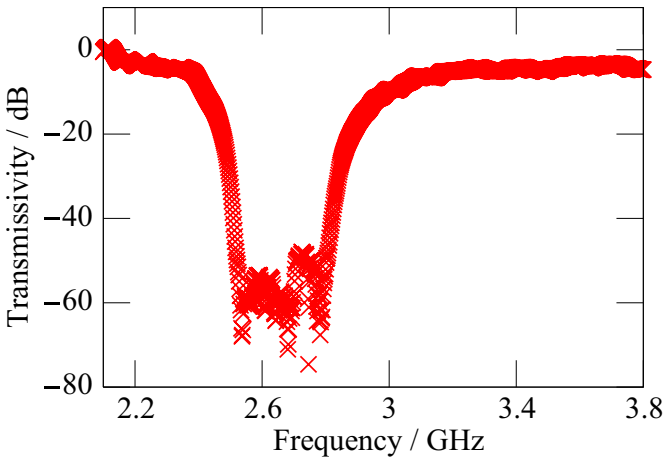

Figure 3.30: Transmission spectrum of the SRR array.

a reflection characteristic of a brass plate was measured and the measured response was regarded as perfect reflection. Then, a reflection response of the SRR array was measured. The reflectivity of the SRR array was determined by calculating the ratio of the reflection response of the SRR array to that of the brass plate.

3.3.3 Results

Transmission spectrum

The measured transmission spectrum of the SRR array is shown in Fig. 3.30. There is a depression in the transmission spectrum. This implies that the resonance of the SRR array is observed. The transmissivity is less than $-40\,\mathrm{dB}$ in the range from $2.50\,\mathrm{GHz}$ to $2.80\,\mathrm{GHz}$. We regard the resonance frequency as $2.65\,\mathrm{GHz}$ that is the center value between $2.50\,\mathrm{GHz}$ and $2.80\,\mathrm{GHz}$. The measured resonance frequency is the same as those of SRR arrays 3 and 4 in Sec. 3.2.

Dependence of reflectivity on incident angle

Figure 3.31 shows the measured reflectivities of the SRR array as a function of the incident angle θ for two distinct frequencies: $2.5845\,\mathrm{GHz}$ and $2.6001\,\mathrm{GHz}$.

In the case of $f = 2.5845\,\mathrm{GHz}$ shown in Fig. 3.31(a), the reflectivity decreases

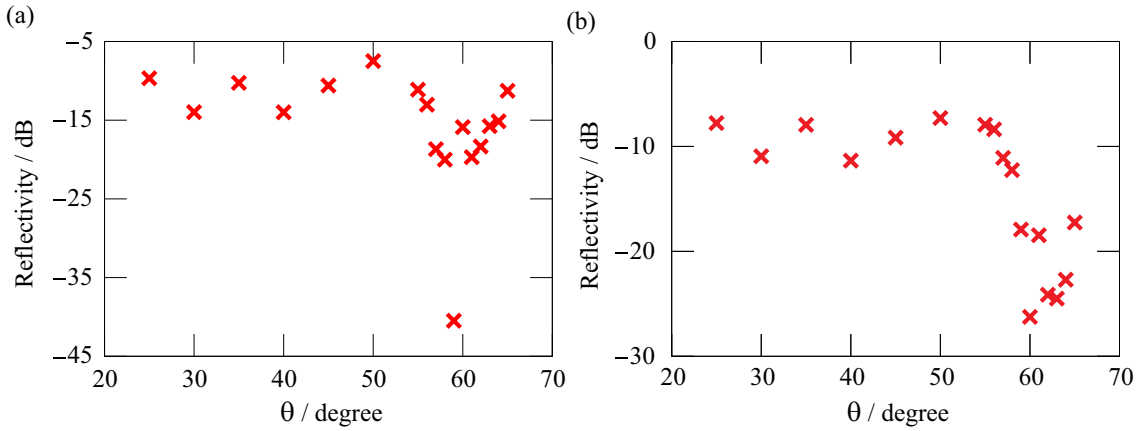

Figure 3.31: Reflectivities of the SRR array versus the incident angle θ in the cases of (a) $f = 2.5845\,\mathrm{GHz}$ and (b) $f = 2.6001\,\mathrm{GHz}$.

by more than 40 dB compared with the case of perfect reflection in the vicinity of $\theta = 59°$. This indicates that Brewster's effect for TE waves is observed. The incident angle $\theta = 59°$ where the minimum reflectivity is achieved corresponds to the Brewster angle.

In the case of $f = 2.6001\,\mathrm{GHz}$ shown in Fig. 3.31(b), the reflectivity decreases by more than 27 dB in the vicinity of $\theta = 60°$, which corresponds to the Brewster angle for TE waves. Compared with the case of $f = 2.5845\,\mathrm{GHz}$, the reflectivity gently decreases in the vicinity of the Brewster angle. This is because the loss of the SRR array comes to maximum at the resonance frequency $f = 2.65\,\mathrm{GHz}$, or the loss of the SRR array at $f = 2.6001\,\mathrm{GHz}$ is larger than that of $f = 2.5845\,\mathrm{GHz}$.

Brewster angle

The measured Brewster angles as a function of the frequency are plotted as red circles in Fig. 3.32. Note that the Brewster angles could be determined only in a limited region just below the resonance frequency. The frequency bandwidth where the Brewster angles could be observed is about 100 MHz, which corresponds to the fractional bandwidth of 4.2 %. The measured Brewster angles increase with the frequency in this region.

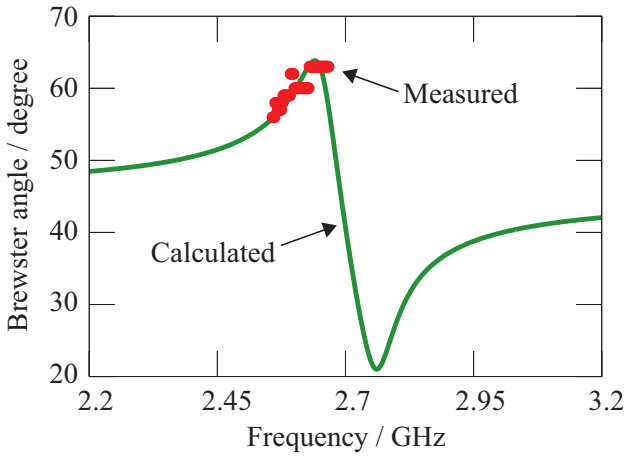

Figure 3.32: Measured (red circles) and calculated (green curve) Brewster angles versus frequency.

3.3.4 Discussion

In order to confirm the reliability of the experiments, we calculated the frequency dependence of the Brewster angles for TE waves from Eq. (3.19) by assuming

$$\varepsilon_{\mathrm{r}}(f) = 1, \tag{3.99}$$

$$\mu_{\mathrm{r}}(f) = 1 - \frac{F}{f^2 + \mathrm{i}\gamma f - f_0^2}, \tag{3.100}$$

where $f_0 = 2.65\,\mathrm{GHz}$ is the resonance frequency that is determined by the transmission measurement, and F and γ are the fitting parameters. The validity of this assumption is guaranteed by the results of Sec. 3.2. By fitting the calculated Brewster angles to the experimental results, we fixed the parameters F and γ. The calculated angles are shown as the green curve in Fig. 3.32. It increases with frequency in the region where the Brewster angles can be determined; this is in agreement with the experimental results. The agreement indicates that the measurements we performed are reliable. The fitting parameters, F and γ, are $0.6\,(\mathrm{GHz})^2$ and $0.052\,\mathrm{GHz}$, respectively. In Fig. 3.33, we plot $\mu_{\mathrm{r}}(f)$ in Eq. (3.100) using the obtained fitting parameters.

As previously discussed in Sec. 3.2, the Brewster angles can be observed only in a limited frequency region. We note that in actual experiments, the reflectivity varies

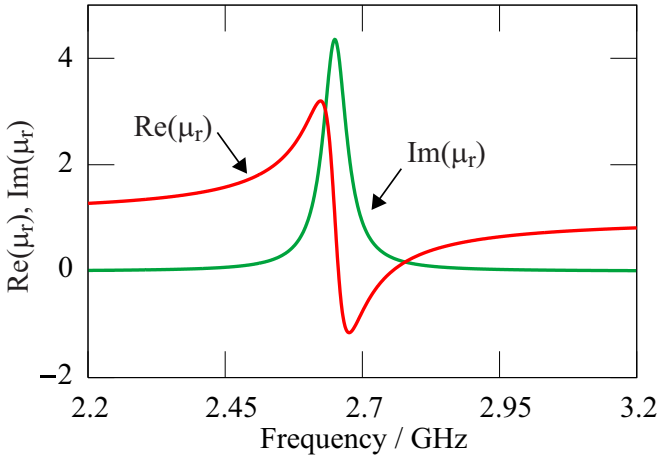

Figure 3.33: Relative permeability μ_r of the SRR array, which is obtained by the fitting, as a function of frequency.

somewhat erratically due to the interference of spurious waves or other reasons, and the dip in reflectivity can be detected only for the cases where R_{min}/R_0 is sufficiently small. In the other on-resonance frequency regions, R_{min} cannot be sufficiently small due to the absorption losses. On the other hand, R_0 reduces in the off-resonance regions. We could observe Brewster's effect in broader frequency regions if we use antennas that have better directivity than horn antenna, such as lens antenna [43].

3.4 Summary

We observed Brewster's no-reflection effect for TE waves, which had previously never been observed for normal dielectric media. It was found that a medium having $\mu_r \neq 1$ is necessary for observing TE Brewster's effect. A metamaterial composed of SRRs was used in order to achieve a magnetic medium at the microwave frequencies. The FDTD simulation showed that the TE Brewster effect could be easily observed in the narrow frequency region just below the resonance frequency of the SRR array. The reliability of the simulation was confirmed by experimentally investigating the properties of the single SRR and the SRR array. We measured the incident angle dependence of the reflectivity at the boundary between air and the SRR array and

were successful in observing Brewster's effect for TE waves.

This is a good example of the use of metamaterials. In terms of the parameter space $(\varepsilon_{\mathrm{r}}, \mu_{\mathrm{r}})$, by introducing metamaterials, the rigid condition of $\varepsilon_{\mathrm{r}} > 0$, $\mu_{\mathrm{r}} = 1$ can be eliminated. The restrictions $\varepsilon_{\mathrm{r}} > 0$ and $\mu_{\mathrm{r}} > 0$ can also be eliminated.

The working range of metamaterials presently extends from the microwave to the terahertz or even to the optical regions. In the near future, we may be able to fabricate a Brewster window for TE light. In fact, the TE Brewster effect for visible light has been observed [59] after our work.

Chapter 4

No-reflection conditions for chiral metamaterials

In the previous chapter, we described that Brewster's effect is observed for TE waves as well as TM waves when we control both permittivity and permeability. In addition to the permittivity and permeability, chirality parameter and non-reciprocity parameter can be controlled using metamaterials. It is also possible to control the anisotropy in electromagnetic responses. Therefore, the no-reflection condition for generalized media should be explored in order to develop novel devices for reflection control of electromagnetic waves. Brewster's condition has been studied for anisotropic media [29–32], chiral media (bi-isotropic media) [33, 34], and bi-anisotropic media [35]. However, thus far, the explicit relation among the medium parameters for achieving non-reflectivity in chiral and bi-anisotropic media have not been determined. The purpose of this study is to derive the explicit relation among the permittivity, permeability, and chirality parameter of the chiral medium that satisfy the no-reflection condition for a planar interface between a vacuum and the chiral medium.

The no-reflection condition is derived from the vanishing eigenvalue condition of the reflection Jones matrix. The analysis can be largely simplified by decomposing the reflection Jones matrix into the unit and Pauli matrices [60].

We find that in general chiral media, the no-reflection condition is satisfied by elliptically polarized (EP) incident waves for at most one particular angle of incidence.

This is merely a natural extension of the usual Brewster effect for achiral (nonchiral) media. When the wave impedance and the absolute value of the wavenumber in the chiral medium equal those in vacuum for one of the CP waves, the corresponding CP wave is transmitted to the medium without reflection for all angles of incidence. This phenomenon is quite different from the no-reflection effects for linearly polarized waves in achiral media and for elliptically polarized waves in chiral media. The no-reflection effect for chiral nihility media resembles that for achiral media.

We provide an FDTD analysis of the no-reflection effect for CP waves. We analyze the scatterings of electromagnetic waves by a cylinder and a triangular prism made of a chiral medium whose medium parameters satisfy the no-reflection condition for one of the CP waves. The simulation demonstrates that the corresponding CP wave is not scattered and the other CP wave is largely scattered. We show that a circular polarizing beam splitter can be achieved by utilizing the no-reflection effect.

We propose a structure of an isotropic chiral metamaterial in which the no-reflection effects for EP and CP waves could be observed. The metamaterial is composed of three-dimensionally arranged metal helices. We consider structural conditions that are required to be satisfied in the metamaterial having isotropy and chirality.

4.1 Reflection and transmission for chiral media

We derive the reflectivity and transmissivity at the boundary between a vacuum and an isotropic chiral medium [33]. The constitutive equations for chiral media are shown in Eqs. (2.31) and (2.32). The wavenumber and wave impedance in chiral media are given by Eqs. (2.42) and (2.39).

As shown in Fig. 4.1, suppose that a monochromatic plane electromagnetic wave is incident from the vacuum on the chiral medium at an incident angle of θ. The electromagnetic fields of the incident (i), reflected (r), and transmitted (t) waves

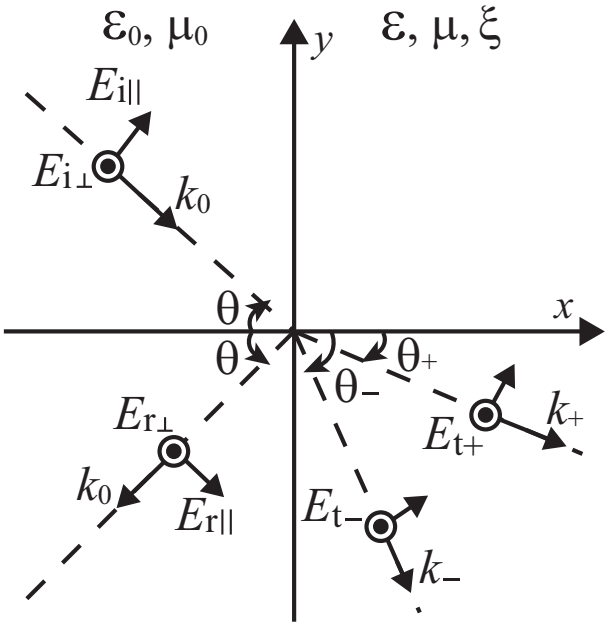

Figure 4.1: Geometry of coordinate system. Incident, reflected, and transmitted waves are denoted by subscripts i, r, and t. Region $x < 0$ represents a vacuum, and region $x \geq 0$ represents the chiral medium.

are written as the following equations:

$$\boldsymbol{E}_{\mathrm{i}} = \boldsymbol{E}_1 \exp\left[\mathrm{i}k_0(x\cos\theta - y\sin\theta)\right], \tag{4.1}$$

$$\boldsymbol{H}_{\mathrm{i}} = \boldsymbol{H}_1 \exp\left[\mathrm{i}k_0(x\cos\theta - y\sin\theta)\right], \tag{4.2}$$

$$\boldsymbol{E}_{\mathrm{r}} = \boldsymbol{E}_2 \exp\left[\mathrm{i}k_0(-x\cos\theta - y\sin\theta)\right], \tag{4.3}$$

$$\boldsymbol{H}_{\mathrm{r}} = \boldsymbol{H}_2 \exp\left[\mathrm{i}k_0(-x\cos\theta - y\sin\theta)\right], \tag{4.4}$$

$$\boldsymbol{E}_{\mathrm{t}} = \boldsymbol{E}_3 \exp\left[\mathrm{i}k_+(x\cos\theta_+ - y\sin\theta_+)\right] + \boldsymbol{E}_4 \exp\left[\mathrm{i}k_-(x\cos\theta_- - y\sin\theta_-)\right], \tag{4.5}$$

$$\boldsymbol{H}_{\mathrm{t}} = \boldsymbol{H}_3 \exp\left[\mathrm{i}k_+(x\cos\theta_+ - y\sin\theta_+)\right] + \boldsymbol{H}_4 \exp\left[\mathrm{i}k_-(x\cos\theta_- - y\sin\theta_-)\right], \tag{4.6}$$

where the common time-harmonic factor $\exp(-\mathrm{i}\omega t)$ is omitted for simplicity and

$$\boldsymbol{E}_1 = E_{\mathrm{i}\perp}\boldsymbol{e}_z + E_{\mathrm{i}\parallel}(\cos\theta\boldsymbol{e}_y + \sin\theta\boldsymbol{e}_x), \tag{4.7}$$

$$\boldsymbol{H}_1 = Z_0^{-1}[E_{\mathrm{i}\parallel}\boldsymbol{e}_z - E_{\mathrm{i}\perp}(\cos\theta\boldsymbol{e}_y + \sin\theta\boldsymbol{e}_x)], \tag{4.8}$$

$$\boldsymbol{E}_2 = E_{\mathrm{r}\perp}\boldsymbol{e}_z + E_{\mathrm{r}\parallel}(-\cos\theta\boldsymbol{e}_y + \sin\theta\boldsymbol{e}_x), \tag{4.9}$$

$$\boldsymbol{H}_2 = Z_0^{-1}[E_{\mathrm{r}\parallel}\boldsymbol{e}_z + E_{\mathrm{r}\perp}(\cos\theta\boldsymbol{e}_y - \sin\theta\boldsymbol{e}_x)], \tag{4.10}$$

$$\boldsymbol{E}_3 = E_{\mathrm{t}+}[\mathrm{i}(\cos\theta_+\boldsymbol{e}_y + \sin\theta_+\boldsymbol{e}_x) + \boldsymbol{e}_z], \tag{4.11}$$

$$\boldsymbol{H}_3 = E_{\mathrm{t}+}Z_{\mathrm{c}}^{-1}[-(\cos\theta_+\boldsymbol{e}_y + \sin\theta_+\boldsymbol{e}_x) + \mathrm{i}\boldsymbol{e}_z], \tag{4.12}$$

$$\boldsymbol{E}_4 = E_{\mathrm{t}-}[-\mathrm{i}(\cos\theta_-\boldsymbol{e}_y + \sin\theta_-\boldsymbol{e}_x) + \boldsymbol{e}_z], \tag{4.13}$$

$$\boldsymbol{H}_4 = E_{\mathrm{t}-}Z_{\mathrm{c}}^{-1}[-(\cos\theta_-\boldsymbol{e}_y + \sin\theta_-\boldsymbol{e}_x) - \mathrm{i}\boldsymbol{e}_z]. \tag{4.14}$$

Due to the translational invariance of the interface, Snell's equations:

$$k_0\sin\theta = k_+\sin\theta_+ = k_-\sin\theta_-, \tag{4.15}$$

are satisfied. From the continuity of the tangential components of the electromagnetic fields across the boundary, we obtain

$$E_{\mathrm{i}\perp} + E_{\mathrm{r}\perp} = E_{\mathrm{t}+} + E_{\mathrm{t}-}, \tag{4.16}$$

$$E_{\mathrm{i}\parallel}\cos\theta - E_{\mathrm{r}\parallel}\cos\theta = \mathrm{i}E_{\mathrm{t}+}\cos\theta_+ - \mathrm{i}E_{\mathrm{t}-}\cos\theta_-, \tag{4.17}$$

$$Z_0^{-1}(E_{\mathrm{i}\parallel} + E_{\mathrm{r}\parallel}) = \mathrm{i}Z_{\mathrm{c}}^{-1}(E_{\mathrm{t}+} - E_{\mathrm{t}-}), \tag{4.18}$$

$$Z_0^{-1}(-E_{\mathrm{i}\perp}\cos\theta + E_{\mathrm{r}\perp}\cos\theta) = -Z_{\mathrm{c}}^{-1}(E_{\mathrm{t}+}\cos\theta_+ + E_{\mathrm{t}-}\cos\theta_-). \tag{4.19}$$

The reflection and transmission matrices are derived from Eqs. (4.16)-(4.19) and written as

$$\begin{bmatrix} E_{\mathrm{r}\perp} \\ E_{\mathrm{r}\parallel} \end{bmatrix} = \begin{bmatrix} R_{11} & R_{12} \\ R_{21} & R_{22} \end{bmatrix} \begin{bmatrix} E_{\mathrm{i}\perp} \\ E_{\mathrm{i}\parallel} \end{bmatrix}, \tag{4.20}$$

$$\begin{bmatrix} E_{\mathrm{t}+} \\ E_{\mathrm{t}-} \end{bmatrix} = \begin{bmatrix} T_{++} & T_{+-} \\ T_{-+} & T_{--} \end{bmatrix} \begin{bmatrix} E_{\mathrm{i}+} \\ E_{\mathrm{i}-} \end{bmatrix}, \tag{4.21}$$

where

$$R_{11} = \frac{(Z_{\mathrm{c}}^2 - Z_0^2)\cos\theta(\cos\theta_+ + \cos\theta_-) + 2Z_0Z_{\mathrm{c}}(\cos^2\theta - \cos\theta_+\cos\theta_-)}{\Delta}, \tag{4.22}$$

$$R_{12} = \frac{\mathrm{i}2Z_0Z_{\mathrm{c}}\cos\theta(\cos\theta_+ - \cos\theta_-)}{\Delta}, \tag{4.23}$$

$$R_{21} = \frac{-\mathrm{i}2Z_0Z_{\mathrm{c}}\cos\theta(\cos\theta_+ - \cos\theta_-)}{\Delta}, \tag{4.24}$$

$$R_{22} = \frac{-(Z_{\mathrm{c}}^2 - Z_0^2)\cos\theta(\cos\theta_+ + \cos\theta_-) + 2Z_0Z_{\mathrm{c}}(\cos^2\theta - \cos\theta_+\cos\theta_-)}{\Delta}, \tag{4.25}$$

$$T_{++} = \frac{2Z_{\mathrm{c}}(Z_{\mathrm{c}} + Z_0)\cos\theta(\cos\theta + \cos\theta_-)}{\Delta}, \tag{4.26}$$

$$T_{+-} = \frac{-2Z_{\mathrm{c}}(Z_{\mathrm{c}} - Z_0)\cos\theta(\cos\theta - \cos\theta_-)}{\Delta}, \tag{4.27}$$

$$T_{-+} = \frac{-2Z_{\mathrm{c}}(Z_{\mathrm{c}} - Z_0)\cos\theta(\cos\theta - \cos\theta_+)}{\Delta}, \tag{4.28}$$

$$T_{--} = \frac{2Z_{\mathrm{c}}(Z_{\mathrm{c}} + Z_0)\cos\theta(\cos\theta + \cos\theta_+)}{\Delta}, \tag{4.29}$$

$$\Delta = (Z_{\mathrm{c}}^2 + Z_0^2)\cos\theta(\cos\theta_+ + \cos\theta_-) + 2Z_0Z_{\mathrm{c}}(\cos^2\theta + \cos\theta_+\cos\theta_-), \tag{4.30}$$

$$E_{\mathrm{i}\pm} = \frac{E_{\mathrm{i}\perp} \mp \mathrm{i}E_{\mathrm{i}\parallel}}{2}. \tag{4.31}$$

4.2 Derivation of no-reflection condition for chiral media

We find from the result of the previous section that the relation between the electric field of the incident wave and that of the reflected wave is written as

$$\begin{bmatrix} E_{\mathrm{r}\perp} \\ E_{\mathrm{r}\parallel} \end{bmatrix} = \frac{1}{\Delta} M_{\mathrm{R}} \begin{bmatrix} E_{\mathrm{i}\perp} \\ E_{\mathrm{i}\parallel} \end{bmatrix}, \tag{4.32}$$

$$M_{\mathrm{R}} = c_{\mathrm{u}} I + c_2\sigma_2 + c_3\sigma_3, \tag{4.33}$$

$$c_{\mathrm{u}} = 2Z_0Z_{\mathrm{c}}(\cos^2\theta - \cos\theta_+\cos\theta_-), \tag{4.34}$$

$$c_2 = -2Z_0Z_{\mathrm{c}}\cos\theta(\cos\theta_+ - \cos\theta_-), \tag{4.35}$$

$$c_3 = (Z_{\mathrm{c}}^2 - Z_0^2)\cos\theta(\cos\theta_+ + \cos\theta_-), \tag{4.36}$$

where we introduce the unit matrix I and the Pauli matrices [61]:

$$\sigma_2 = \begin{bmatrix} 0 & -\mathrm{i} \\ \mathrm{i} & 0 \end{bmatrix}, \quad \sigma_3 = \begin{bmatrix} 1 & 0 \\ 0 & -1 \end{bmatrix}. \tag{4.37}$$

The reflection matrix M_R can be rewritten as

$$M_\mathrm{R} = c_\mathrm{u} I + c_\varphi \sigma_\varphi, \tag{4.38}$$

where $c_\varphi = \sqrt{c_2^2 + c_3^2}$, $\sigma_\varphi = \sigma_2 \sin\varphi + \sigma_3 \cos\varphi$, $\sin\varphi = c_2/c_\varphi$, and $\cos\varphi = c_3/c_\varphi$.

The no-reflection condition is satisfied when M_R has at least one vanishing eigenvalue, namely, $\det(M_\mathrm{R}) = 0$ or $\mathrm{rank}(M_\mathrm{R}) \leq 1$. For the incident wave with the corresponding eigenpolarization, the reflection is nullified. From Eq. (4.38), we observe that the eigenvalue problem for M_R is reduced to that for σ_φ. The eigenvalues of σ_φ are ± 1 and their corresponding eigenpolarizations are $\boldsymbol{e}_{\varphi+} = \cos(\varphi/2)\,\boldsymbol{e}_z + \mathrm{i}\sin(\varphi/2)(\boldsymbol{e}_x \sin\theta + \boldsymbol{e}_y \cos\theta)$ and $\boldsymbol{e}_{\varphi-} = \sin(\varphi/2)\,\boldsymbol{e}_z - \mathrm{i}\cos(\varphi/2)(\boldsymbol{e}_x \sin\theta + \boldsymbol{e}_y \cos\theta)$. Therefore, M_R has one vanishing eigenvalue when $c_\mathrm{u} = c_\varphi \neq 0$ ($c_\mathrm{u} = -c_\varphi \neq 0$) is satisfied, and no-reflection is achieved for the incident wave with the polarization $\boldsymbol{e}_{\varphi-}$ ($\boldsymbol{e}_{\varphi+}$). When $c_\mathrm{u} = c_\varphi = 0$, M_R becomes zero matrix; no-reflection is achieved for arbitrary polarized incident waves.

4.3 Analysis of no-reflection effect for chiral media

We classify the no-reflection effects into three cases based on the expression of the reflection matrix and make detailed analyses of the phenomena.

4.3.1 No-reflection effect for elliptically polarized waves

Conditions $\xi \neq 0$, $k_+ \neq -k_-$, and $Z_\mathrm{c} \neq Z_0$ give $\varphi \neq n\pi/2$ with integer n. The eigenpolarizations are $\boldsymbol{e}_{\varphi\pm}$; hence, the no-reflection condition can only be satisfied for EP waves. The no-reflection effect is observed at a particular incident angle satisfying $c_\mathrm{u} = \pm c_\varphi$, which is a natural extension of the usually observed

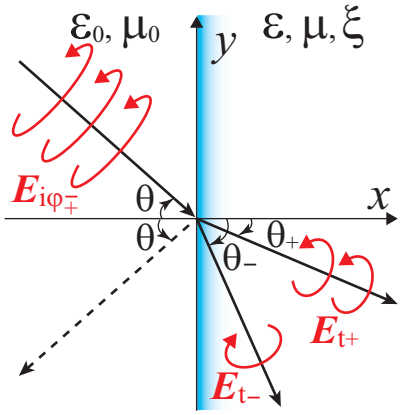

Figure 4.2: No-reflection effect for EP waves. The incident angle satisfies $c_{\mathrm{u}} = \pm c_{\varphi}$.

no-reflection effect, or the Brewster effect in achiral media ($\xi = 0$). In Fig. 4.2, we show a schematic of the no-reflection effect for EP waves.

The no-reflection angles are derived from the zero eigenvalue condition $c_{\mathrm{u}} = \pm c_{\varphi}$. The contour lines of the no-reflection angles are shown in the left panels of Fig. 4.3. The no-reflection condition in the case of $\xi = 0$ exists in the whole region of the first and third quadrants of the $(\varepsilon_{\mathrm{r}}, \mu_{\mathrm{r}})$-plane except $\varepsilon_{\mathrm{r}} = \mu_{\mathrm{r}}^{-1} \neq \pm 1$, as shown in Fig. 3.2, while in the case of $\xi \neq 0$, there is a region where the no-reflection condition does not exist, which is represented as the gray region in Fig. 4.3. In addition, the no-reflection condition also exists in the second and fourth quadrants, which correspond to strong chiral media ($k_+ k_- < 0$). The right panels of Fig. 4.3 show the incident polarization for which the no-reflection condition is satisfied. The polarization is described in terms of the ellipticity $\alpha = \arctan\left(E_{\parallel}/\mathrm{i}E_{\perp}\right)$. The condition $\alpha > 0$ ($\alpha < 0$) denotes left (right) elliptically polarized wave and $|\alpha| = 90°$ ($|\alpha| = 0$) corresponds to TM (TE) waves. When $|\alpha| > 45°$ ($|\alpha| < 45°$), major axis of the polarization ellipse is perpendicular (parallel) to $\boldsymbol{e}_z$ and minor axis is parallel (perpendicular) to $\boldsymbol{e}_z$, namely, the no-reflection condition is satisfied for TM-like (TE-like) EP waves.

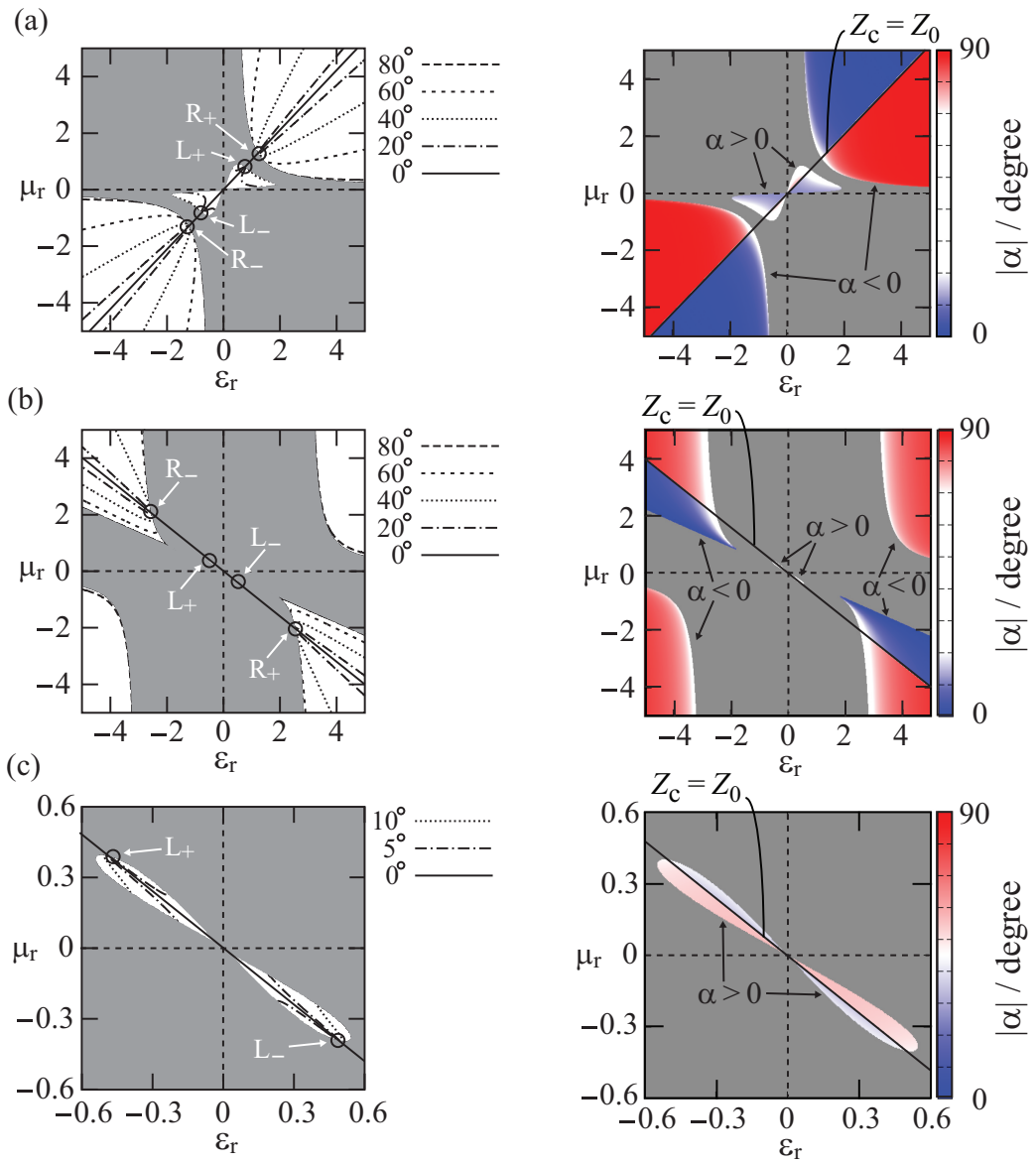

Figure 4.3: No-reflection conditions (a) for $\xi_r = \xi Z_0 = 0.2$ and (b), (c) for $\xi_r = 1.5$. [Note that the scale of (c) is different from other figures.] (left panels); contour lines of no-reflection angles. L_+ and R_+ (L_- and R_-) represent the no-reflection conditions for LCP and RCP waves written in Eq. (4.39) [Eq. (4.40)], respectively. (right panels); ellipticity α of incident polarization for which no-reflection condition is satisfied. Sign of α is reversed if sign of ξ_r is reversed. No-reflection conditions do not exist in gray region.

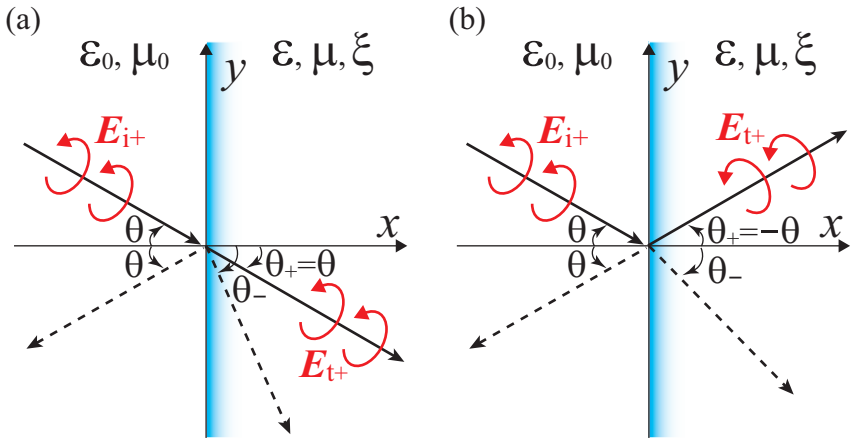

Figure 4.4: No-reflection effects for CP waves in the cases of (a) $k_+ = k_0$ and (b) $k_+ = -k_0$. Non-reflectivity is achieved for any incident angle.

4.3.2 No-reflection effect for circularly polarized waves

In the case of $\xi \neq 0$, $k_+ \neq -k_-$, and $Z_\mathrm{c} = Z_0$, we have $M_\mathrm{R} = c_\mathrm{u} I + c_2 \sigma_2$. The eigenpolarizations are $[\boldsymbol{e}_z \pm \mathrm{i}(\boldsymbol{e}_x \sin\theta + \boldsymbol{e}_y \cos\theta)]/\sqrt{2}$; hence, the no-reflection condition can only be satisfied for CP waves. The condition $\cos\theta_+ = \cos\theta$ ($\cos\theta_- = \cos\theta$) is required to satisfy $c_\mathrm{u} = -c_2$ ($c_\mathrm{u} = c_2$), which is the no-reflection condition for LCP (RCP) waves. Note that once $|k_+| = k_0$ ($|k_-| = k_0$) is satisfied by selecting the constants of medium, $c_\mathrm{u} = -c_2$ ($c_\mathrm{u} = c_2$) is satisfied for any incident angle. That is, the no-reflection condition is satisfied for all angles of incidence. This observation is quite different from the no-reflection conditions for TM and TE waves in isotropic achiral media and for EP waves in isotropic chiral media. A qualitatively new mode of no-reflection is obtained for LCP (RCP) waves in isotropic chiral media when the wave impedance matching condition $Z_\mathrm{c} = Z_0$ and the wavenumber matching condition $|k_+| = k_0$ ($|k_-| = k_0$) are satisfied simultaneously. Figure 4.4 shows a schematic of the no-reflection effect for CP waves.

We derive the explicit relations among the medium parameters for the no-reflection condition for CP waves. From the above discussion, both $Z_\mathrm{c} = Z_0$ and

$|k_+| = k_0$ ($|k_-| = k_0$) are necessary and yield the following relations:

$$\varepsilon_\mathrm{r} = -(\pm\xi_\mathrm{r} - 1), \quad \mu_\mathrm{r} = \frac{\pm 1}{\xi_\mathrm{r} \pm 1} \quad (\text{from } k_\pm = k_0), \tag{4.39}$$

$$\varepsilon_\mathrm{r} = \pm\xi_\mathrm{r} - 1, \quad \mu_\mathrm{r} = -\frac{\pm 1}{\xi_\mathrm{r} \pm 1} \quad (\text{from } k_\pm = -k_0), \tag{4.40}$$

where $\xi_\mathrm{r} = \xi Z_0$ is the normalized chirality parameter. The positive (negative) sign in Eqs. (4.39) and (4.40) indicates the condition for LCP (RCP) waves. Figure 4.5(a) and 4.5(b) [4.5(c) and 4.5(d)] represent the relations among ε_r, μ_r, and ξ_r shown in Eq. (4.39) [Eq. (4.40)]. Note that the no-reflection conditions for CP waves correspond to the intersections of the contour lines of the no-reflection angles in Fig. 4.3. Using the electric susceptibility $\chi_\mathrm{e} = \varepsilon_\mathrm{r} - 1$ and magnetic susceptibility $\chi_\mathrm{m} = 1 - \mu_\mathrm{r}^{-1}$, Eqs. (4.39) and (4.40) are reduced to simpler forms:

$$\chi_\mathrm{e} = \chi_\mathrm{m} = \mp\xi_\mathrm{r}, \tag{4.41}$$

$$\chi_\mathrm{e} + 2 = \chi_\mathrm{m} - 2 = \pm\xi_\mathrm{r}, \tag{4.42}$$

respectively, where the upper (lower) sign corresponds to the condition for LCP (RCP) waves.

We clarify the physical meaning of the no-reflection effect for CP waves by considering the medium polarization $\boldsymbol{P}$ and magnetization $\boldsymbol{M}$ induced by $\boldsymbol{E}$ and $\boldsymbol{B}$ in CP waves. For simplicity, assume that the no-reflection condition is satisfied for LCP waves. $\boldsymbol{P}$ and $\boldsymbol{M}$ are given by $\boldsymbol{P} = \boldsymbol{P}_\mathrm{E} + \boldsymbol{P}_\mathrm{B}$ and $\boldsymbol{M} = \boldsymbol{M}_\mathrm{B} + \boldsymbol{M}_\mathrm{E}$, where $\boldsymbol{P}_\mathrm{E} = (\varepsilon - \varepsilon_0)\boldsymbol{E}$, $\boldsymbol{P}_\mathrm{B} = -\mathrm{i}\,\xi\boldsymbol{B}$, $\boldsymbol{M}_\mathrm{B} = -(\mu^{-1} - \mu_0^{-1})\boldsymbol{B}$, and $\boldsymbol{M}_\mathrm{E} = \mathrm{i}\,\xi\boldsymbol{E}$ [37]. First, we calculate $\boldsymbol{P}$ and $\boldsymbol{M}$ when Eq. (4.39) is satisfied. From the relation $\boldsymbol{H} = (\mathrm{i}/Z_\mathrm{c})\boldsymbol{E}$ that is satisfied for LCP waves (see Tab. 2.1), and Eqs. (2.31), (2.32), and (4.39), it is not difficult to confirm that $\boldsymbol{P} = 0$ and $\boldsymbol{M} = 0$ are satisfied regardless of the propagation direction. Due to the electromagnetic mixing attributed to ξ, the polarization $\boldsymbol{P}_\mathrm{B}$, which is induced by the magnetic flux density, completely cancels out the polarization $\boldsymbol{P}_\mathrm{E}$, which is induced by the electric field. Similarly, $\boldsymbol{M}_\mathrm{E}$ cancels out $\boldsymbol{M}_\mathrm{B}$. As a result of the destructive interference of electric and magnetic responses, net polarization and magnetization vanish in the case of LCP waves in the chiral medium. This implies that the chiral medium is identical to the vacuum for LCP waves. Next, we calculate $\boldsymbol{P}$ and $\boldsymbol{M}$ when Eq. (4.40) is satisfied. By

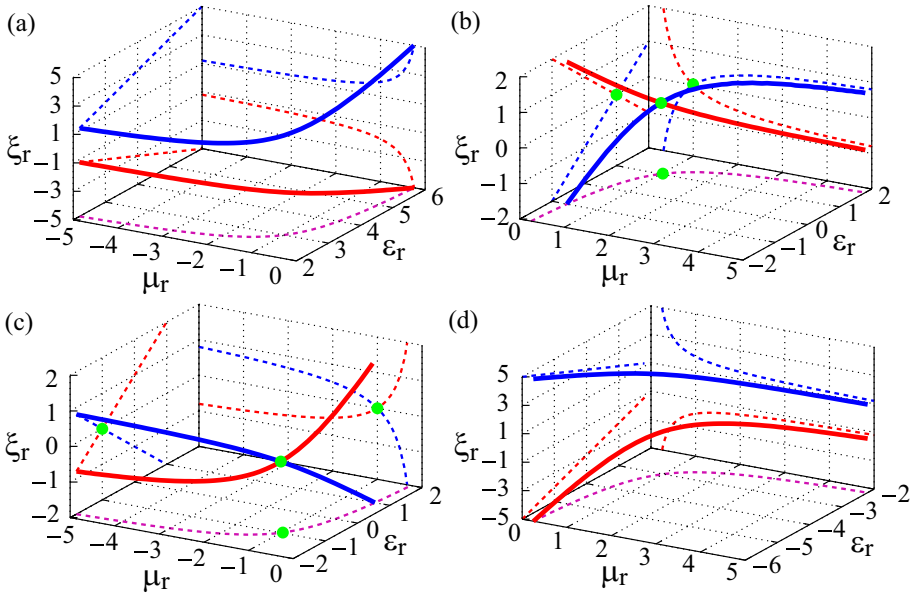

Figure 4.5: Relations among ε_{r}, μ_{r}, and ξ_{r} that satisfy the no-reflection condition for CP waves: (a), (b) relations given by Eq. (4.39), and (c), (d) relations given by Eq. (4.40). Red (blue) solid lines represent the no-reflection condition for LCP (RCP) waves. Dashed lines are projections of solid lines on each plane. Green solid circles correspond to (b) vacuum and (c) anti-vacuum.

applying a similar procedure, we obtain $\boldsymbol{P} = -2\varepsilon_0\boldsymbol{E}$ and $\boldsymbol{M} = -2\boldsymbol{H}$, which equal the corresponding values in an anti-vacuum. Therefore, the chiral medium behaves as an anti-vacuum for LCP waves.

4.3.3 No-reflection effect for linearly polarized waves

When $\xi = 0$ or $k_+ = -k_-$ is satisfied, c_2 vanishes and the reflection matrix becomes $M_{\mathrm{R}} = c_{\mathrm{u}}I + c_3\sigma_3$. The eigenpolarizations are $\boldsymbol{e}_x \sin\theta + \boldsymbol{e}_y \cos\theta$ and $\boldsymbol{e}_z$; therefore, the no-reflection condition can only be satisfied for linearly polarized waves. The no-reflection effect is observed at a particular incident angle that satisfies $c_{\mathrm{u}} = \pm c_3$. The equation $c_{\mathrm{u}} = c_3$ ($c_{\mathrm{u}} = -c_3$) yields a no-reflection angle, or the Brewster angle, for TM (TE) waves.

The condition $\xi = 0$ implies that the medium is achiral. We have already

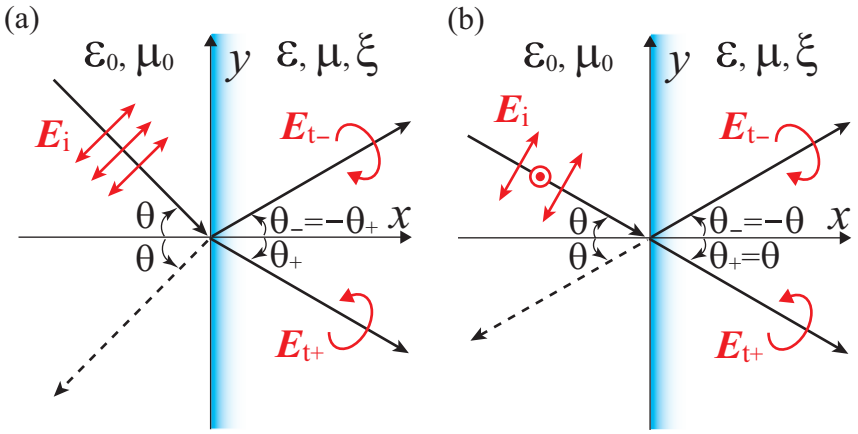

Figure 4.6: No-reflection effect for chiral nihility media. (a) In the case of $Z_\mathrm{r} \neq 1$ and $n \neq \pm 1$, no-reflection effect arises for TM (TE) waves at the incident angle that satisfies $c_\mathrm{u} = c_3$ ($c_\mathrm{u} = -c_3$). (b) In the case of $Z_\mathrm{r} = 1$ and $n = \pm 1$, no-reflection effect arises for arbitrary polarized waves at all angles of incidence.

analyzed the no-reflection condition for achiral, or isotropic media in Sec. 3.1. Here, we analyze the no-reflection effect for the case of $k_+ = -k_-$, or chiral nihility media [62].

From $c_\mathrm{u} = \pm c_3$, we obtain the no-reflection angles θ_TM and θ_TE for TM and TE waves:

$$\theta_\mathrm{TM} = \arcsin\sqrt{\frac{Z_\mathrm{r}^{-2} - 1}{Z_\mathrm{r}^{-2} - n^{-2}}} \quad (\text{from } c_\mathrm{u} = c_3), \tag{4.43}$$

$$\theta_\mathrm{TE} = \arcsin\sqrt{\frac{Z_\mathrm{r}^{2} - 1}{Z_\mathrm{r}^{2} - n^{-2}}} \quad (\text{from } c_\mathrm{u} = -c_3), \tag{4.44}$$

where $Z_\mathrm{r} = Z_\mathrm{c}/Z_0$ and $n = k_+/k_0 = -k_-/k_0$. The no-reflection effect in this case resembles but is different from that in the achiral case. While the transmitted wave is a linearly polarized wave in the achiral case, LCP and RCP waves that satisfy $\theta_+ = -\theta_-$ are transmitted in this case. Equations (4.21) and (4.26)-(4.29) show that the intensities of the transmitted LCP and RCP waves are equal. Figure 4.6(a) illustrates a schematic of the no-reflection effect for chiral nihility media when $c_2 = 0$, $c_\mathrm{u} \neq 0$, and $c_3 \neq 0$, namely $Z_\mathrm{r} \neq 1$ and $n \neq \pm 1$.

The medium parameters satisfying the no-reflection condition are derived from

$$(\varepsilon_{\mathrm{r}} + \mu_{\mathrm{r}}\xi_{\mathrm{r}}^2)\mu_{\mathrm{r}} = 0, \tag{4.45}$$

$$Z_{\mathrm{r}}^2(\varepsilon_{\mathrm{r}} + \mu_{\mathrm{r}}\xi_{\mathrm{r}}^2) = \mu_{\mathrm{r}}, \tag{4.46}$$

$$\mu_{\mathrm{r}}\xi_{\mathrm{r}} = \pm n. \tag{4.47}$$

Equation (4.45) is the condition for chiral nihility ($k_+ = -k_-$), and Eqs. (4.46) and (4.47) are the conditions for the wave impedance and wavenumber. To satisfy these equations at a particular angular frequency ω_0, the medium parameters need to be written as the following equations around ω_0:

$$\left.\begin{aligned} \varepsilon_{\mathrm{r}}(\omega) &= \frac{n}{Z_{\mathrm{r}}}\left[f(\omega-\omega_0) - \frac{1}{f(\omega-\omega_0)}\right], \\ \mu_{\mathrm{r}}(\omega) &= nZ_{\mathrm{r}}f(\omega-\omega_0), \\ \xi_{\mathrm{r}}(\omega) &= \pm\frac{1}{Z_{\mathrm{r}}f(\omega-\omega_0)}, \end{aligned}\right\} \tag{4.48}$$

where the function f satisfies $\lim_{\omega\to\omega_0} f(\omega-\omega_0) = 0$.

When $Z_{\mathrm{r}} = 1$ and $n = \pm 1$, namely, $Z_{\mathrm{c}} = Z_0$ and $|k_\pm| = k_0$ are satisfied, the reflection matrix M_{R} becomes a zero matrix. Since the conditions $Z_{\mathrm{c}} = Z_0$ and $|k_\pm| = k_0$ are independent of the incident angle, M_{R} becomes a zero matrix for all angles of incidence; arbitrary polarized waves are not reflected for any incident angle. Figure 4.6(b) shows a schematic of the no-reflection effect. This phenomenon has been confirmed by numerically calculating the reflectivity when $Z_{\mathrm{c}} = Z_0$ and $|k_\pm| \approx k_0$ are satisfied [63].

We consider the physical meaning of Eq. (4.48) when both $Z_{\mathrm{r}} = 1$ and $n = \pm 1$ are satisfied. For simplicity, suppose that $(\varepsilon_{\mathrm{r}}, \mu_{\mathrm{r}}, \xi_{\mathrm{r}}) = [f(\omega-\omega_0) - f(\omega-\omega_0)^{-1}, f(\omega-\omega_0), f(\omega-\omega_0)^{-1}]$ are satisfied in this paragraph. The medium polarization and magnetization are found to be $\boldsymbol{P} = \varepsilon_0 f(\omega-\omega_0)\boldsymbol{E} \to 0$ and $\boldsymbol{M} = f(\omega-\omega_0)\boldsymbol{H} \to 0$ for LCP waves and $\boldsymbol{P} = \varepsilon_0[f(\omega-\omega_0)-2]\boldsymbol{E} \to -2\varepsilon_0\boldsymbol{E}$ and $\boldsymbol{M} = [f(\omega-\omega_0)-2]\boldsymbol{H} \to -2\boldsymbol{H}$ for RCP waves when $\omega \to \omega_0$. This implies that the medium behaves as a vacuum for LCP waves and as an anti-vacuum for RCP waves.

The no-reflection condition in the case of $Z_{\mathrm{c}} = Z_0$ and $|k_\pm| = k_0$ can be regarded as the case of $|\xi_{\mathrm{r}}| \to \infty$ in Eqs. (4.39) and (4.40). From Eqs. (4.39) and (4.40),

we find that the vacuum condition for LCP (RCP) waves and the anti-vacuum condition for RCP (LCP) waves can be simultaneously satisfied when $|\xi_\mathrm{r}| \to \infty$. In other words, the points represented by L_+ and R_- (L_- and R_+) in Fig. 4.3 approach each other with increasing $|\xi_\mathrm{r}|$ and the two points become identical in the case of $|\xi_\mathrm{r}| \to \infty$.

4.4 FDTD analysis of no-reflection effect for CP waves

We focus on the no-reflection effect for CP waves and analyze the no-reflection effect by an FDTD method. Here, the parameters of the chiral medium are set as $\varepsilon_\mathrm{r} = 0.75$, $\mu_\mathrm{r} = 0.8$, and $\xi_\mathrm{r} = 0.25$, which give $Z_\mathrm{c} = Z_0$, $k_+ = k_0$, and $k_- = 0.6k_0$. That is, the no-reflection condition (vacuum condition) is satisfied for LCP waves.

To adopt the two-dimensional FDTD method, Maxwell's equations for CP waves are rearranged as follows:

$$\frac{\partial E_{z\pm}}{\partial y} = \mathrm{i}\omega(\mu \pm \mu\xi Z_\mathrm{c}) H_{x\pm}, \tag{4.49}$$

$$-\frac{\partial E_{z\pm}}{\partial x} = \mathrm{i}\omega(\mu \pm \mu\xi Z_\mathrm{c}) H_{y\pm}, \tag{4.50}$$

$$\frac{\partial H_{y\pm}}{\partial x} - \frac{\partial H_{x\pm}}{\partial y} = -\mathrm{i}\omega \left[(\varepsilon + \mu\xi^2) \pm \frac{\mu\xi}{Z_\mathrm{c}} \right] E_{z\pm}, \tag{4.51}$$

where the relation $\boldsymbol{H} = \pm(\mathrm{i}/Z_\mathrm{c})\boldsymbol{E}$ is used and the positive (negative) sign corresponds to LCP (RCP) waves. Section 4.3.2 and Eqs. (4.21) and (4.26)-(4.29) show that the incident CP wave is not converted into the other CP wave on the reflection and refraction because the wave impedance matching condition $Z_\mathrm{c} = Z_0$ is satisfied in this case. Thus, we may separately analyze the propagations of LCP and RCP waves.

We set the dimension of the simulation region to $40\lambda \times 40\lambda$. The unit cell size $\Delta x \times \Delta y$ is $(\lambda/15) \times (\lambda/15)$ and the time step size is $0.30\Delta x/c_0$. The second Mur absorbing boundary condition is applied to the outside boundaries. A Gaussian beam with a beamwidth of 8.4λ is used as an input electromagnetic wave.

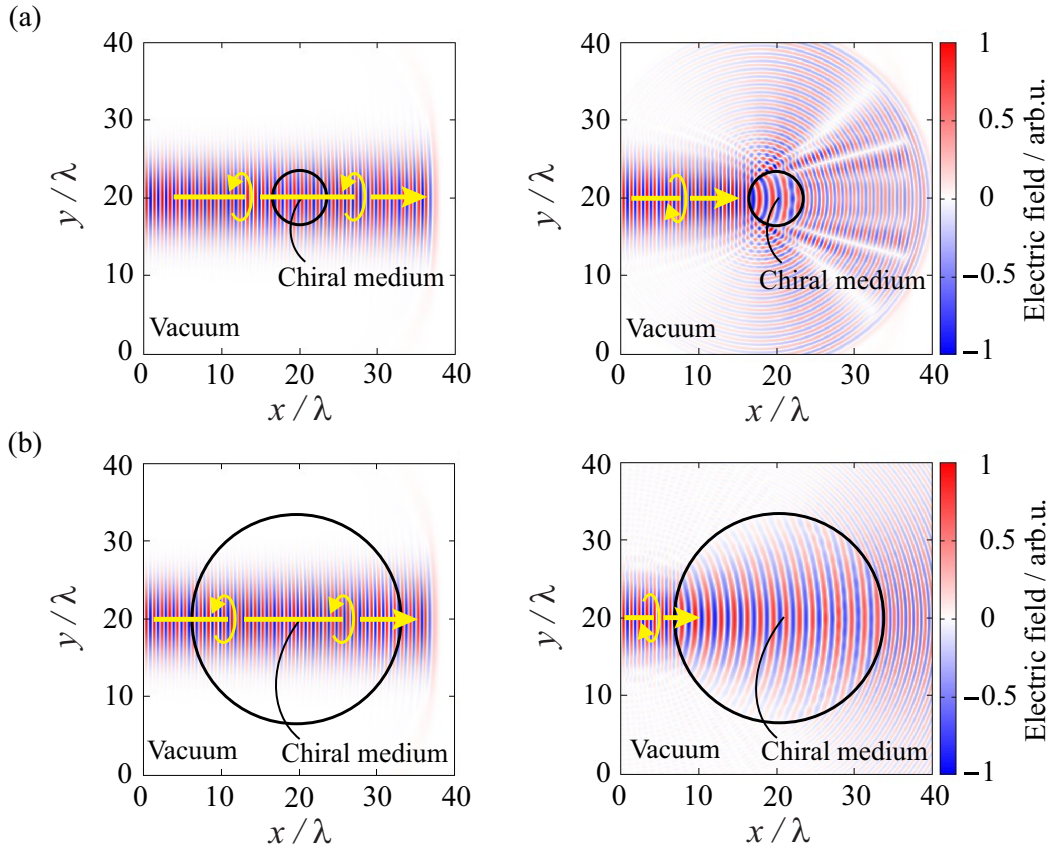

Figure 4.7: Scattering of electromagnetic waves by cylindrical chiral medium when diameter of chiral medium is (a) smaller and (b) larger than beamwidth of electromagnetic wave. Left panels show propagations of LCP waves and right panels show those of RCP waves.

First, we compute the scattering of electromagnetic waves by a cylinder made of the chiral medium. Figure 4.7 shows the propagations of electromagnetic waves when the diameter of the cylindrical chiral medium is smaller (diameter: 6.7λ) and larger (diameter: 26.7λ) than the beamwidth of the electromagnetic waves. One sees that LCP waves propagate with no scattering, and RCP waves are largely scattered.

Next, we analyze the propagation of electromagnetic waves when they are incident on a triangular prism made of the chiral medium. For $k_- = 0.6k_0$, Snell's

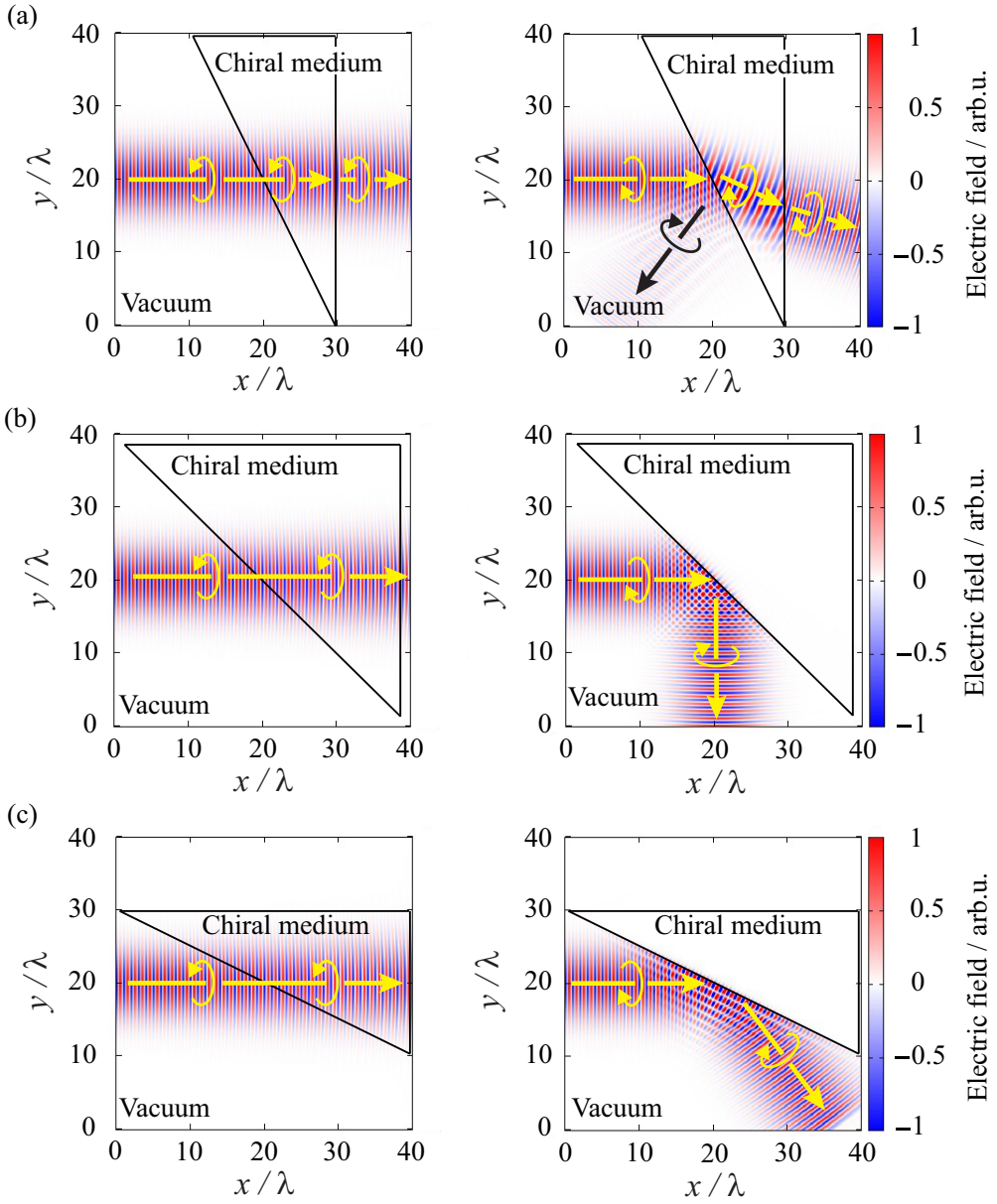

Figure 4.8: Circular polarizing beam splitter. Incident angle is (a) 26.5°, (b) 45°, and (c) 63.5°. (left panels) Propagations of LCP waves and (right panels) of RCP waves.

equation for RCP waves is expressed as $\sin\theta = 0.6\sin\theta_{-}$; hence, the critical angle for RCP waves is $\theta_{\mathrm{c}} = \arcsin(0.6) \simeq 37^{\circ}$. Therefore, LCP waves are completely transmitted without any reflection, while RCP waves are totally reflected with the incident angle greater than 37°. This implies that we can divide the incident waves into LCP and RCP waves. That is, the prism can be utilized as a circular polarizing beam splitter. The left (right) panels of Fig. 4.8 show the propagations of LCP (RCP) waves. Simulations are performed for three incident angles: 26.5°, 45°, and 63.5°. The LCP wave is transmitted straight through the chiral medium without reflection for any incident angle. Although the RCP wave is partially reflected and partially transmitted in the case of $\theta < \theta_{\mathrm{c}}$, it is totally reflected at the surface of the chiral medium when $\theta > \theta_{\mathrm{c}}$. This result confirms that the incident wave can be split into LCP and RCP waves, and circular polarizing beam splitter is achieved when the incident angle exceeds θ_{c}.

4.5 Design of three-dimensional isotropic chiral metamaterial

Isotropic chiral media can be realized by arranging chiral meta-atoms [64–69] isotropically and by electromagnetically induced chirality in atomic systems [70,71]. For the ease of experimental implementation, we consider how to fabricate isotropic chiral media using metamaterials.

We propose a metamaterial shown in Fig. 4.9(a) as an artificial isotropic chiral medium. Figure 4.9(b) shows a constituent, which is made of metal, of the proposed chiral metamaterial. The constituent is not identical to its mirror image and thus exhibits chirality. In addition, it has four-fold rotational symmetry along the z-axis. This indicates that the helix structure can be a constituent of isotropic metamaterials. The pitch p of the helix must be smaller than a half of the wavelength of electromagnetic waves so that the helix structure behaves as a meta-atom.[1] The metamaterial shown in Fig. 4.9(a) consists of three-dimensionally arranged helix structures shown in Fig. 4.9(b). Since the axes of the helices are directed to three distinct orthogonal directions, the metamaterial behaves as an isotropic medium.

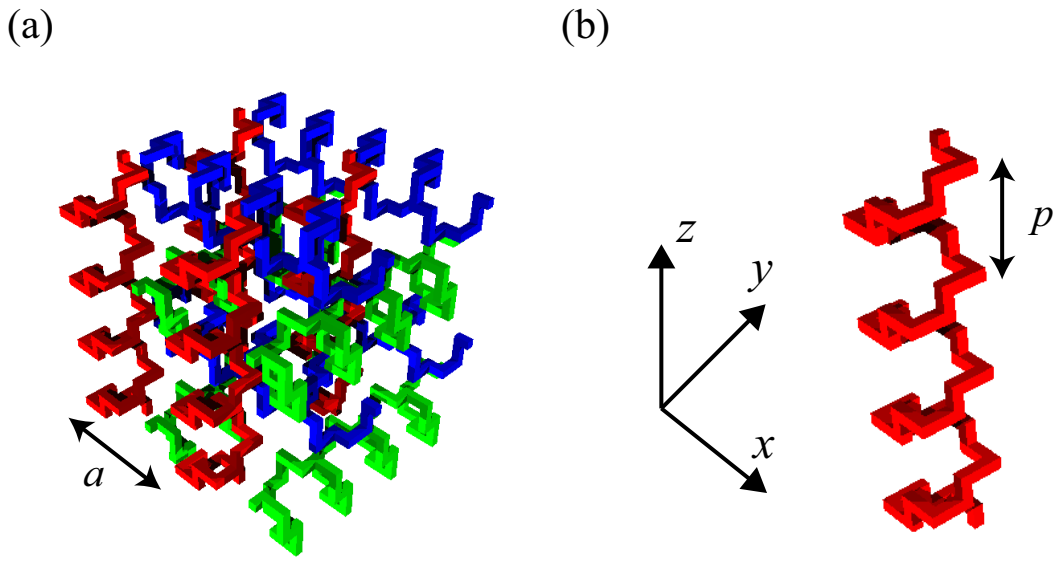

Figure 4.9: Schematic of an isotropic chiral metamaterial. (a) Three-dimensional isotropic chiral structure and (b) its constituent. The color coding serves as a guide to the eye.

The period a of the structure must be smaller than a half of the wavelength so that the metamaterial can be regarded as a continuous medium.[1]

The proposed metamaterial could be fabricated, for example, by using printed circuit boards in the microwave region and by means of three-dimensional direct laser writing [72, 73] in the infrared region.

4.6 Summary

We studied the no-reflection conditions for a planar boundary between a vacuum and a chiral medium. The comparison of the no-reflection conditions for achiral and chiral media is shown in Tab. 4.1. While the no-reflection effect arises for TM and TE waves in the case of achiral media ($\xi = 0$), it arises for EP waves in the case

[1] If the pitch p of the helix and the period a of the metamaterial are smaller than a half of the wavelength, the diffraction does not occur. This implies that the metamaterial acts as a homogeneous medium.

of chiral media ($\xi \neq 0$) whose wave impedances do not equal the vacuum wave impedance. These no-reflection conditions are satisfied for a particular incident angle. When the wave impedance and the absolute value of the wavenumber in the chiral medium equal those in the vacuum for one of the CP waves, the corresponding CP wave is transmitted with no-reflection for all angles of incidence. Although the no-reflection effect for chiral nihility media resembles that for achiral media, the two cases of the no-reflection effect are different from each other in the transmitted waves.

We analyzed the no-reflection effect for CP waves by an FDTD method. The simulation results showed that a chiral medium, whose medium parameters satisfy the no-reflection effect for one of the CP waves, does not scatter the corresponding CP wave and it largely scatters the other CP wave. The FDTD simulation also demonstrated that a circular polarizing beam splitter can be achieved by a triangular prism made of the chiral medium.

We proposed the structure of a three-dimensional isotropic chiral metamaterial. The metamaterial is composed of three-dimensionally arranged metal helix structures that have four-fold rotational symmetry along the helix axes. The chiral metamaterial could be fabricated in the microwave and infrared regions using state-of-the-art technology.

For future studies, we must prepare metamaterials whose ε_{r}, μ_{r}, and ξ_{r} satisfy the no-reflection conditions for EP and CP waves.

Table 4.1: Classification of no-reflection conditions for achiral ($\xi = 0$) and chiral ($\xi \neq 0$) media.

$\xi = 0$

Wave impedance	$Z_\mathrm{c} \neq Z_0$		$Z_\mathrm{c} = Z_0$
Medium parameters, Incident angle	$c_\mathrm{u} = c_3$	$c_\mathrm{u} = -c_3$	$k \equiv k_\pm = \pm k_0$
Polarization	TM	TE	—
No-reflection angle	$^\exists\theta$	$^\exists\theta$	$^\forall\theta$
Refraction	yes	yes	no (when $k = k_0$) yes (when $k = -k_0$)

$\xi \neq 0$

Wave impedance	$Z_\mathrm{c} \neq Z_0$		$Z_\mathrm{c} = Z_0$	
Medium parameters, Incident angle	$c_\mathrm{u} = c_\varphi$, $Z_\mathrm{c} > Z_0$ or $c_\mathrm{u} = -c_\varphi$, $Z_\mathrm{c} < Z_0$	$c_\mathrm{u} = -c_\varphi$, $Z_\mathrm{c} > Z_0$ or $c_\mathrm{u} = c_\varphi$, $Z_\mathrm{c} < Z_0$	$k_+ = \pm k_0$	$k_- = \pm k_0$
Polarization	TM-like EP	TE-like EP	LCP	RCP
No-reflection angle	$^\exists\theta$	$^\exists\theta$	$^\forall\theta$	$^\forall\theta$
Refraction	yes	yes	no (when $k_+ = k_0$) yes (when $k_+ = -k_0$)	no (when $k_- = k_0$) yes (when $k_- = -k_0$)

Chapter 5

Conclusion

5.1 Summary of this study

We have studied Brewster's no-reflection phenomena for isotropic and chiral metamaterials.

In Chap. 2, we showed the method for calculating the wavenumber and wave impedance that can be applied to metamaterials where medium parameters become complex values as well as real positive values. The wavenumber and wave impedance can be determined unambiguously by considering the relations between the direction of the power flow and the real part of the wave impedance and between the wavenumber and wave impedance. We clarified the relation among the electromagnetic fields, wavenumber, and wave impedance for each eigenmode from the diagonalized Maxwell equation. The calculation method can also be applied to generalized media having anisotropy and non-reciprocity, namely, bi-anisotropic media.

In Chap. 3, we demonstrated Brewster's effect for TE waves in a magnetic metamaterial. An array of SRRs was used for the experiment as a magnetic metamaterial. The FDTD simulation showed that the TE Brewster effect could be easily observed in the narrow frequency region just below the resonance frequency of the SRR array. The reliability of the simulation was confirmed by experimentally examining the properties of the single SRR and the SRR array. We measured the incident angle dependence of the reflectivity at the boundary between air and the

SRR array and were successful in observing Brewster's effect for TE waves.

In Chap. 4, we studied the no-reflection conditions for a planar interface between a vacuum and a chiral medium. While the no-reflection effect arises for TM and TE waves in the case of achiral media, it arises for EP waves in the case of chiral media whose wave impedances do not equal the vacuum wave impedance. These no-reflection conditions are satisfied for a particular incident angle. When the wave impedance and the absolute value of the wavenumber in the chiral medium equal those in a vacuum for one of the CP waves, the corresponding CP wave is transmitted with no reflection for all angles of incidence. The no-reflection effect for chiral nihility media resembles but is different from that for achiral media. The two cases of the no-reflection effect are different from each other in terms of the transmitted waves. We analyzed the no-reflection effect for CP waves by an FDTD method. We confirmed that the one of the CP waves, for which the no-reflection condition is satisfied, propagates straight through the chiral medium and the other CP wave is largely scattered by the chiral medium. The FDTD analysis demonstrated that the no-reflection effect for CP waves can be utilized as a circular polarizing beam splitter. We presented a discussion on the structure of three-dimensional isotropic chiral metamaterials that are necessary to achieve the no-reflection effects for EP and CP waves. The chiral metamaterial could be fabricated by three-dimensionally arranging metal helices that have four-fold rotational symmetry along the helix axes with state-of-the-art technology.

5.2 Future prospects

For future studies of Brewster's no-reflection phenomena, we must fabricate a three-dimensional isotropic chiral metamaterial whose $\varepsilon_{\rm r}$, $\mu_{\rm r}$, and $\xi_{\rm r}$ satisfy the no-reflection conditions for EP and CP waves. In addition to experimentally verifying the no-reflection effects in the microwave region, we need to fabricate the chiral metamaterials in the terahertz and optical regions where there might be many applications of the no-reflection phenomena.

We summarize phenomena that have been achieved by utilizing metamaterials as shown in Fig. 5.1 in order to discuss future prospects of the study of metamate-

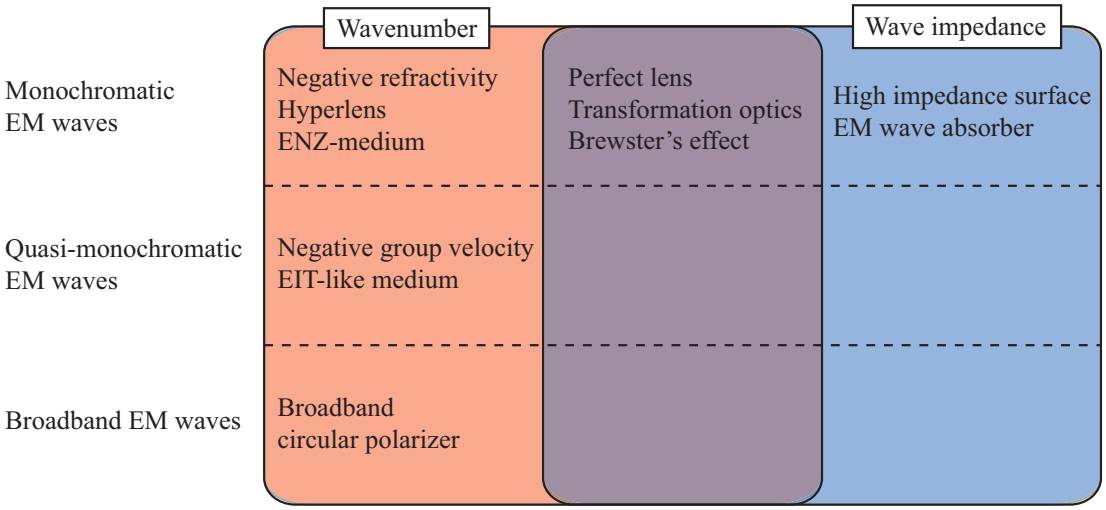

Figure 5.1: Classification of phenomena that have been achieved by utilizing metamaterials whose electromagnetic responses are linear and time-invariant. EM, electromagnetic; ENZ, epsilon-near-zero; EIT, electromagnetically-induced-transparency.

rials. Here we list only phenomena that can be achieved by metamaterials whose electromagnetic responses are linear and time-invariant. The red, blue, and purple regions represent wavenumber control, wave impedance control, and simultaneous control of wavenumber and wave impedance, respectively. Each region is classified into three categories: controls for monochromatic, quasi-monochromatic, and broadband electromagnetic waves. A negative refractive index medium [3, 4, 14], a hyperlens [7, 8], and an epsilon-near-zero medium [74–76] are listed as examples of the wavenumber control for a monochromatic electromagnetic wave. As examples of the wave impedance control for a monochromatic electromagnetic wave, we list a high impedance surface [77] and an electromagnetic wave absorber [78, 79]. A perfect lens [5, 6] and transformation optics [9, 11, 16] are examples of simultaneous control of the wavenumber and wave impedance. Our study [42, 60], namely Brewster's effect, is classified into this category, too. For a quasi-monochromatic electromagnetic wave, the wavenumber controls are carried out and negative group velocity [80] and an electromagnetically-induced-transparency-like medium [81–83]

are achieved. In these studies, a differentiation of the wavenumber with respect to the frequency of the electromagnetic wave is controlled. For a broadband electromagnetic wave, thus far, only a broadband circular polarizer is achieved [73].

From Fig. 5.1, one can see that most studies have focused on controlling a monochromatic electromagnetic wave and that there has been few studies of controlling quasi-monochromatic and broadband electromagnetic waves. In particular, the wave impedance controls for quasi-monochromatic and broadband electromagnetic waves have not received attention yet. Thus, it is necessary to consider methods for controlling differentiations of the wavenumber and wave impedance with respect to the frequency and broadband properties of the wavenumber and wave impedance using metamaterials. Considering novel phenomena that can be achieved by the metamaterials is also necessary. In addition to the linear response, non-linearity and time-variant response of metamaterials can be controlled. By utilizing these flexibilities of electromagnetic responses of metamaterials, we might develop novel devices for controlling propagation of electromagnetic waves.

Appendix A

Post and Tellegen representations

The Post representation:

$$\boldsymbol{D} = \varepsilon_{\mathrm{P}}\boldsymbol{E} - \mathrm{i}\xi_{\mathrm{P}}\boldsymbol{B}, \tag{A.1}$$

$$\boldsymbol{H} = \mu_{\mathrm{P}}^{-1}\boldsymbol{B} - \mathrm{i}\xi_{\mathrm{P}}\boldsymbol{E}, \tag{A.2}$$

and the Tellegen representation:

$$\boldsymbol{D} = \varepsilon_{\mathrm{T}}\boldsymbol{E} - \mathrm{i}\kappa_{\mathrm{T}}\boldsymbol{H}, \tag{A.3}$$

$$\boldsymbol{B} = \mu_{\mathrm{T}}\boldsymbol{H} + \mathrm{i}\kappa_{\mathrm{T}}\boldsymbol{E}, \tag{A.4}$$

are mainly used as the constitutive equations for chiral media [37]. Here $\varepsilon_{\mathrm{P,T}}$ is the permittivity, $\mu_{\mathrm{P,T}}$ is the permeability, and ξ_{p} and κ_{T} are the chirality parameters. The subscript P (T) stands for the Post (Tellegen) representation. We derive the relation between the medium parameters in these two constitutive equations. We also describe the wavenumber and wave impedance in chiral media using the Post and Tellegen representations.

By solving Eqs. (A.1) and (A.2) for $\boldsymbol{D}$ and $\boldsymbol{B}$, we obtain the following equations:

$$\boldsymbol{D} = (\varepsilon_{\mathrm{P}} + \mu_{\mathrm{P}}\xi_{\mathrm{P}}^2)\boldsymbol{E} - \mathrm{i}\mu_{\mathrm{P}}\xi_{\mathrm{P}}\boldsymbol{H}, \tag{A.5}$$

$$\boldsymbol{B} = \mu_{\mathrm{P}}\boldsymbol{H} + \mathrm{i}\mu_{\mathrm{P}}\xi_{\mathrm{P}}\boldsymbol{E}. \tag{A.6}$$

A comparison between Eqs. (A.3), (A.4) and Eqs. (A.5), (A.6) yields

$$\varepsilon_{\mathrm{T}} = \varepsilon_{\mathrm{P}} + \mu_{\mathrm{P}}\xi_{\mathrm{P}}^2, \quad \mu_{\mathrm{T}} = \mu_{\mathrm{P}}, \quad \kappa_{\mathrm{T}} = \mu_{\mathrm{P}}\xi_{\mathrm{P}}, \tag{A.7}$$

which are the relations between the medium parameters in the Post representation and that in the Tellegen representation. Note that the definitions of the medium parameters in the Post and Tellegen representations are different from each other.

As we showed in Sec. 2.2.1, the wavenumber and wave impedance in chiral media can be calculated by diagonalizing Maxwell's equation. These quantities in the Post and Tellegen representations are written as

$$k_\pm = \omega(\sqrt{\varepsilon_\mathrm{P}\mu_\mathrm{P} + \mu_\mathrm{P}^2\xi_\mathrm{P}^2} \pm \mu_\mathrm{P}\xi_\mathrm{P}) = \omega[(\varepsilon_\mathrm{P} + \mu_\mathrm{P}\xi_\mathrm{P}^2)Z_\mathrm{c} \pm \mu_\mathrm{P}\xi_\mathrm{P}], \tag{A.8}$$

$$= \omega(\sqrt{\varepsilon_\mathrm{T}\mu_\mathrm{T}} \pm \kappa_\mathrm{T}) = \omega(\varepsilon_\mathrm{T}Z_\mathrm{c} \pm \kappa_\mathrm{T}), \tag{A.9}$$

$$Z_\mathrm{c} = \sqrt{\frac{\mu_\mathrm{P}}{\varepsilon_\mathrm{P} + \mu_\mathrm{P}\xi_\mathrm{P}^2}}, \tag{A.10}$$

$$= \sqrt{\frac{\mu_\mathrm{T}}{\varepsilon_\mathrm{T}}}, \tag{A.11}$$

where $\mathrm{Re}\,(Z_\mathrm{c}) > 0$.

Acknowledgments

The author wishes to express his sincere appreciation to Professor Masao Kitano, Department of Electronic Science and Engineering, Kyoto University, for his continuous guidance and supervision.

The author would like to deeply acknowledge Professor Koichiro Tanaka, Institute for Integrated Cell-Material Sciences, Kyoto University, and Associate Professor Osamu Sakai, Department of Electronic Science and Engineering, Kyoto University, for their valuable comments and critical reading of the manuscript.

The author is deeply grateful to Associate Professor Kazuhiko Sugiyama, Department of Electronic Science and Engineering, Kyoto University, for his many helpful suggestions and encouragement. It is a willingness of the author to acknowledge fruitful discussions and continuous guidance of Assistant Professor Toshihiro Nakanishi, Department of Electronic Science and Engineering, Kyoto University. The author would like to thank Ms. Keiko Yamada and Ms. Hisako Sekiguchi for official assistance.

The author wishes to thank all of the members of Kitano Lab. including the past members for providing many kinds of support. In particular, the author would like to express his gratitude to Mr. Takehiro Hiramatsu, Mr. Hirokazu Kobayashi, Mr. Yugo Onoda, Mr. Tomoyuki Uehara, Mr. Shuhei Tamate, Mr. Yasuhiro Wakasa, Mr. Tetsuo Kanazawa, Mr. Yosuke Nakata, and Mr. Kalale Chola for their helpful and useful advice.

This research was supported by a Grant-in-Aid for Scientific Research on Innovative Areas (No. 22109004), the 21st Century COE Program (No. 14213201), and the Global COE program "Photonics and Electronics Science and Engineering" at Kyoto University. The author would like to acknowledge the support from

a Research Fellowship of the Japan Society for the Promotion of Science for Young Scientists.

Finally, the author would like to thank his parents for their continuous support and encouragement.

References

[1] R. E. Collin, *Field Theory of Guided Waves*, 2nd ed. (IEEE Press, Piscataway, NJ, 1990).

[2] J. B. Pendry, A. J. Holden, D. J. Robbins, and W. J. Stewart, "Magnetism from Conductors and Enhanced Nonlinear Phenomena," IEEE Trans. Microwave Theory Tech. **47**, 2075–2084 (1999).

[3] V. G. Veselago, "The electrodynamics of substances with simultaneously negative values of ε and μ," Sov. Phys. Usp. **10**, 509–514 (1968).

[4] R. A. Shelby, D. R. Smith, and S. Schultz, "Experimental Verification of a Negative Index of Refraction," Science **292**, 77–79 (2001).

[5] J. B. Pendry, "Negative Refraction Makes a Perfect Lens," Phys. Rev. Lett. **85**, 3966–3969 (2000).

[6] A. N. Lagarkov and V. N. Kissel, "Near-Perfect Imaging in a Focusing System Based on a Left-Handed-Material Plate," Phys. Rev. Lett. **92**, 077401 (2004).

[7] Z. Jacob, L. V. Alekseyev, and E. Narimanov, "Optical Hyperlens: Far-field imaging beyond the diffraction limit," Opt. Express **14**, 8247–8256 (2006).

[8] Z. Liu, H. Lee, Y. Xiong, C. Sun, and X. Zhang, "Far-Field Optical Hyperlens Magnifying Sub-Diffraction-Limited Objects," Science **315**, 1686 (2007).

[9] J. B. Pendry, D. Schurig, and D. R. Smith, "Controlling Electromagnetic Fields," Science **312**, 1780–1782 (2006).

[10] U. Leonhardt, "Optical Conformal Mapping," Science **312**, 1777–1780 (2006).

[11] D. Schurig, J. J. Mock, B. J. Justice, S. A. Cummer, J. B. Pendry, A. F. Starr, and D. R. Smith, "Metamaterial Electromagnetic Cloak at Microwave Frequencies," Science **314**, 977–980 (2006).

[12] S. Zhang, L. Yin, and N. Fang, "Focusing Ultrasound with an Acoustic Metamaterial Network," Phys. Rev. Lett. **102**, 194301 (2009).

[13] J. B. Pendry, A. J. Holden, W. J. Stewart, and I. Youngs, "Extremely Low Frequency Plasmons in Metallic Mesostructures," Phys. Rev. Lett. **76**, 4773–4776 (1996).

[14] J. Valentine, S. Zhang, T. Zentgraf, E. Ulin-Avila, D. A. Genov, G. Bartal, and X. Zhang, "Three-dimensional optical metamaterial with a negative refractive index," Nature **455**, 376–379 (2008).

[15] S. Zhang, W. Fan, K. J. Malloy, S. R. J. Brueck, N. C. Panoiu, and R. M. Osgood, "Near-infrared double negative metamaterials," Opt. Express **13**, 4922–4930 (2005).

[16] G. W. Milton, M. Briane, and J. R. Willis, "On cloaking for elasticity and physical equations with a transformation invariant form," New J. Phys. **8**, 248 (2006).

[17] M. Y. L. Zhang and and M. Qiu, "The effect of transformation order on the invisibility performance of a practical cylindrical cloak," J. Opt. A: Pure Appl. Opt. **10**, 095001 (2008).

[18] J. Li and J. B. Pendry, "Hiding under the Carpet: A New Strategy for Cloaking," Phys. Rev. Lett. **101**, 203901 (2008).

[19] R. Liu, C. Ji, J. J. Mock, J. Y. Chin, T. J. Cui, and D. R. Smith, "Broadband Ground-Plane Cloak," Science **323**, 366–369 (2009).

[20] J. Valentine, J. Li, T. Zentgraf, G. Bartal, and X. Zhang, "An optical cloak made of dielectrics," Nature Mater. **8**, 568–571 (2009).

[21] T. Ergin, N. Stenger, P. Brenner, J. B. Pendry, and M. Wegener, "Three-Dimensional Invisibility Cloak at Optical Wavelengths," Science **328**, 337–339 (2010).

[22] M. Rahm, S. A. Cummer, D. Schurig, J. B. Pendry, and D. R. Smith, "Optical Design of Reflectionless Complex Media by Finite Embedded Coordinate Transformations," Phys. Rev. Lett. **100**, 063903 (2008).

[23] W. Wang, H. Xing, L. Fang, Y. Liu, J. Ma, L. Lin, C. Wang, and X. Luo, "Far-field imaging device: planar hyperlens with magnification using multilayer metamaterial," Opt. Express **16**, 21142–21148 (2008).

[24] B. E. A. Saleh and M. C. Teich, *Fundamentals of Photonics*, 2nd ed. (John Wiley & Sons, Hoboken, NJ, 2007).

[25] W. T. Doyle, "Graphical approach to Fresnel's equations for reflection and refraction of light," Am. J. Phys. **48**, 643–647 (1980).

[26] G. P. Sastry and S. Chakrabarty, "The generalised Brewster condition from the extinction theorem," Eur. J. Phys. **8**, 125–127 (1987).

[27] J. Futterman, "Magnetic Brewster angle," Am. J. Phys. **63**, 471 (1995).

[28] C. Fu, Z. M. Zhang, and P. N. First, "Brewster angle with a negative-index material," Appl. Opt. **44**, 3716–3724 (2005).

[29] T. M. Grzegorczyk, Z. M. Thomas, and J. A. Kong, "Inversion of critical angle and Brewster angle in anisotropic left-handed metamaterials," Appl. Phys. Lett. **86**, 251909 (2005).

[30] T. Tanaka, A. Ishikawa, and S. Kawata, "Unattenuated light transmission through the interface between two materials with different indices of refraction using magnetic metamaterials," Phys. Rev. B **73**, 125423 (2006).

[31] N.-H. Shen, Q. Wang, J. Chen, Y.-X. Fan, J. Ding, and H.-T. Wang, "Total transmission of electromagnetic waves at interface associated with an indefinite medium," J. Opt. Soc. Am B **23**, 904–912 (2006).

[32] W. Shu, Z. Ren, H. Luo, and F. Li, "Brewster angle for anisotropic materials from the extinction theorem," Appl. Phys. A **87**, 297–303 (2007).

[33] S. Bassiri, C. H. Papas, and N. Engheta, "Electromagnetic wave propagation through a dielectric-chiral interface and through a chiral slab," J. Opt. Soc. Am. A **5**, 1450–1459 (1988).

[34] I. V. Lindell, A. H. Sihvola, S. A. Tretyakov, and A. J. Viitanen, *Electromagnetic Waves in Chiral and Bi-Isotropic Media* (Artech House, Boston, MA, 1994).

[35] A. Lakhtakia, "General schema for the Brewster conditions," Optik (Stuttgart) **90**, 184–186 (1992).

[36] A. Taflove and S. C. Hagness, *Computational Electrodynamics: The Finite-Difference Time-Domain Method*, 3rd ed. (Artech House, Norweed, MA, 2005).

[37] A. Serdyukov, I. Semchenko, S. Tretyakov, and A. Sihvola, *Electromagnetics of Bi-anisotropic Materials: Theory and Applications* (Gordon and Breach Science Publishers, LH, Amsterdam, 2001).

[38] N. I. Zheludev, S. L. Prosvirnin, N. Papasimakis, and V. A. Fedotov, "Lasing spacer," Nature Photon. **2**, 351–354 (2008).

[39] Y. Yuan, B.-I. Popa, and S. A. Cummer, "Zero loss magnetic metamaterials using powered active unit cells," Opt. Express **17**, 16135–16143 (2009).

[40] A. Fang, T. Koschny, M. Wegener, and C. M. Soukoulis, "Self-consistent calculation of metamaterials with gain," Phys. Rev. B **79**, 241104 (2009).

[41] S. Xiao, V. P. Drachev, A. V. Kildishev, X. Ni, U. K. Chettiar, H.-K. Yuan, and V. M. Shalaev, "Loss-free and active optical negative-index metamaterials," Nature **466**, 735–738 (2010).

[42] Y. Tamayama, T. Nakanishi, K. Sugiyama, and M. Kitano, "Observation of Brewster's effect for transverse-electric electromagnetic waves in metamaterials: Experiment and theory," Phys. Rev. B **73**, 193104 (2006).

[43] R. C. Johnson, ed., *Antenna Engineering Handbook*, 3rd ed. (McGrow-Hill, New York, NY, 1992).

[44] R. Marqués, F. Mesa, J. Martel, and F. Medina, "Comparative Analysis of Edge- and Broadside-Coupled Split Ring Resonators for Metamaterial Design—Theory and Experiments," IEEE Trans. Antennas Propag. **51**, 2572–2581 (2003).

[45] J. A. Stratton, *Electromagnetic Theory* (McGraw-Hill, New York, NY, 1941).

[46] T. Sakurai and K. Tamaru, "Simple Formulas for Two- and Three-Dimensional Capacitances," IEEE Trans. Electron Devices **ED-30**, 183–185 (1983).

[47] D. R. Smith, D. C. Vier, N. Kroll, and S. Schultz, "Direct calculation of permeability and permittivity for a left-handed metamaterial," Appl. Phys. Lett. **77**, 2246–2278 (2000).

[48] R. M. A. Azzam, "Maximum minimum reflectance of parallel-polarized light at interfaces between transparent and absorbing media," J. Opt. Soc. Am. **73**, 959–962 (1983).

[49] S. Y. Kim and K. Vedam, "Analytic solution of the pseudo-Brewster angle," J. Opt. Soc. Am. A **3**, 1772–1773 (1986).

[50] A. Das and S. K. Das, *Microwave Engineering* (McGraw-Hill, New York, NY, 2001).

[51] R. A. Witte, *Spectrum and network measurements* (SciTech Publishing, Raleigh, NC, 2006).

[52] D. R. Smith, S. Schultz, P. Markoš, and C. M. Soukoulis, "Determination of effective permittivity and permeability of metamaterials from reflection and transmission coefficients," Phys. Rev. B **65**, 195104 (2002).

[53] X. Chen, T. M. Grzegorczyk, B.-I. Wu, J. P. Jr., and J. A. Kong, "Robust method to retrieve the constitutive effective parameters of metamaterials," Phys. Rev. E **70**, 016608 (2004).

[54] D. M. Pozar, *Microwave Engineering*, 3rd ed. (John Wiley & Sons, Hoboken, NJ, 2005).

[55] P. Gay-Balmaz and O. J. F. Martin, "Electromagnetic resonances in individual and coupled split-ring resonators," J. Appl. Phys. **92**, 2929–2936 (2002).

[56] N. Katsarakis, T. Koschny, M. Kafesaki, E. N. Economou, and C. M. Soukoulis, "Electric coupling to the magnetic resonance of split ring resonators," Appl. Phys. Lett. **84**, 2943–2945 (2004).

[57] M. Born and E. Wolf, *Principles of Optics*, 2nd ed. (Pergamon Press, Headington, Oxford, 1964).

[58] A. Nishikata, "On the Influence of Specimen Size and Antenna Distance or Beam Convergence for the Reflectivity Measurement of Wave Absorber by Free Space Methods," J. IEICE **88**, 943 (2005). (*in Japanese*).

[59] R. Watanabe, M. Iwanaga, and T. Ishihara, "s-polarization Brewster's angle of stratified metal-dielectric metamaterial in optical regime," Phys. Stat. Sol. (b) **245**, 2696–2701 (2008).

[60] Y. Tamayama, T. Nakanishi, K. Sugiyama, and M. Kitano, "An invisible medium for circularly polarized electromagnetic waves," Opt. Express **16**, 20869–20875 (2008).

[61] J. J. Sakurai, *Modern Quantum Mechanics*, revised ed. (Addison-Wesley, Reading, MA, 1994).

[62] S. Tretyakov, I. Nefedov, A. Sihvola, S. Maslovski, and C. Simovsli, "Waves and energy in chiral nihility," J. of Electromagn. Waves and Appl. **17**, 695–706 (2003).

[63] C.-W. Qiu, N. Burokur, S. Zouhd, and L.-W. Li, "Chiral nihility effects on energy flow in chiral materials," J. Opt. Soc. Am. A **25**, 55–63 (2008).

[64] S. A. Tretyakov, F. Mariotte, C. R. Simovski, T. G. Kharina, and J.-P. Heliot, "Analytical Antenna Model for Chiral Scatterers: Comparison with Numerical and Experimental Data," IEEE Trans. Antennas Propag. **44**, 1006–1014 (1996).

[65] Y. Svirko, N. Zheludev, and M. Osipov, "Layered chiral metallic microstructures with inductive coupling," Appl. Phys. Lett. **78**, 498–500 (2001).

[66] M. Kuwata-Gonokami, N. Saito, Y. Ino, M. Kauranen, K. Jefimovs, T. Vallius, J. Turunen, and Y. Svirko, "Giant Optical Activity in Quasi-Two-Dimensional Planar Nanostructures," Phys. Rev. Lett. **95**, 227401 (2005).

[67] S. Zhang, Y.-S. Park, J. Li, X. Lu, W. Zhang, and X. Zhang, "Negative Refractive Index in Chiral Metamaterials," Phys. Rev. Lett. **102**, 023901 (2009).

[68] C. Rockstuhl, C. Menzel, T. Paul, and F. Lederer, "Optical activity in chiral media composed of three-dimensional metallic meta-atoms," Phys. Rev. B **79**, 035321 (2009).

[69] B. Wang, J. Zhou, T. Koschny, and C. M. Soukoulis, "Nonplanar chiral metamaterials with negative index," Appl. Phys. Lett. **94**, 151112 (2009).

[70] V. A. Sautenkov, Y. V. Rostovtsev, H. Chen, P. Hsu, G. S. Agarwal, and M. O. Scully, "Electromagnetically Induced Magnetochiral Anisotropy in a Resonant Medium," Phys. Rev. Lett. **94**, 233601 (2005).

[71] J. Kästel, M. Fleischhauer, S. F. Yelin, and R. L. Walsworth, "Tunable Negative Refraction without Absorption via Electromagnetically Induced Chirality," Phys. Rev. Lett. **99**, 073602 (2007).

[72] M. Thiel, M. S. Rill, G. von Freymann, and M. Wegener, "Three-Dimensional Bi-chiral Photonic Crystals," Adv. Mater. **21**, 4690–4682 (2009).

[73] J. K. Gansel, M. Thiel, M. S. Rill, M. Decker, K. Bade, V. Saile, G. von Freymann, S. Linden, and M. Wegener, "Gold Helix Photonic Metamaterial as Broadband Circular Polarizer," Science **325**, 1513–1515 (2009).

[74] M. Silveirinha and N. Engheta, "Tunneling of Electromagnetic Energy through Subwavelength Channels and Bends using ε-Near-Zero Materials," Phys. Rev. Lett. **97**, 157403 (2006).

[75] R. Liu, Q. Cheng, T. Hand, J. J. Mock, T. J. Cui, S. A. Cummer, and D. R. Smith, "Experimental Demonstration of Electromagnetic Tunneling Through an Epsilon-Near-Zero Metamaterial at Microwave Frequencies," Phys. Rev. Lett. **100**, 023903 (2008).

[76] B. Edwards, A. Alù, M. E. Young, M. Silveirinha, and N. Engheta, "Experimental Verification of Epsilon-Near-Zero Metamaterial Coupling and Energy Squeezing Using a Microwave Waveguide," Phys. Rev. Lett. **100**, 033903 (2008).

[77] D. Sievenpiper, L. Zhang, R. F. J. Broas, N. G. Alexópolous, and E. Yablonovitch, "High-Impedance Electromagnetic Surfaces with a Forbidden Frequency Band," IEEE Trans. Microwave Theory Tech. **47**, 2059–2074 (1999).

[78] N. I. Landy, S. Sajuyigbe, J. J. Mock, D. R. Smith, and W. J. Padilla, "Perfect Metamaterial Absorber," Phys. Rev. Lett. **100**, 207402 (2008).

[79] B. Wang, T. Koschny, and C. M. Soukoulis, "Wide-angle and polarization-independent chiral metamaterial absorber," Phys. Rev. B **80**, 033108 (2009).

[80] G. Dolling, C. Enkrich, M. Wegener, C. M. Soukoulis, and S. Linden, "Simultaneous Negative Phase and Group Velocity of Light in a Metamaterial," Science **312**, 892–894 (2006).

[81] J. Zhang, H. Chen, L. Ran, Y. Luo, B.-L. Wu, and J. A. Kong, "Experimental characterization and cell interactions of a two-dimensional isotropic left-handed metamaterial," Appl. Phys. Lett. **92**, 084108 (2008).

[82] N. Liu, L. Langguth, T. Weiss, J. Kästel, M. Fleischhauer, T. Pfau, and H. Giessen, "Plasmonic analogue of electromagnetically induced transparency at the Drude damping limit," Nature Mater. **8**, 758–762 (2009).

[83] Y. Tamayama, T. Nakanishi, Y. Wakasa, T. Kanazawa, K. Sugiyama, and M. Kitano, "Electromagnetic response of a metamaterial with field-gradient-induced transparency," Phys. Rev. B **82**, 165130 (2010).

List of publications

Journal papers

1. Y. Tamayama, T. Nakanishi, K. Sugiyama, and M. Kitano, "Observation of Brewster's effect for transverse-electric electromagnetic waves in metamaterials: Experiment and theory," Phys. Rev. B **73**, 193104-1-4 (2006).

2. Y. Tamayama, T. Nakanishi, K. Sugiyama, and M. Kitano, "An invisible medium for circularly polarized electromagnetic waves," Opt. Express **16**, 20869-20875 (2008).

Book chapters

1. Y. Tamayama, T. Nakanishi, K. Sugiyama, and M. Kitano, "No-Reflection Phenomena for Chiral Media," in *Electromagnetic Waves*, edited by Andrei Petrin (In-Tech, Janeza Trdine, Rijeka, 2011) (in press).

International conferences

1. Y. Tamayama, T. Nakanishi, K. Sugiyama, and M. Kitano, "No-reflection conditions for chiral media," Third International Congress on Advanced Electromagnetic Materials in Microwaves and Optics, Poster 1-12, London, UK, August 30-September 4 (2009).

2. M. Kitano, Y. Tamayama, and T. Nakanishi, "No-Reflection No-Refraction Metamaterial for Circularly Polarized Light," 2010 Asia-Pacific Radio Science Conference, DC1-1, Toyama, Japan, September 22-26 (2010).

Domestic conferences

1. Y. Tamayama, T. Nakanishi, K. Sugiyama, and M. Kitano, "Brewster's effect for TE waves with metamaterials," JPS 2005 Autumn Meeting, 20pWA-7,

Kyoto, September 19-22 (2005).

2. Y. Tamayama, T. Nakanishi, K. Sugiyama, and M. Kitano, "No-Reflection Effect for Circularly Polarized Electromagnetic Waves in Chiral Media," The 37th Annual Meeting on Electromagnetic Theory, EMT-08-104, Gifu, November 20-22 (2008).

3. Y. Tamayama, T. Nakanishi, K. Sugiyama, and M. Kitano, "A completely invisible medium for circularly polarized electromagnetic waves," The 64th JPS Annual Meeting, 30pSK-5, Tokyo, March 27-30 (2009).

4. Y. Tamayama, T. Nakanishi, K. Sugiyama, and M. Kitano, "No-reflection conditions for chiral media," JPS 2009 Autumn Meeting, 26pXB-14, Kumamoto, September 25-28 (2009).

Related publications

Journal papers

1. Y. Tamayama, T. Nakanishi, Y. Wakasa, T. Kanazawa, K. Sugiyama, and M. Kitano "Electromagnetic response of a metamaterial with field-gradient-induced transparency," Phys. Rev. B **82**, 165130-1-6 (2010).

International conferences

1. T. Nakanishi, Y. Wakasa, Y. Tamayama, T. Kanazawa, K. Sugiyama, and M. Kitano, "Electromagnetically-induced-transparency-like metamaterial with magnetic quadrupole," Third International Congress on Advanced Electromagnetic Materials in Microwaves and Optics, Poster 3-6, London, UK, August 30-September 4 (2009).

2. Y. Tamayama, T. Nakanishi, Y. Wakasa, T. Kanazawa, K. Sugiyama, and M. Kitano, "Field-gradient-induced-transparency metamaterial," Fourth International Congress on Advanced Electromagnetic Materials in Microwaves and Optics, Poster 1-39, Karlsruhe, Germany, September 13-16 (2010).

Domestic conferences

1. Y. Wakasa, T. Nakanishi, Y. Tamayama, T. Kanazawa, K. Sugiyama, and M. Kitano, "Electromagnetically-induced-transparency-like metamaterial with magnetic quadrupole resonance," JPS 2009 Autumn Meeting, 26pXB-15, Kumamoto, September 25-28 (2009).

2. T. Kanazawa, Y. Tamayama, T. Nakanishi, K. Sugiyama, and M. Kitano, "Controlling Group Velocity of Electromagnetic Waves in Varactor Loaded Metamaterials," JPS 2009 Autumn Meeting, 26pXB-16, Kumamoto, September 25-28 (2009).

3. Y. Tamayama, T. Nakanishi, Y. Wakasa, T. Kanazawa, K. Sugiyama, and M. Kitano, "Electric-field-gradient-induced-transparency in metamaterials," The 65th JPS Annual Meeting, 21pHL-13, Okayama, March 20-23 (2010).

4. T. Kanazawa, Y. Tamayama, T. Nakanishi, K. Sugiyama, and M. Kitano, "Enhancement of Second Harmonic Generation in Double Resonant Metamaterials," JPS 2010 Autumn Meeting, 25aRE-8, Osaka, September 23-26 (2010).